MODIFICATION OF ARCTIC CLOUDS BY LONG-RANGE AEROSOL TRANSPORT

by

Quentin Coopman

A dissertation submitted to the faculty of
The University of Utah
in partial fulfillment of the requirements for the degree of

Doctor of Philosophy

Department of Atmospheric Sciences

The University of Utah

May 2017

The University of Utah Graduate School

STATEMENT OF DISSERTATION APPROVAL

The dissertation of **Quentin Coopman**
has been approved by the following supervisory committee members:

Timothy J. Garrett ,	Chair(s)	**7 Dec 2016** Date Approved
Jérôme Riedi ,	Member	**7 Dec 2016** Date Approved
Gerald G. Mace ,	Member	**7 Dec 2016** Date Approved
Tristan S. L'Ecuyer ,	Member	**3 Jan 2017** Date Approved
John Chun-Han Lin ,	Member	**7 Dec 2016** Date Approved

by **Kevin D. Perry** , Chair/Dean of
the Department/College/School of **Atmospheric Sciences**
and by **David B. Kieda** , Dean of The Graduate School.

ABSTRACT

The Arctic region is warming particularly rapidly. Aerosol impacts on cloud microphysical parameters are still poorly understood. Aerosol-cloud interactions (ACI) play an important role for cloud radiative properties and climate change. A challenge in the study of ACI is the use of independent datasets for cloud microphysical parameters and aerosol content so they cannot influence one another.

In this study, we combine measurements from satellite instruments POLDER-3 and MODIS to temporally and spatially colocate cloud microphysical properties with carbon monoxide concentrations from GEOS-Chem and FLEXPART, serving as a passive tracer of aerosol content. We also add ERA-I reanalysis of meteorological parameters to stratify meteorological parameters such as specific humidity and lower tropospheric stability. Thus, observed differences in cloud microphysical parameters can be attributed to differences in aerosol content rather than meteorological variability.

We define a net aerosol-cloud interaction parameter (ACI^{net}) which can be interpreted as a measure of the sensitivity of a cloud at any given location to pollution plumes from distant sources. We use this parameter to study the impact of aerosols from anthropogenic and biomass burning sources from midlatitudes on liquid-cloud microphysical properties in Arctic, for a time period between 2005 and 2010, above ocean, and for controlled meteorological regimes. Our results suggest that the effect of biomass pollution plumes on clouds is smaller ($ACI^{net} \sim 0$) than that for anthropogenic pollution plumes ($ACI^{net} \sim 0.30$). Meteorological parameters can inhibit the aerosol-cloud interaction or favor the aerosol-cloud interaction.

The impact of anthropogenic aerosol on thermodynamic phase transition are analyzed. The smaller the effective radius, the higher the supercooling temperature whereas the greater the aerosol concentration, the lower the supercooling temperature. Independently of changes in effective radius, decrease in energy barrier due to an increase in aerosol concentration can be up to 48%.

CONTENTS

LIST OF TABLES

ACKNOWLEDGEMENTS

This manuscript and this research was examined by Dr. Kathy S. Law, Dr. Tristan S. L'Ecuyer, Dr. Denis Petitprez, Dr. Isabelle Chiapello, Dr. Gerald G. Mace, Dr. John C. Lin, Dr. Jérôme Riedi, and Dr. Timothy J. Garrett. I thank all of them for their advice, suggestions and comments which helped to improve this manuscript and will be a great benefit to my future research.

My acknowledgements also go to my two co-advisors: Jérôme Riedi and Tim Garrett. They supported me and optimized conditions for a successful PhD. My knowledge and my understanding in the atmospheric science field has been deeply intensified by their patience and their pedagogy. During the last three years, they have shared their motivation, enthusiasm, and precious advice. There is no doubt that the PhD would have been much more difficult without their knowledge and guidance.

I thank the financial support from NSF and the University of Lille. The financial support allowed me to go to many conferences, seminars, and workshops which motivated me, increased my knowledge, and expanded my professional network.

I thank François and Romain for their help in computing. I also thank Marie-Lyse Lievain, Anne Priem, Leslie Allaire, and Michelle Brook for their guidance and kindness in helping me going through administrative problems.

I cannot list all the friends who helped me to handle the PhD but here is a nonexhaustive list. In the US, for her great joy of life and for being the best American-life guide, Sarah, I feel so lucky to have met her. I lived in many different houses in the US, my roommates are still wonderful friends: Ian, Daniel, Ben, Mary-Kate, Prabhat, and Saurabh.

In the French part, many people encouraged me during the PhD, including people I met at kindergarten up to the end of my education. Isabelle for the morning coffee and delicious cakes, Romain for all the discussions about everything, Rita for her kindness, Anne BP for the different coffee breaks and laugh, Anne P. for afternoon tea-times, and Paul-Étienne, Fabien, and Gaël with whom I shared beer(s) after exhausting days. Many

thanks go to Fanny, Augustin, Pierre Sebastian, and Rudy, they showed me how to successfully complete the PhD.

My friends that I have known since kindergarten and junior high-school: Benjamin, Cesar, Thomas, Mathias, Caroline, Maxime, Louis F., Louis B., Xavier, Agathe, Peggy, François, and Claire. A special thank goes to Raphaëlle and Adrien, they helped me a lot during the last months of writing. Finally the ones I met at the University from my first year up to the end of my PhD; I have learned physics by their sides, sharing hard work sessions but so many other things: Audrey, Coralie, Pierre, Helene, Guillaume, and Simon.

Last but not least I thank my family: Mon frère Jean-Christophe et ma soeur Delphine, mes deux nièces Léanne et Charlotte et mes parents, Monique et Jean-Luc. Ils m'ont toujours encouragé et soutenu pour aller au bout de mes études et de mon projet de recherche tout au long de cette thèse mais aussi sur les différents objectifs de ma vie.

CHAPTER 1

GENERAL INTRODUCTION

1.1 Context

1.1.1 Scientific context

Climate change has been observed through different proxies: rising ocean level (Church and White 2006), sea-ice melting (Serreze et al. 2007), extinction of animal species (Thomas et al. 2004), desertification (Le Houerou 1996), and human migration (Reuveny 2007). Environmental issues are omnipresent in our societies and they are now a public concern. The so-called greenhouse effect, main actor of global warming, takes place in the atmosphere where it traps the radiation from earth but is transparent to solar radiation (Bolin and Doos 1989; Ramanathan and Vogelmann 1997). Clouds play an important role in the planetary energy budget as they can have both a cooling or warming effect, depending on their altitude and thickness (Hartmann et al. 1992). Cloud feedback is what happens when changes in surface air temperature lead to a change in cloud cover and properties, changing their radiative forcing at the surface, and so amplify or diminish the initial temperature (Held and Soden 2000; Stephens 2005). In the present global warming research, the study of cloud radiative impacts is important. For example, an increase of 17% in low-level cloud cover would offset the doubling in carbon dioxide warming (Slingo 1990). One of the key drivers of cloud properties is the presence of aerosols (Brock et al. 2011). Unfortunately aerosol-cloud interactions remain highly uncertain (McFarquhar et al. 2011) and their effects on surface temperature are difficult to quantify due to disagreement between large-scale and small-scale modeling studies (Stevens and Feingold 2009).

The arctic region acts as a regulator of global climate by receiving energy from the tropics, and, therefore, balancing the excess of solar radiation absorbed by tropical regions (Hassol 2004). Moreover, arctic sea ice plays an important role in the global climate system (Curry 1995): the sea-ice and snow surfaces are nine times more reflective to sunlight than the open ocean, which absorbs sun radiation and warms the surface (Perovich et al. 2002).

The Arctic is not pristine as the region receives pollution not only from long-range transport but also from new local sources located within the arctic region (Barrie 1986; Quinn et al. 2007a). The emergence of new local sources shifts the influence of pollutant from midlatitude human activities (Law et al. 2014) to new anthropogenic sources, such as gas flaring and wood burning (Ødemark et al. 2012; Winther et al. 2014). Cloud radiative properties influence the sea-ice extent (Schweiger et al. 2008; Kay et al. 2008; Van Tricht et al. 2016). A better understanding of aerosol-cloud interactions is needed to anticipate the sea-ice extent decrease, and therefore global warming (Kellogg 1975). Due to anthropogenic and natural variability (Shindell 2007), models predict that arctic warming will lead to a sea-ice-free summer by 2037 (Wang and Overland 2009).

In this manuscript, we intend to observe and quantify the impacts of aerosols on liquid cloud microphysical parameters and their impacts on liquid-ice cloud thermodynamic phase transition. In this chapter, we first compare present and future warming of the arctic region with the global warming of 2°C in 2030 (IPCC 2013) and some actors specific to the Arctic which explain the rapid warming. As clouds have an important role in the climate system, we quickly describe their conditions of formation, their microphysical and radiative parameters, and how the variation of the latter influences cloud radiative forcing. Finally, we conclude on the cloud radiative impact in the Arctic. Aerosols from midlatitude reach the arctic and influence cloud mirophysical properties: We describe the different pathways that aerosols follow and describe the different types of aerosols which are present in the Arctic. We present aerosol impacts on liquid clouds, and introduce the net aerosol-cloud interaction parameters (ACI^{net}) and the impacts of aerosols on cloud phase transition. Meteorological parameters having an impact on cloud properties, we state the importance to consider them in the problem of aerosol-cloud interactions. Finally, we describe the different objectives that we aim to complete in the present manuscript.

1.1.2 Arctic amplification

Over the last two decades, numerous field campaigns have been held in the Arctic to analyze cloud properties, aerosol-cloud interactions, and the radiative impact of clouds on climate. These include:

- 1994: The Beaufort and Arctic Storms Experiment (BASE, Curry et al. (1997))

- 1998: The First International Satellite Cloud Climatology Project (ISCCP) Regional Experiment Arctic Clouds Experiment (FIRE-ACE, Curry et al. (2000))
- 2004: The Mixed-Phase Arctic Cloud Experiment (M-PACE, Verlinde et al. (2007))
- 2004 and 2007: The Arctic Study of Tropospheric Cloud, Aerosol, and Radiation (ASTAR, Gayet et al. (2009); Jourdan et al. (2010))
- between 2007 and 2009: The International Polar Year (IPY)
- 2008: The Polar Study using Aircraft, Remote Sensing Surface Measurements, and Models of Climate, Chemistry, Aerosols and Transport (POLARCAT, Delanoë et al. (2013)
- 2008: Indirect and Semi-Direct Aerosol Campaign (ISDAC, McFarquhar et al. (2011))
- 2010: Solar Radiation and Phase Discrimination of Arctic Clouds experiment (SORPIC, Bierwirth et al. (2013))
- 2012: Vertical Distribution of Ice in Arctic clouds (VERDI, Klingebiel et al. (2015))

A driving interest in the arctic region is the regionally rapid global warming. Figure 1.1, from Screen and Simmonds (2010), shows the anomaly in surface temperature based on 1989-2008 data for different altitudes, seasons, and latitudes between 40° and 90°. For the different seasons, a general increase in temperature has been observed for all latitudes and altitudes of about 0.5°C per decade. Low altitudes in the Arctic have experienced a more intense warming than higher altitudes of about 1.5°C per decade on average and 2.5°C per decade during fall and winter. Altitudes higher than 800 hPa have never exceeded a warming of 1.25°C per decade.

Figure 1.1 also shows that the warming has been more intense for high latitudes. At the surface in winter the 1°C per decade isoline is around 67°N in latitude and isolines increase at greater latitudes. The Arctic has experienced a very rapid and more intense warming than midlatitude regions (Symon et al. 2004; Serreze and Francis 2006; Chapman and Walsh 2007a; Screen and Simmonds 2010; Sanderson et al. 2011; Richter-Menge and Jeffries 2011; Pithan and Mauritsen 2014), the intensification of the warming is usually referred to as arctic amplification.

1.1.3 Future arctic climate

In 1990, the first IPCC was published (IPCC 1990) assessing major conclusions and examining the key indicators of a climate change. In 2014, the fifth IPCC report was published with the same goal and assessed the scientific knowledge gained through observations, theoretical analysis, and modeling studies in different domains (LeTreut 2007): human and natural drivers of climate change, direct observations of recent climate change, palaeoclimatic perspective, understanding and attributing climate change, and projections of future changes in climate. From the first four reports, models were developed considering the different conclusions assessed for the 5 topics cited above: FAR in 1990, SAR in 1996, TAR in 2001, and AR4 in 2007.

Figure 1.2 a) from the IPCC (2013) shows the mean temperature anomalies, relative to 1961-1990 for different models considering different components. From 2001 to 2035, 4 models are considered: (i) FAR (Atmosphere, land surface, and ocean and sea ice) (Bretherton, F. P., Bryan, K., & Woods 1990), (ii) SAR (as FAR with aerosols) (IPCC 1996), (iii) TAR (same as SAR plus carbon cycle and dynamic vegetation) (Cubasch et al. 2001), (iv) AR4 (same as TAR plus atmospheric chemistry and land ice) (IPCC 2007), and from 1950 to 2001 the Coupled Model Intercomparison Project (CMIP3). The CMIP3 (light gray line) fits well with observations before 2001. FAR, SAR, TAR, and AR4 results are consistent with observations from 2001 to 2014.

The AR4 model ensemble is divided between 3 different scenarios: the B1 scenario represents the same global population as now with a reduction in material intensity and the introduction of clean technologies; the A2 scenario describes a continuous increase in population and delayed development of renewable energy, and finally, the A1B scenario describes a balance of fossil and nonfossil energy with rapid economic growth and an introduction of efficient technologies. Every model and scenario agrees on an increase of temperature between +0.5° and +2°C in 2035 compared to the 1961-1990 average.

Chapman and Walsh (2007b) produced an equivalent figure for arctic surface temperature shown in Figure 1.2 b) for latitudes between 60° and 90°. 14 global climate models, used in the IPCC (2001), derived temperature from 2000 to 2100 expressed as a departure from the 1981-2000 means. Prior to 2001, the models used greenhouse gas concentration and estimated sulfate aerosols (Wang et al. 2007). After 2001, they used the projected

greenhouse gas concentration for the three scenarios (Nakicenovic et al. 2000). From all 14 models, an increase of temperature is expected in the future. By the end of the 21st century the B1 scenario temperature anomalies range from +1° to +5.5°C, the A1B scenario ranges from +2.5° to +7.0°C, and the A2 scenario ranges from +4.0° to +9.0°C. If we consider 2030 to compare with the global evolution from the IPCC (2013) (Fig. 1.2 a), the increase of arctic temperature ranges from +0.2° to 3.7°C and continues through 2100.

Regardless of scenario or model, the temperature increase is most intense in the Arctic. If some actors of this warming are already well-known and understood such as greenhouse gases or heat fluxes (Yu and Weller 2007), there remain important questions to be answered, especially regarding the major feedback mechanisms.

1.1.4 Cloud and sea-ice feedback

A decrease in sea-ice extent has been observed over recent decades (Cavialieri et al. 1996; Parkinson et al. 1999; Serreze and Francis 2006) of about 34,300 $\pm$ 3700 km^2 (2.8% per decade) (Parkinson et al. 1999). A sea-ice-free summer is expected by 2039 according to IPCC models (Wang and Overland 2009; Overland and Wang 2013). The reason for the decline is attributed to the GHG radiative forcing, atmospheric circulation, oceanic circulation, and aerosol effects on cloud radiative properties (Shindell 2007).

The arctic amplification is primarily attributed to the sea-ice extent decrease (Serreze et al. 2009). As surface temperature increases, the sea-ice extent decreases and consequently the open-ocean surface increases (Curry 1995). The open-ocean is less reflective than the sea-ice surface (Robock 1980). In the presence of open ocean, sun radiation is absorbed increasing surface warming (Kellogg 1975).

Low-level clouds in the Arctic are different than those at lower latitudes (Verlinde et al. 2007). Weak solar irradiance, strong inversion, and the presence of sea-ice produce clouds with very stable temperature profiles (Curry 1986; Randall et al. 1996). For a cloud-free scene, sea ice reflects shortwave radiation and leads to a cooling effect compared to the open ocean. Clouds also reflect sunlight, but their presence also increases the absorption of longwave emissions from the surface. Due to the low solar radiation in the Arctic, the cloud shortwave reflection cooling effect is smaller than the cloud longwave emission warming effect (Shupe et al. 2013). Cloud presence has an important impact on the surface

warming (Chapman and Walsh 2007a) and, therefore, on the sea-ice decrease (Leibowicz et al. 2012; Bennartz et al. 2013; Liu and Key 2014; Van Tricht et al. 2016).

1.2 Clouds and their role in the climate system

As clouds have an important effect on arctic surface temperature, we briefly describe their formation, microphysical parameters, and radiative forcing at the top of atmosphere and at the surface in the Arctic.

1.2.1 Cloud formation

Cloud formation requires both air that is sufficiently cool and moist as well as the presence of condensation nuclei. Aerosol particles provide sites for the water vapor to adhere. If the air is cool enough, the temperature is below the dew point allowing condensation to take place (Lamb and Verlinde 2011). After cloud droplet formation, cloud droplets grow to 10 μm by vapor deposition, droplet collision, and coalescence for liquid clouds or by vapor deposition, riming, and the Bergeron process for mixed-phase and ice clouds (Pruppacher and Klett 1997).

Liquid nucleation occurs when a gas phase is supersaturated with respect to liquid water. The liquid nucleation without the presence of aerosol particles, the so-called homogeneous nucleation, requires an RH greater than 400% due to the Kelvin Effect (Thomson 1872), which is not observed in the atmosphere (Madonna et al. 1961; Heist and Reiss 1973; Pruppacher and Klett 1997). The presence of particles decreases the radius of curvature of the water surface, leading to a decrease in latent heat of evaporation (Pruppacher and Klett 1997). Those particles are aerosols and act as cloud condensation nuclei (CCN) for heterogeneous nucleation.

1.2.2 Cloud extinction of radiation

The interaction of radiation with matter leads to a decrease in radiative power. This is the extinction phenomenon. Let an infinitesimal atmospheric layer with a thickness ds be composed of particles or cloud droplets, then the incoming radiation with intensity I_0 (W m^{-2}) that crosses the layer and exits with intensity I_0+dI, can be expressed by (Fig. 1.3)

$$dI = -\sigma_e I_0 ds, \tag{1.1}$$

where σ_e (m^{-1}) is the extinction coefficient.

A particle can either absorb or scatter the light. We can characterize the scattering and absorption coefficient contributions to the extinction coefficient

$$\sigma_e = \sigma_a + \sigma_{sca} \tag{1.2}$$

with σ_a and σ_{sca}, respectively, the absorption and scattering coefficients.

To characterize the relative importance of scattering versus absorption, the single scattering albedo is introduced as:

$$\tilde{\omega} = \frac{\sigma_{sca}}{\sigma_e} = \frac{\sigma_{sca}}{\sigma_{sca} + \sigma_a}, \tag{1.3}$$

where $\tilde{\omega}$ ranges from 0 to 1 and for a nonabsorbing medium $\tilde{\omega}$ equals to 1.

For a finite layer thickness between s_1 and s_2 (Fig. 1.3), instead of the infinitesimal ds, Beer-Lambert's law gives

$$I(s_2) = I(s_1)e^{-\tau_e} \tag{1.4}$$

with

$$\tau_e = \int_{s_1}^{s_2} \sigma_e(s)ds, \tag{1.5}$$

where τ_e is the extinction optical depth (unit less).

Descriptions of radiative cloud properties usually invoke the plane parallel assumption: Horizontal variations are neglected in the atmosphere compared to vertical variations (Hansen and Travis 1974). Since parameters do not depend on horizontal distance x and y but depend only on vertical distance z, we can assume that

$$\sigma_e(s) = \sigma_e(x, y, z) \sim \sigma_e(z). \tag{1.6}$$

We can also express the optical depth by:

$$\tau = \int_0^h \int_0^\infty r^2 Q_E(r/\lambda) n(r, z) dr dz, \tag{1.7}$$

with $Q_E(r/\lambda)$ the extinction efficiency, λ the wavelength, $n(r, z)$ the droplet distribution, and r the droplet radius. Q_E varies with r/λ and converges to 2 when r/λ is large. At solar wavelengths and cloud droplet distributions around 10μm, the approximation Q_E =

2 is justified. By considering that physical parameters do not vary within the cloud, we finally have:

$$\tau = 2\pi N_c \bar{r}^2 h, \tag{1.8}$$

where $\bar{r}$ is the mean cloud droplet size and N_C the droplet number concentration.

The optical depth depends on vertical extension, cloud droplets, and physical constitution through absorption properties (crystals, drops, droplets).

1.2.3 Cloud-droplet effective radius

In order to describe the droplet size distribution, the mean particle size through the arithmetic mean should be the optimal parameter to represent cloud droplet size distribution:

$$\bar{r} = \frac{\int_0^\infty r n(r) dr}{\int_0^\infty n(r) dr} = \frac{1}{N} \int_0^\infty r n(r) dr, \tag{1.9}$$

where N is the particle concentration.

From a remote-sensing point of view, however, we are more interested in defining the scattered light. Since each particle scatters an amount of light proportional to $\sigma_{sca} = \pi r^2 Q_{sca}$, the mean radius of scattering is defined by (Hansen and Travis 1974):

$$r_{sca} = \frac{\int_0^\infty r \pi r^2 Q_{sca}(x, n_r, n_i) n(r) dr}{\int_0^\infty \pi r^2 Q_{sca}(x, n_r, n_i) n(r) dr}, \tag{1.10}$$

where Q_{sca} is the scattering efficiency. It is not convenient to retrieve Q_{sca} from measurements, but if r is applied to cloud droplet ($\sim 10\,\mu$m) and if visible wavelengths are considered, Q_{sca} approximates to two, and we can define the effective radius as

$$r_e = \frac{\int_0^\infty r^3 n(r) dr}{\int_0^\infty r^2 n(r) dr}. \tag{1.11}$$

1.2.4 Liquid water path

The Liquid water content (LWC), expressed in $\mathrm{g\,m^{-3}}$, is the mass of condensed liquid water per cubic meter in the cloud. In terms of a population of cloud droplets, the LWC can be expressed as

$$LWC = \frac{4}{3} \rho_w \pi r^3 N_C, \tag{1.12}$$

where ρ_w is the bulk density of liquid water, N_C the concentration of liquid-cloud droplets, and r the volume weighted mean radius. The Liquid Water Path (LWP) is defined as

$$LWP = \int_{z=0}^{h} LWC dz \tag{1.13}$$

for a cloud with a base at z $= 0$ and a cloud thickness of h. LWP is a measure of the column liquid water amount present between two vertical positions in the atmosphere.

A question remains on how we can link cloud radiative parameters to radiative forcing. In the next section, we introduce the radiative transfer equation to link cloud optical properties to their radiative properties and estimate their forcing.

1.2.5 Cloud radiative properties and cloud radiative forcing

In the atmosphere, single scattering alone is not realistic and has been called "utterly useless" for treating solar radiation in clouds (Hewson and Longley 1944; Goody and Yung 1995; Petty 2006). Clouds are optically thick and weakly absorbing at visible wavelengths ($\tilde{\omega}$ close to 1), so multiple scattering cannot be ignored (Petty 2006).

Based on energy conservation, a differential change in intensity dI can be due to a change in extinction, in emission, or radiation scattered into the beam from other directions.

$$dI = dI_{ext} + dI_{emit} + dI_{scat}. \tag{1.14}$$

The differential form of the radiative transfer equation is given by (Petty 2006):

$$\frac{dI(\hat{\Omega})}{d\tau} = I(\hat{\Omega}) - J(\hat{\Omega}) \tag{1.15}$$

where $\hat{\Omega}$ is the direction of interest and J is the source function which lump all sources of radiation and is given by:

$$J(\hat{\Omega}) = (1 - \tilde{\omega})B + \frac{\tilde{\omega}}{4\pi} \int_{4\pi} p(\hat{\Omega}', \hat{\Omega}) I(\hat{\Omega}') d\omega, \tag{1.16}$$

where ω is the angular frequency, $\tilde{\omega}$ is the single scattering albedo, B is the Planck function which depends on wavelength and temperature, and $p(\hat{\Omega}', \hat{\Omega})$ is the scattering phase function for arbitrary combinations of incoming and scattering directions.

Cloud-free scene and horizontally extensive and homogeneous stratiform clouds are problems for which the plane parallel approximation is realistic.

To adapt Eq. (1.15) to the plane parallel atmosphere, we define $\mu = cos(\theta)$ to state the direction of propagation of the radiation measured from zenith. Moreover the radiation-beam contribution to the horizontal flux does not depend on the azimuthal angle. These assumptions simplify Eq. 1.15 to

$$\mu \frac{dI(\mu)}{d\tau} = I(\mu) - \frac{\tilde{\omega}}{2} \int_{-1}^{1} p(\mu, \mu') I(\mu') d\mu'. \tag{1.17}$$

The two-stream method is a method which aims to link the intensity I_0 with the intensity at a definite layer $I(\tau)$, the optical depth, and the albedo. The two-stream method assumes that the intensity $I(\mu)$ is constant in each hemisphere:

$$I(\mu) = \begin{cases} I^{\uparrow} & \mu > 0 \\ I^{\downarrow} & \mu < 0 \end{cases} \tag{1.18}$$

with both $I^{\uparrow}$ and $I^{\downarrow}$ constants.

We do not describe all the steps needed to state the final solution but it can be found in every good handbook about atmospheric radiation (Petty 2006). More assumptions have to be made: the lower boundary is considered as black (no upward reflected radiation at $\tau = \tau^*$ with τ^* the total atmospheric optical depth), the azimuthally averaged backscatter fraction $\bar{b}$ varies linearly with the asymmetry factor g, and the averaged intensity I_0 incident on the top of the atmosphere is known. The two-stream method finally retrieves $I^{\uparrow}$ and $I^{\downarrow}$ as:

$$I^{\uparrow}(\tau) = \frac{r_{\infty} I_0}{e^{\Gamma\tau^*} - r_{\infty}^2 e^{-\Gamma\tau^*}} \left[e^{-\Gamma(\tau^* - \tau)} - e^{-\Gamma(\tau^* - \tau)} \right] \tag{1.19}$$

$$I^{\downarrow}(\tau) = \frac{I_0}{e^{\Gamma\tau^*} - r_{\infty}^2 e^{-\Gamma\tau^*}} \left[e^{-\Gamma(\tau^* - \tau)} - r_{\infty}^2 e^{-\Gamma(\tau^* - \tau)} \right] \tag{1.20}$$

with $\Gamma = 2\sqrt{1 - \tilde{\omega}}\sqrt{1 - \tilde{\omega} g}$, and r_{∞} a parameter dependent on $\tilde{\omega}$ and g.

From the intensity, we can derive the flux F: the two-stream method assuming an isotropic intensity within each hemisphere $F = \pi I$. The net Flux is then equal to

$$F^{net} = \pi (I^{\uparrow} - I^{\downarrow}). \tag{1.21}$$

We do not go through mathematical developments but the general expressions for the total albedo (the fraction of incident radiation that is reflected, r), and the total transmittance (t fraction of radiation that goes from the source through the entire atmosphere), are equal to

$$r = \frac{r_\infty \left[e^{\Gamma\tau^*} - e^{-\Gamma\tau^*}\right]}{e^{\Gamma\tau^*} - r_\infty^2 e^{-\Gamma\tau^*}} \tag{1.22}$$

$$t = \frac{1 - r_\infty^2}{e^{\Gamma\tau^*} - r_\infty^2 e^{-\Gamma\tau^*}}. \tag{1.23}$$

Small changes in $\tau*$ can have a large impact on the albedo. For example, Petty (2006) has shown that for $\tilde{\omega}$ equals to 1, an increase of τ^* from 0 to 10 changes the albedo from 0 to 0.6. The radiative transfer equation and its associated assumptions help to associate measured observables (e.g., $I^{\downarrow}$) and components of the system (e.g., I_0) to cloud radiative properties (r, t). The different results aim to associate cloud radiative effects to cloud microphysical properties.

Here we presented the two-stream method as an approximated but convenient way to relate cloud microphysical properties to their radiative properties and evaluate their forcing. However, several methods can be used to relate microphysical and radiative parameters: the doubling or adding method (Van de Hulst and Irvine 1963), successive orders of scattering (Van de Hulst 1948), iteration of formal solution (Herman and Browning 1965), invariant imbedding (Ambartsumian 1942), spherical harmonics (Lenoble 1961), Monte Carlo (Hammersley and Handscomb 1964), and so forth.

1.2.6 Cloud radiative impacts in the Arctic

Clouds have a large impact on the surface temperature in the Arctic (Serreze and Barry 2011). Walsh and Chapman (1998) measured from ground-based stations that overcast temperatures are 6 to 9°C higher than clear-skies temperature from September to March.

Depending upon their altitude and optical thickness, clouds have varying impacts on the radiation budget (Hartmann et al. 1992). A high and cold cloud, such as a cirrus, can be transparent to shortwave radiation and has a low reflective impact on incoming solar radiation. At the same time, it absorbs the outgoing longwave radiation and decreases the energy emitted out into space. High and cold clouds tend to warm the surface and the troposphere, acting as a cloud greenhouse forcing.

In contrast, low and thick clouds reflect more shortwave radiation into space than high thin clouds. Low-altitude-cloud tops also have temperature similar to that of surfaces. Therefore, contrasts in emitted longwave radiations between cloud free scenes or cloudy

scenes are small. The net effect of those clouds is the cooling of the surface and the troposphere.

In the Arctic, both clouds and surface contribute to the variability in shortwave radiative forcing at the top of the atmosphere (Qu and Hall 2005). A decrease in cloud fraction drives an increase of the net top-of-atmosphere shortwave in the early summer (Kay and L'Ecuyer 2013) and a decrease in sea-ice extent drives the increase of the net top-of-atmosphere shortwave in the late summer (Kato et al. 2006; Kay and L'Ecuyer 2013). Cloud radiative properties therefore have a significant impact on their net forcing of the Arctic region.

The radiative forcing is the impact of clouds on radiative fluxes and determined as the difference between all-sky and clear-sky fluxes (Ramanathan et al. 1989). The seasonal variability of arctic-cloud radiative properties is significant (Kay and L'Ecuyer 2013). At the top of the atmosphere and at the surface shortwave radiative forcing is null during the polar night due to the absence of sun irradiance. From Clouds and the Earth's Radiant Energy System-Energy Balanced and Filled (CERES-EBAF) (Loeb et al. 2009) radiative fluxes, Kay and L'Ecuyer (2013) created a cloud and radiation climatology above the ocean. During summer the shortwave radiative forcing is maximal of -75 $\mathrm{W\,m^{-2}}$ for both top of atmosphere and surface. On average the shortwave radiative forcing is -31 $\mathrm{W\,m^{-2}}$ at the top of the atmosphere and -32 $\mathrm{W\,m^{-2}}$ at the surface. The cloud longwave radiative forcing is positive and close to the same value throughout the year: 19 $\mathrm{W\,m^{-2}}$ at the top of the atmosphere and 42 $\mathrm{W\,m^{-2}}$ at the surface. The annual mean arctic-cloud forcing results show a warming effect at the surface and a cooling effect a the top of the atmosphere (Schweiger and Key 1994; Intrieri 2002; Dong et al. 2010; Zygmuntowska et al. 2012): Kay and L'Ecuyer (2013) retrieves an annual mean arctic-cloud forcing at the top of atmosphere of -12 $\mathrm{W\,m^{-2}}$ and an annual mean arctic-cloud forcing at the surface of 10 $\mathrm{W\,m^{-2}}$.

1.3 Aerosols in the Arctic

A key driver of cloud radiative properties is the impact of aerosols on available CCN, and their related interactions with cloud microphysical properties. The fourth assessment IPCC, based on two modeling studies (Stevenson et al. 2013; Shindell et al. 2009), evaluated the impact of aerosols on cloud radiative properties to -0.45 $\mathrm{W\,m^{-2}}$. However, the poor

understanding of aerosol-cloud interactions leads to a large uncertainty of this value from -1.2 to 0.0 $W\,m^{-2}$. Aerosol-cloud interactions therefore have a highly uncertain, though potentially large impact on the total radiative forcing, especially when comparing to the radiative forcing from anthropogenic emissions (CO_2) of about 1.68 $W\,m^{-2}$.

Even if the Arctic is far from the major aerosol sources present in midlatitudes (Barrie 1986; Jiao and Flanner 2016), the arctic region is influenced by various types of aerosols (Stohl 2006). Natural aerosols from desert, marine, volcanic, and biogenic sources represent 90% of the total mass of emitted particles (Satheesh and Krishnamoorthy 2005); Anthropogenic aerosols from industry, transportation, ships, and domestic sources comprise the remainder. Nevertheless, the majority of aerosols in the Arctic originates from fossil fuel (Singh et al. 2010; Villiers et al. 2010) or biomass burning (Stohl and James 2005; Koch and Hansen 2005). Volcanic and desert dust particles can be present in the Arctic, but such events are not common (Xie 1999; Hirdman et al. 2010; McCoy and Hartmann 2015; Schmidt et al. 2015). Local sources such as flaring and ship transportation contribute to the total arctic aerosol concentration (Lamarque et al. 2010), however, their contribution remain currently limited, for example, the black-carbon deposition from these sources is less than 1% of the total (Browse et al. 2013).

During winter, the Arctic is well known for the presence of arctic Haze: a thick layer of aerosols with an anthropogenic signature (Barrie 1986; Shaw 1995; Stohl 2006; Quinn et al. 2007b; Law and Stohl 2007). On the contrary, during summer when temperature and humidity increase, precipitation washes aerosols from the atmosphere. The arctic atmosphere becomes extremely clean, consistent with a location remote from industrialized areas (Quinn et al. 2002; Garrett et al. 2010, 2011).

Aerosols arrive in the Arctic by a variety of pathways. Law et al. (2014) illustrated the pathways from Stohl (2006), presented in Figure 1.4. Figure 1.4 refers to the Arctic front and the polar dome. The polar dome separates the cold air in the Arctic from the midlatitude warmer air. The polar dome plays an important role in aerosol transport (Klonecki et al. 2003; Stohl 2006). The polar dome boundary, or arctic front, varies from as far south as 40°N in winter to north of 70°N in the North Atlantic Ocean.

Stohl (2006) described pathways of air parcels from midlatitude sources to the Arctic using a black-carbon (BC) passive tracer from the numerical tracer transport model FLEX-

PART (FLEXible PARTicle) (Stohl et al. 1998, 2005). We associate the 9 pathways from Figure 1.4 to the 3 pathways described by Stohl (2006).

Rapid transport from European sources at high latitudes takes 4 days to reach the Arctic. Air-parcel transport is low-level, about 950 hPa, into the Arctic and then lifted at the arctic front. Uplift and precipitation occur north of the polar front so this pathway is very efficient for allowing aerosol deposition into the Arctic when the arctic front is located at the northern limit. This pathway corresponds to transport 1 in Figure 1.4.

Taking approximately 10 to 15 days, low-level transports from European or high-latitude Asian sources are characterized by cold-air transport into the polar dome. This pathway occurs mainly during winter and early spring (Klonecki et al. 2003). This pathway corresponds to transport 3 in Figure 1.4.

Air parcels are lifted close to the source by conveyor belt (Stohl et al. 2007; Brock et al. 2011) and are subjected to cycles of upward and downward transport or high-latitude transport. Finally air parcels descend into the polar dome. Precipitation is efficient outside the Arctic for this transport pathway and concerns air parcels from North America and East Asia. This pathway corresponds to transports 2, 4, 5, 6, 7, and 8 from Figure 1.4.

1.4 Impact of aerosols on liquid-cloud microphysical properties

Under appropriate circumstances aerosols can serve as CCN (Fletcher et al. 1962). Higher CCN concentrations lead to high droplet concentrations. For a given LWC, this results in smaller droplets (Hobbs et al. 2000; Wood 2006). Twomey (1977) has shown that one of the consequences of clouds with smaller droplets and constant LWC is an increase of τ, known as the first indirect effect (Twomey 1974). The increase of τ makes the cloud brighter and more reflective. The final effect is the increase of the planetary albedo, causing profound long-term effect on climate (Twomey 1974). This effect has been observed by in situ measurements (Coakley et al. 1987), airborne observations (Brenguier et al. 2000), ground-based measurements (Feingold 2003b), and satellite measurements (Han et al. 1998; Breon et al. 2002; Painemal and Zuidema 2013a). The well-known ship track feature is a striking example of this phenomenon as shown by Figure 1.5. By burning fuel oil with a high sulfur content, ships emit aerosols into the atmosphere, which then act as CCN in

clouds. Clouds in the track become brighter. This effect is easily recognizable when local air parcels are considered (Radke et al. 1989; Christensen et al. 2014), but it is more difficult when air parcels are considered from long-range transport (Durkee et al. 2000; Coakley and Walsh 2002; Stevens and Feingold 2009).

A direct consequence of the cloud-droplet radius reduction is a lifetime effect (Albrecht 1989). When the mean droplet size is decreased by the presence of CCN, the drizzle production is reduced. The LWC is increased and so is the cloudiness fraction. This describes another cooling effect induced by the aerosols. Nevertheless, Stevens and Feingold (2009) have shown that this effect can be disproved. If less precipitation happens, more liquid is lofted to cloud top leading to deeper clouds. Deeper clouds produce more rain, offsetting the initial suppression of precipitation (Stevens 2007; Stevens and Seifert 2008).

Dry air entrained into a cloud top evaporates cloud droplets (Ackerman et al. 2004). The evaporation process is fastest when the droplet radius is small. High concentrations of CCN favor the preferential evaporation of these smaller droplets leading to an increase in the mean droplet radius. The increase of droplet radius decreases the cloud reflectivity (Twomey 1977). This result explains the possible overestimation of the first indirect effect by previous studies (Haywood and Boucher 2000).

1.4.1 The Aerosol-cloud parameter

The link between r_e and N_C described by Eq. (1.12) yields the following relationship when LWP is considered constant:

$$\frac{d\,ln\,r_e}{d\,ln\,N_C}\,|_{LWC} = -\frac{1}{3} \tag{1.24}$$

An aerosol-cloud interaction parameter can be defined as the change of a cloud parameter (e.g., r_e) as a function of an aerosol proxy (α) (Feingold et al. 2001):

$$ACI = -\frac{d\,ln\,r_e}{d\,ln\alpha} \tag{1.25}$$

One of the advantages of using the ACI is that we are not looking at absolute, but rather at relative changes. The value of ACI is less affected by the underestimation or overestimation of measurements or models.

If we consider that N_c is linearly related to CCN concentrations and CCN concentrations are proportional to the aerosol proxy (α), Eq. (1.24) yields a theoretical value for

the ACI of $\frac{1}{3}$. Most of the time, however, CCN is not the only factor that impacts the value of r_e, because cloud formation and properties are at first order primarily driven by meteorological conditions as described later in Section 1.6. Previous studies considered different parameters for aerosol quantities: The AOD (Feingold et al. 2001; Lohmann and Feichter 2004), the aerosol index (Breon et al. 2002; Matsui et al. 2006), the CCN concentration (McComiskey et al. 2009; Zamora et al. 2015), or the aerosol extinction (Feingold 2003b). The retrieved ACI values from the studies cited above are smaller than the $\frac{1}{3}$ threshold, most certainly due to the impact of meteorological parameters (Unger et al. 2009; McComiskey et al. 2009; Zamora et al. 2015).

1.4.2 Aerosol-cloud interaction from different methods

Due to the potential climate impact of aerosol-cloud interactions and our poor understanding of their magnitude (Kristjánsson 2002; Stevens and Feingold 2009), the scientific community has been stimulated and many previous works have been aimed to analyze, understand, and quantify the interaction between aerosols and clouds. Warm clouds have been studied using data from ground-based observations and retrieved an ACI range between 0.01 and 0.36 (Feingold 2003b; Garrett et al. 2004; Kim et al. 2008; Lihavainen et al. 2008; McComiskey et al. 2009; Kim et al. 2012; Schmidt et al. 2014; Sarna and Russchenberg 2016). Airborne observation from field campaigns yielded ACI ranging from 0.05 to 0.33 (Raga and Jonas 1993; Martin et al. 1994; Gultepe et al. 1996; O'Dowd et al. 1999; McFarquhar and Heymsfield 2001; Ramanathan 2001; Twohy 2005; Lu et al. 2007, 2008; Terai et al. 2012; Painemal and Zuidema 2013a; Zamora et al. 2015), satellite observations retrieved an ACI range between 0.02 and 0.17 (Nakajima et al. 2001; Sekiguchi 2003; Quaas 2004; Quaas et al. 2005; Kaufman et al. 2005; Lebsock et al. 2008; Bulgin et al. 2008; Sporre et al. 2012; Costantino and Bréon 2013), and satellites with models observed ACI ranging between 0.01 and 0.17 (Breon et al. 2002; Chameides et al. 2002; Avey et al. 2007; Tietze et al. 2011).

The results come out with a high diversity in regions of interest, types of clouds, types of aerosols, instruments, or methods. For example, the spatial resolutions for aircraft and ground-based measurements are generally below 20 km whereas satellite spatial resolution can go up to 400 km (McComiskey and Feingold 2012). The particular problem of

the spatial resolution has been demonstrated to influence the aerosol-cloud interaction retrievals' sensitivity. McComiskey and Feingold (2012) also detailed the importance of constraining for parameters, such as LWP and the separation in space of cloud and aerosol properties. Without sufficient constraints "aerosol-cloud interaction studies" are more likely representative of "aerosol-cloud interaction studies associated with their feedback."

Each method presents a set of associated advantages and weaknesses. Airborne in situ studies retrieve extremely accurate properties and can retrieve robust measurements of the cloud droplet size, aerosol concentration within the cloud droplet and radiation impacts. Unfortunately, these methods give temporally and geographically localized measurements. It is difficult to compare those studies and generalize their results.

Ground-based measurements offer the possibility to have long term measurements over several seasons, but they are geographically localized.

Satellite measurements provide geographically large and temporally long measurements, but unfortunately the resolution is coarse compared to the methods described above. Also, satellites cannot usually retrieve cloud properties and aerosol content at the same location and time due to cloud brightness. Satellite studies often consider air parcels just next to the cloud or use active satellites and consider aerosols above the cloud top to retrieve the information of the presence of CCN within the clouds. This method is intrinsically biased.

The last method considers satellite measurements coupled with a numerical tracer transport model. The satellite observations are used to retrieve cloud properties, and the numerical tracer transport model provides information regarding the aerosol content. Cloud properties are temporally and geographically colocated with aerosol content. The advantage of coupling satellite data with a numerical tracer transport model is that datasets are decoupled from each other so they cannot influence one another.

McComiskey and Feingold (2012) reviewed studies that provide an ACI index, and we add values from more recent studies and studies focused in the arctic region in Table 1.1. In Table 1.1 not every study retrieved ACI. For example, from Eq. (1.24) it can be deduced that $ACI_{r_e} = ACI_{N_c}/3$, and if LWP is constrained then $ACI_{r_e} = ACI_{\tau}$. From Table 1.1, we see that the ACI parameter spans the entire physically meaningful range of the first indirect effect between 0 and 0.33 with an average of 0.14. McComiskey and Feingold (2012) noted

that higher ACI values are associated with studies using higher spatial resolution — The average of ground-based and airborne studies is respectively 0.16 and 0.19 and coarser resolution studies with satellite only and satellite+model data are respectively 0.09 and 0.11.

Regarding the studies based on the Arctic, the ACI values are comprised between 0.05 and 0.17 and the average (0.15) is a bit higher than the average considering all regions (0.14).

It is difficult to compare all these studies since they used different methods to represent cloud, aerosol properties, and focus on different regions (Sena et al. 2016).

Results from other studies cannot be converted to ACI parameters. Andersen and Cermak (2015) favored the study of the correlation between r_e and aerosol index for different meteorological regimes from satellite data, but did not retrieve the slope of $\ln(r_e)$ as function of ln(AI). Chen et al. (2014) focused on the analysis of the slope of r_e as a function of ln(AI), but the absence of use of the logarithmic function for the cloud microphysical parameters prevents estimation of ACI parameters.

1.4.3 Aerosol-cloud interactions from satellite and models

A passive tracer can be used as a proxy for aerosols for the purpose of studying aerosol-cloud interactions (Avey et al. 2007; Brioude et al. 2009; Garrett et al. 2010; Tietze et al. 2011; Yang et al. 2015). An advantage of using a passive tracer is that, while aerosols interact with cloud properties, in return cloud properties interact with aerosols, in a coupled system, it becomes labyrinthine to reveal an effect of aerosols on clouds (Stevens and Feingold 2009). Any effect can diminish, cancel, or enhance its own effect through positive and negative feedbacks.

Figure 1.6 shows different cases of pathways whether the pollution plume contains CCN or not. In Figure 1.6 the passive tracer is the carbon monoxide (CO), described in Section 2.2.1. Let's consider that meteorological parameters are perfectly controlled and that only aerosols impact cloud microphysical properties. If there is no precipitation, both aerosols and CO from the source arrive in the Arctic. If aerosols are CCN, they change microphysical properties of clouds. The variation of CO is associated with a variation of cloud microphysics. Thus, we can assess the impact of aerosols. If aerosols are not CCN,

then the CO variation is not associated with cloud property variation, we can then assess that aerosols do not influence cloud microphysics.

The use of a passive tracer does not only have advantages. The main problem comes when there is precipitation while pollution plumes are en route to the Arctic. In this case, aerosols are scavenged, whereas the passive tracer remains in the atmosphere, both passive tracer and aerosols are decorrelated. Thus, CO variations are no longer associated with a change in cloud microphysics. Where precipitation occurs on the way to the Arctic, we cannot assess the nature of aerosols. We can only conclude about the sensitivity of clouds to long-range transport of pollution plumes. From a climate impact standpoint, it is ultimately what we are the most interested in: if all aerosols are immediately scavenged after emission, we do not care about aerosols' effect on arctic clouds.

If we consider in Eq. (1.25) that the aerosol proxy (α) is the passive tracer concentration (χ_α), we define a new parameter, the net ACI (ACI^{net}) as the ACI defined in Section 1.4.1 minus aerosol-scavenging interactions (ASI)

$$ACI^{net} = ACI - ASI. \tag{1.26}$$

ACI^{net} represents the impact of aerosols assuming no dry or wet scavenging en route to the Arctic ($ASI = 0$). ACI^{net} is defined as

$$ACI_{r_e}^{net} = -\frac{d\,ln\,r_e}{d\,ln\,\chi_\alpha} \tag{1.27}$$

and

$$ACI_{\tau}^{net} = \frac{d\,ln\,\tau}{d\,ln\,\chi_\alpha}. \tag{1.28}$$

We expect a decrease in r_e and an increase in the optical depth when the χ_α increases, so ACI_{τ}^{net} and $ACI_{r_e}^{net}$ are expected to be positive.

Since τ can be expressed by:

$$\tau = \frac{3}{2}\frac{LWP}{\rho_w r_e} \tag{1.29}$$

the derivative of τ with respect to χ_α is

$$\frac{d\,ln\,\tau}{d\,ln\,\chi_\alpha} = -\frac{d\,ln\,r_e}{d\,ln\,\chi_\alpha} + \frac{d\,ln\,LWP}{d\,ln\,\chi_\alpha} \tag{1.30}$$

given the LWP constant,

$$ACI_{\tau}^{net} = ACI_{r_e}^{net} \tag{1.31}$$

If the ACI^{net} is close to $\frac{1}{3}$ it means that the passive tracer is perfectly correlated with CCN and that meteorological variability is sufficiently controlled to not influence ACI (Feingold et al. 2001). If ACI^{net} is close to 0, there are two possibilities: (i) aerosols do not act as CCN and do not impact cloud properties or (ii) aerosols have been scavenged before reaching the Arctic (Garrett and Zhao 2006; Garrett et al. 2010).

1.4.4 Impact of aerosols on liquid-cloud radiative forcing

Zhao and Garrett (2015) used ground based measurements in Barrow (Alaska) from 2000 to 2003 and retrieved monthly mean of shortwave and longwave cloud radiative forcing under different aerosol regimes. Figure 1.7, from Zhao and Garrett (2015), shows aerosol impacts on arctic liquid-cloud radiative forcing: the change of cloud shortwave radiative forcing due to pollution events ranges from 0 in winter to -12.6 $W\,m^{-2}$ in summer and the change of cloud longwave radiative forcing due to pollution events ranges from 8.1 in fall to 9.9 $W\,m^{-2}$ in spring. Regarding the seasonal cloud radiative forcing, the aerosol-cloud interactions decrease the longwave cloud radiative forcing to 14% in summer and increase the shortwave cloud radiative forcing to 33% in spring.

1.5 Impact of aerosols on ice-cloud microphysical properties

Liquid clouds are present in the atmosphere at temperature well below the melting point of ice (T_m =0°C). Even if the potential energy of the solid phase is lower than the potential energy of the liquid phase, the system needs a certain amount of energy ΔG_i^* to reach the more favorable stage. In fact, liquid-phase molecule liaisons have to be broken in order to be orderly arranged in the ice lattice (Lamb and Verlinde 2011). Since observations show that homogeneous nucleation occurs at about -38°C in the atmosphere (Rosenfeld and Woodley 2000; Heymsfield et al. 2005; Hu et al. 2010), the heterogeneous nucleation, by the presence of an ice nuclei (IN), increases the freezing temperature from -38°C to T_m (Rogers et al. 1998; DeMott 2003; Sassen et al. 2003; Lamb and Verlinde 2011). Thus the premature ice-crystal formation, by heterogeneous nucleation compared to homogeneous nucleation, can decrease significantly the cloud lifetime by favoring precipitation (DeMott et al. 1998). Unfortunately, improvement in heterogeneous nucleation still needs to be achieved (Szyrmer and Zawadzki 1997; Lin et al. 2002; Kärcher 2003) and is even qualified

as ”desperately needed” (Cantrell and Heymsfield 2005).

1.5.1 Nature of ice nuclei

Insoluble foreign particles create a lattice that helps water molecules to be spatially organized close to the crystalline structure of ice (Mason 1961). On the opposite side, foreign soluble particles can decrease the freezing temperature (Rasmussen 1982; Sassen and Dodd 1988). Ice nuclei (IN) can be mineral dusts (Rogers et al. 1998; DeMott et al. 2003) for which the supercooling temperature can be as low as -5.2°C (Sassen 2003). Organic materials associated with biomass burning can also act as efficient IN and increase freezing temperatures to -1°C (Fukuta and Mason 1963; Popovitz-Biro et al. 1994). Efficient IN are usually aerosols with a crystalline structure close to the lattice of ice (Lamb and Verlinde 2011).

1.5.2 Modes of action

Aerosols impact cloud phase transitions through 4 modes of actions (Pruppacher and Klett 1997). In *deposition nucleation*, water vapor is supersaturated with respect to ice, but subsaturated with respect to liquid. The ice forms on the IN surface from the water vapor by the Bergeron process (Pruppacher and Klett 1997). In *contact nucleation*, the IN impinges upon a droplet surface and leads to a decrease in the energy barrier at the three-phase contact line (Djikaev and Ruckenstein 2008; Gurganus et al. 2014). A laboratory study has shown that the nature of aerosol does not matter and just an impact induces the phase transition (Niehaus and Cantrell 2015). This study concluded that not only do aerosols act as IN in the contact nucleation, but so do other particles, such as cloud droplets which can initiate freezing by colliding each other. *Immersion freezing* is when the ice forms on the IN which is immersed in a supercooled liquid-water droplet. *Condensation freezing* occurs when ice forms on the IN surface after condensation occurs. The last two modes, immersion freezing and condensation freezing, needs a higher relative humidity than the other nucleation processes, a supersaturated water vapor with respect to liquid, which is less likely to occur in the Arctic compared to the first two modes.

1.5.3 Theory of heterogeneous nucleation

The classical approach to ice nucleation assumes that ice embryos form randomly on the IN's surface. The IN decreases the free-barrier energy ΔG_i*, and the rate of nucleation J by a particle takes the general form

$$J = K_X exp(-\frac{\Delta G^*}{k_b T}), \tag{1.32}$$

where K_X is a kinetic coefficient adapted to vapor or liquid parent phase X. The heterogeneous ice nucleation assumes that an ice embryo is in contact with the IN and with the parent phase (vapor or liquid).

The magnitude of the energy barrier is a competition between three terms: the contribution from the volume of ice fragment, which decreases the energy, the contribution of the interface between the parent phase and ice, which increases the energy, and the contribution of the interface between the ice embryo and the IN, which lowers the free energy of the system. The free energy to form an ice embryo can be derived as

$$\Delta G_X = -n_I V_I \Delta \mu_{XI} + A_{IX}\sigma_{IX} - A_{IN}\sigma_{IX} m_X, \tag{1.33}$$

where V_I is the volume of the ice embryo, A_{IX} is the area of the interface between the embryo and the parent phase, A_{IN} is the ice-nucleus interfacial area, and n_I is the molar density of ice. Figure 1.8 represents the free-energy ΔG as a function of the ice embryo radius.

From Eq. (1.33), the critical point of the function, the critical radius r*, is derived as the point where the contribution of both the volume of ice fragment and interface between the ice embryo and the IN is greater than the contribution of the interface between the parent phase and ice. The critical radius of an ice embryo ($r*$) which leads to the phase transition of the droplet and depends on the interfacial free energy between the parent phase and the ice. r* is derived as (Pruppacher and Klett 1997)

$$r_X^* = \frac{2\sigma_{IX}}{n_I \Delta \mu_{XI}}, \tag{1.34}$$

where $\mu_X I = \mu_X - \mu_I \propto \Delta T_s / T_m$ is the chemical potential of bulk parent phase relative to the chemical potential of ice, with ΔT_s the supercooling temperature.

The free energy at r^* leads to the free-energy barrier height (ΔG^*)

$$\Delta G_X^* = \Delta G_X(r^*) = \frac{16\pi\sigma_{IX}^3}{3(n_i\Delta\mu_{XI})^2} \cdot f(m_X, r_N) \propto \frac{f'(m_X, r_N)}{\Delta T_s^2}, \tag{1.35}$$

where r_N is the radius of the nucleus, $f(m_X, r_N)$ is a geometrical factor less than 1 and represents the decrease of the free-energy barrier due to the presence of the foreign particle, and $f'(m_X, r_N)$ regroups the different constants. Referring to Eq. 1.32, the increase of the nucleation rate J is favored by a decrease in the free-energy barrier. If ΔG^* is considered constant and ΔT decreases, the parameter f' has to decrease. Thus, the presence of particles decreases the free-energy barrier, and therefore increases the nucleation rate.

1.6 Influence of meteorological parameters on cloud microphysical parameters

The primary control of cloud properties is the meteorological state as defined by the humidity, stability, vertical velocity and temperature (Arakawa 1975; Stevens and Brenguier 2009; Shupe et al. 2013). Arctic cloud formation is favored by high humidity (Cox et al. 2015). Droplet concentration and droplet radius decrease with entrainment of dry air within the cloud (Brenguier et al. 2000). Arctic stratus clouds are also favored by lower lower tropospheric stability (LTS) (Klein and Hartmann 1993). Clouds with higher temperatures tend to be more turbulent with greater available moisture, hence they have higher water contents, larger droplets, and are more likely to precipitate (Pruppacher and Klett 1997).

For example, the amount of liquid water in an adiabatic cloud depends on the difference between the moist and dry lapse rates at temperature T and pressure P:

$$\frac{dLWC}{dz} = \frac{\rho_a(T,p)c_p}{L_v}(\Gamma_d - \Gamma_s(T,p)), \tag{1.36}$$

where $\rho_a(T,p)$ is the density of air at pressure p and temperature T, c_p the heat capacity of air, L_v the latent heat of vaporization, and Γ_d, and Γ_s, respectively, the dry and moist adiabatic lapse rates as function of T and p. At colder temperatures the difference between the dry and moist adiabatic lapse rates is smaller due to the reduced moisture available for condensation. For a cloud forming at 900 hPa with a temperature of -15°C, $dLWC/dz$ equals 0.7 g m^{-3} km^{-1}. At 0°C, $dLWC/dz$ equals 1.9 g m^{-3} km^{-1}.

Meteorological parameter variations can be associated and sometime correlated with aerosol concentration or aerosol-type variations (Andrade et al. 1994; Wehner and Wiedensohler 2002; Luo 2003). Pearl (1994) suggested that if two variables (α, r_e) are correlated, but also influenced by a third variable (meteorological parameters or others), it is impossible to determine the real relationship between the two variables unless the third variable is known and measurable. Gryspeerdt et al. (2016) analyzed the relationship between AOD and cloud fraction (CF), using MODIS measurements, and included information on the cloud droplet number concentrations N_C. Their study suggested that the AOD-CF relationship is explained by another factor than N_C. They concluded that the relationship AOD-CF is driven by meteorological parameters, and accounting for this effect the strength of the relationship AOD-CF is reduced to 80%.

A fundamental question is raised: How can we ensure that observed cloud property changes are due to aerosols and not to meteorological regime variations?

During the transport of aerosols from source regions to the Arctic, the meteorological conditions of air parcels can change. Stohl (2006) traced air parcels from Europe and Asia up to the Arctic, using FLEXPART, and looked at the variations of the specific humidity (SH), pressure, temperature, and potential temperature for different pathways as shown in Figure 1.9. Fast transport of aerosols from Europe was associated with an air-parcel SH of approximately $2.5\,\mathrm{g\,kg^{-1}}$ that dropped to $0.5\,\mathrm{g\,kg^{-1}}$ five days later. Fast transport of European and Asian air parcels had SH values that differed by $2\,\mathrm{g\,kg^{-1}}$. According to the source regions, air parcels have distinct meteorological conditions when they arrive in the Arctic.

Shindell et al. (2008) evaluated the contribution of 5 source regions on the aerosol concentrations in the Arctic by using 17 different models: East Asia, South Asia, Europe, Arctic, and North America. Their conclusions showed that aerosols from Europe are the larger contributor to arctic aerosols close to the surface but East-Asian aerosols become more influential with altitude, and are the larger contributor in the upper troposphere. Depending on the source regions, air parcels have distinct aerosol concentrations when they arrive in the Arctic.

In the light of the studies by Stohl (2006) and Shindell et al. (2008), meteorological parameters in the Arctic covary with aerosol concentrations which has been already stated

by studies focused on other regions (Brenguier et al. 2003; Mauger and Norris 2007). If variations in cloud microphysical properties are observed, it is difficult to disentangle the effect of aerosols from meteorological parameters (Stevens and Feingold 2009). In our work, we constrain for meteorological parameters to reduce the correlation with aerosol content. Thus, changes in cloud microphysical parameters are determined by changes in aerosols content.

1.7 Summary of dissertation

In the Arctic, where the warming is two times faster and stronger than midlatitudes, aerosols from midlatitudes have important consequences on cloud properties. Aerosols change the microphysical properties of liquid clouds, but they can also enhance the thermodynamic transition. The work presented in this dissertation aims to quantify and characterize the interaction of pollution plumes with arctic clouds. In order to analyse cloud-aerosols relationships, our study considers measurements from POLDER (POLarization and Directionality of the Earth's Reflectances) (Deschamps et al. 1994) and MODIS (King et al. 1992) satellite instruments, GEOS-Chem (Goddard Earth Observing System) (Bey et al. 2001; Parrington et al. 2012) and FLEXPART (Stohl et al. 1998, 2005) numerical tracer transport models, and ERA-I (ECMWF-Interim) reanalyses from ECMWF (European Centre for Medium-Range Weather Forecasts) (Berrisford et al. 2011). The three primary topics are an evaluation of the effects of pollution plumes on both liquid and ice clouds, and the impact of meteorological parameters on aerosol-cloud interactions.

Table 1.1 reveals that the type of aerosols (Andreae and Rosenfeld 2008), the region, the type of clouds, and meteorological parameters can all influence aerosol-cloud interactions (Sena et al. 2016). However, until now, there has been no study focusing on the influence of anthropogenic and biomass-burning aerosols on liquid and ice arctic clouds, controlling for meteorological parameters by using satellite and model datasets.

By using different and independent datasets, presented in Chapter 2, we can provide a complete analysis of aerosol-cloud interactions for the entire arctic region for a period between 2005 and 2010 above the ocean. In an attempt to disentangle the effect of aerosols from the meteorological parameters, we control for humidity, lower tropospheric stability (LTS), temperature, and LWP to isolate the effect of aerosols on clouds.

The first step, in Chapter 3, is to describe precisely the temporal and geographical variability of the different parameters used in this study. We look at cloud parameters, χ_{CO} from anthropogenic and biomass-burning plumes, and meteorological parameters focused on SH and LTS, vertical, and horizontal winds.

Our first objective has been to quantify the anthropogenic and biomass-burning aerosol effect on liquid-cloud microphysical properties for different meteorological parameters. Results of our analysis are presented in two chapters. Chapter 4 is dedicated to the study of anthropogenic aerosol effects on cloud microphysics. Anthropogenic aerosols are mainly secondary aerosols for which the surface is coated with sulfate, making aerosols soluble in water (Lamb and Verlinde 2011). Solubility in water has been observed to be a key factor allowing an aerosol to act as a CCN (Quinn et al. 2007a). This chapter aims to test the efficiency of anthropogenic aerosols by evaluating the ACI parameter for a particular regime of meteorological parameters. Also we test the efficiency for different meteorological regimes, to answer the following questions: Are meteorological parameters influencing aerosol-cloud interactions (Chen et al. 2014)? Does the dry air inhibit aerosol-cloud interactions (Ackerman et al. 2004)? Does aerosol concentration change the value of the ACI (Andersen and Cermak 2015)?

Chapter 5 compares biomass-burning-aerosol effects with anthropogenic aerosol effects. Biomass burning have been stated as insoluble particle (Costantino and Bréon 2013) unfitting of acting as efficient CCN. Nevertheless, previous studies have concluded that biomass-burning aerosols could act as CCN (Andersen and Cermak 2015) and especially in the Arctic (Tietze et al. 2011; Zamora et al. 2015). From this contradiction, we analyze the effect of anthropogenic aerosols on liquid-cloud microphysical properties. We describe the meteorological regimes associated with anthropogenic and biomass-burning pollution plumes and explain the differences between studies.

The second objective, presented in Chapter 6, described the impact of aerosols on the thermodynamic cloud-phase transition for different sets of cloud microphysical parameters, such as the liquid-cloud-droplet r_e, τ, and pressure levels. Since water-insoluble particles act as efficient ice nuclei (Popovitz-Biro et al. 1994), anthropogenic sulfate aerosols should inhibit the liquid-ice transition. Nevertheless, studies have shown that anthropogenic aerosols are potentially efficient IN (Lohmann and Feichter 2004). We study the

impact of anthropogenic aerosols on liquid-ice thermodynamic phase for different atmospheric parameter settings.

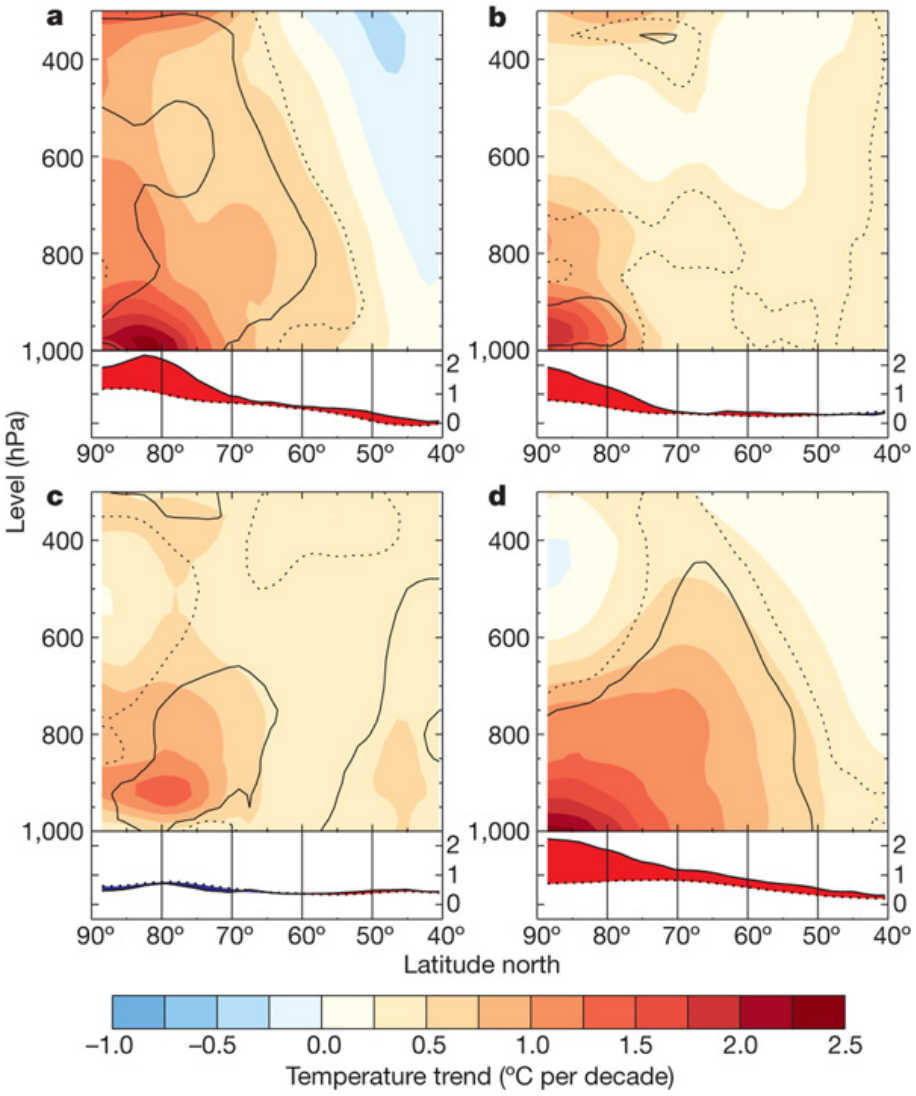

Figure 1.1: Zonal average of temperature trends for the four seasons. Zonal average of temperature trends for winter (December to February; a), spring (March to May; b), summer (June to August; c) and autumn (September to November; d). The black outlines indicate where trends differ significantly from zero at the 99% (solid lines) and 95% (dotted lines) confidence levels. The line graphs show trends (same units as in color plots) averaged over the lower part of the atmosphere (950-1,000 hPa; solid lines) and over the entire atmospheric column (300-1,000 hPa; dotted lines). Red shading indicates that the lower atmosphere has warmed faster than the atmospheric column as a whole. Blue shading indicates that the lower atmosphere has warmed slower than the atmospheric column as a whole (Screen and Simmonds 2010). Reprinted by permission from Macmillan Publishers Ltd: Nature (Screen and Simmonds (2010)), copyright 2010.

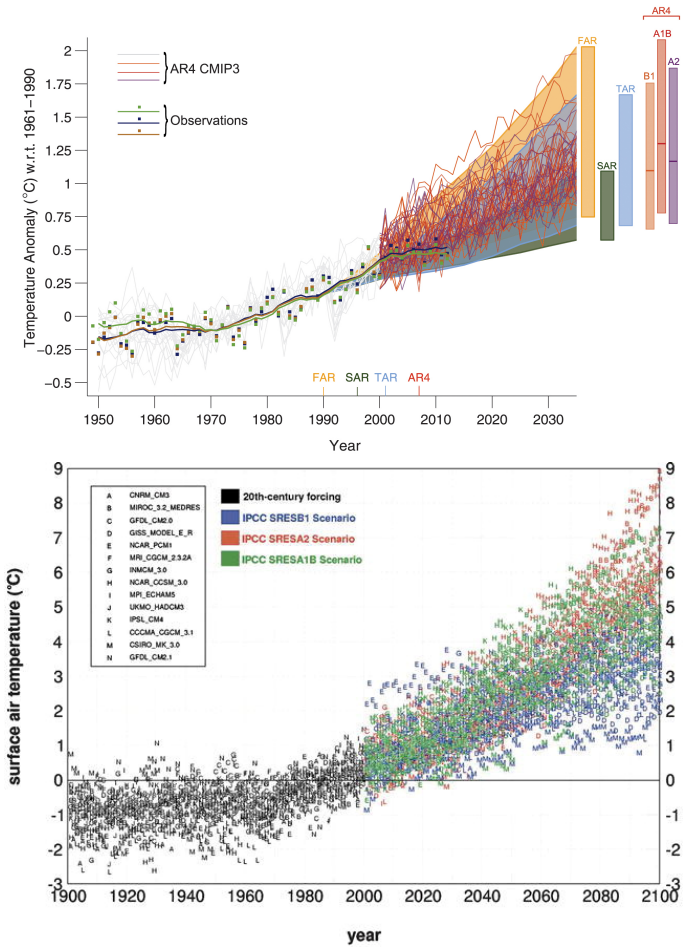

Figure 1.2: Evolution of temperature for the globe and the Arctic region for different scenarios. *Top:* Estimated changes in the observed globally and annually averaged surface temperature anomaly relative to 1961-1990 (in °C) since 1950 was compared with the range of projections from the previous IPCC assessments. Values are harmonized to start from the same value as in 1990. Observed global annual mean surface air temperature anomaly, relative to 1961-1990, is shown as squares and smoothed time series as solid lines (National Aeronautics and Space Administration (NASA) (dark blue), National Oceanic and Atmospheric Administration (NOAA) (warm mustard), and the UK Hadley Centre (bright green) reanalyses). The colored shading shows the projected range of the global annual mean surface air temperature change from 1990 to 2035 for models used in FAR, SAR, and TAR. TAR results are based on the simple climate model analyses presented and not on the individual full three-dimensional climate model simulations. For the AR4, results are presented as single model runs of the CMIP3 ensemble for the historical period from 1950 to 2000 (light grey lines) and for three scenarios (A2, A1B and B1) from 2001 to 2035. The bars at the right-hand side of the graph show the full range given for 2035 for each assessment report. (IPCC 2013). *Bottom:* Simulated and projected annual mean arctic surface air temperature, expressed as departures from 1981-2000 means, by 14 global climate models for the twentieth- and twenty-first centuries. Projections use three greenhouse gas forcing scenarios: IPCC SRESB1 (blue), IPCC SRESA1B (green), and IPCC SRESA2 (red) (Chapman and Walsh 2007a). ©American Meteorological Society. Used with permission.

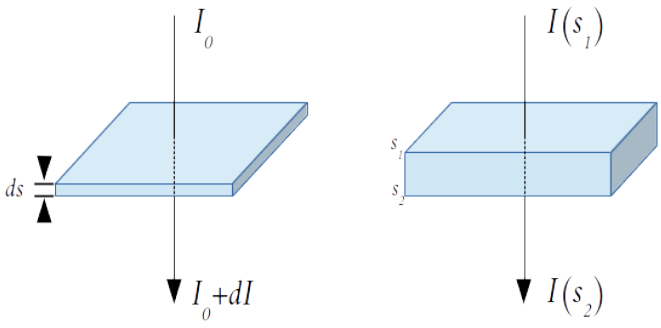

Figure 1.3: Incoming radiation interaction with a medium. *Left:* Incoming radiation with intensity I_0 goes through a layer with a thickness ds. The radiation exits the layer with a change in intensity of dI. *Right:* The layer is not infinitesimal, the incoming radiation with intensity $I(s_1)$ exits the layer with an intensity $I(s_2)$.

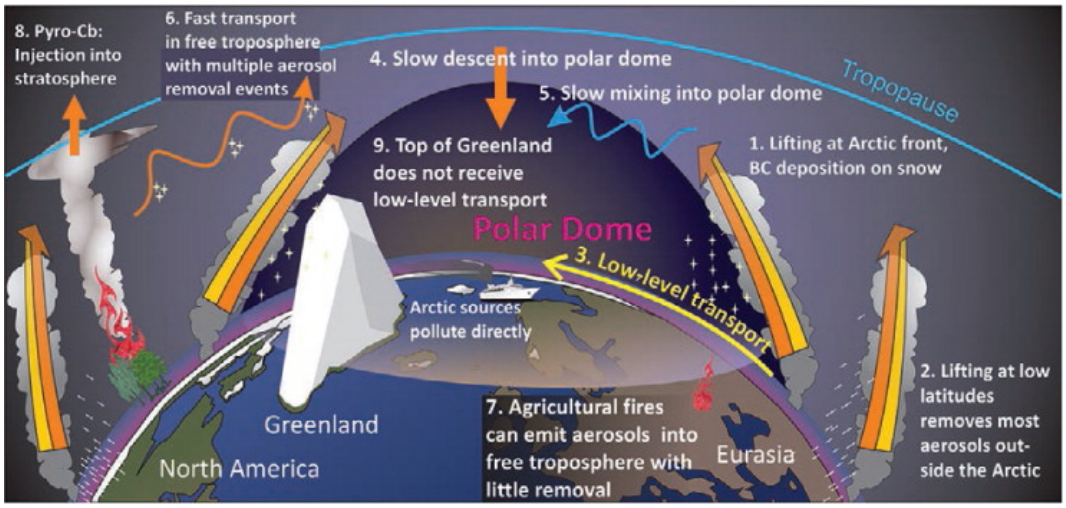

Figure 1.4: Schematic showing of pathways for the transport of air pollution into the Arctic. Following Stohl (2006), three main routes are evident: 1) low-level transport from midlatitude emission regions followed by uplift at the arctic front; 2) lifting of pollutants at lower latitudes, followed by upper tropospheric transport and possible slow descent (due to radiative cooling) or mixing into the polar dome — a frequent transport route from North America and Asia, but prone to significant wet scavenging; and 3) wintertime low-level transport of already cold air into the polar dome, mainly from northern Eurasia. Emissions from strong boreal fires could be lifted by pyroconvection (Fromm 2005) and later entrained into the polar dome (Law et al. 2014).

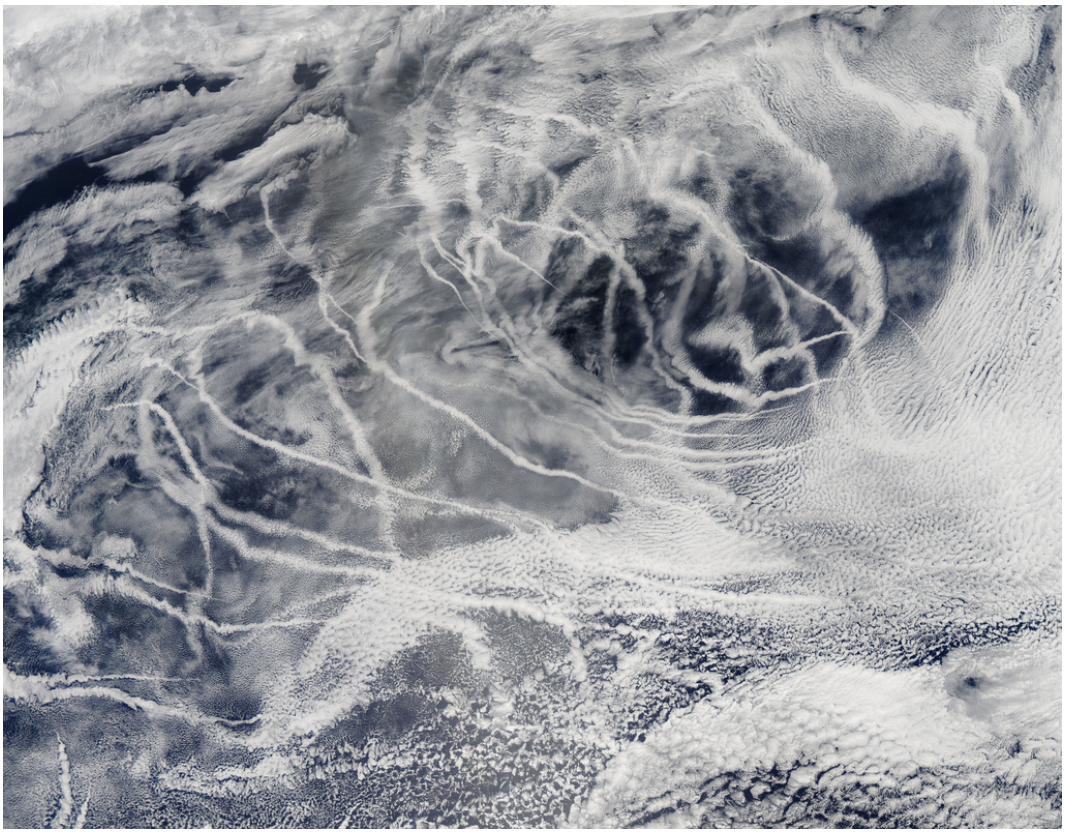

Figure 1.5: Satellite picture acquired on July 3, 2010 by MODIS (Moderate-Resolution Imaging Spectroradiometer) in the North Pacific (from NASA's Earth Observatory).

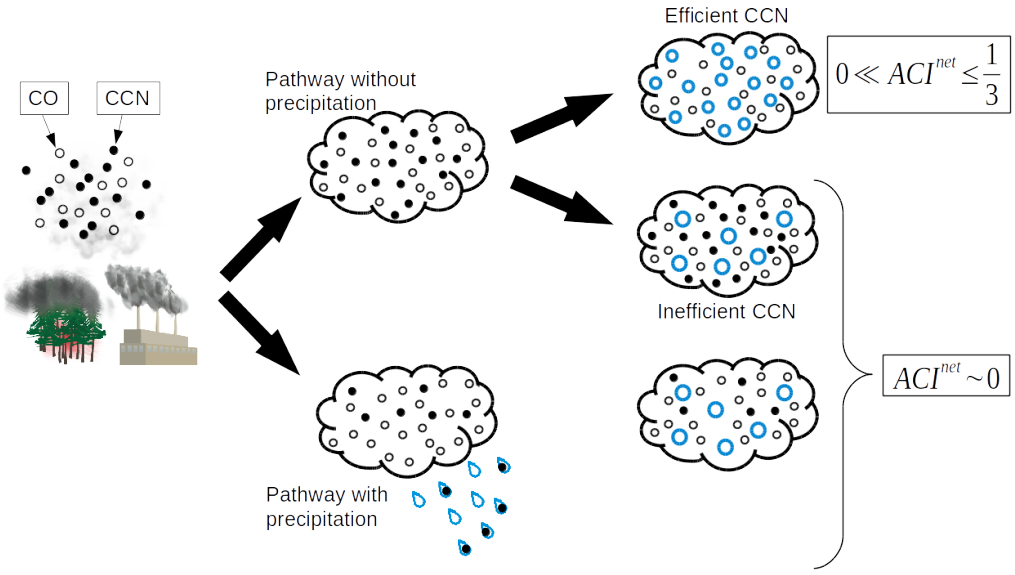

Figure 1.6: Relation between CO concentration and aerosol concentration along different pathways.

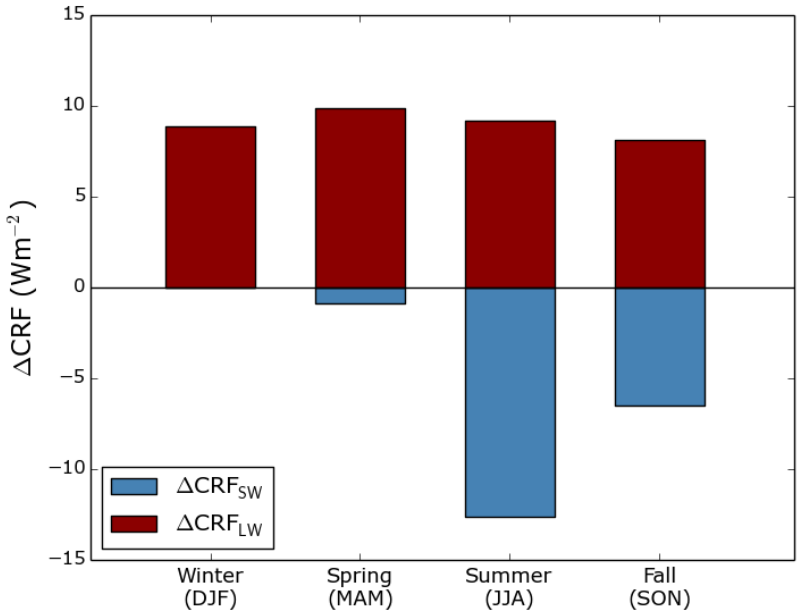

Figure 1.7: Seasonal mean change in arctic liquid-cloud shortwave radiative forcing (ΔCRF_{SW} in blue) and arctic liquid-cloud longwave radiative forcing (ΔCRF_{SW} in red) associated with haze pollution in Barrow (Alaska). Data are from Table 1 in Zhao and Garrett (2015).

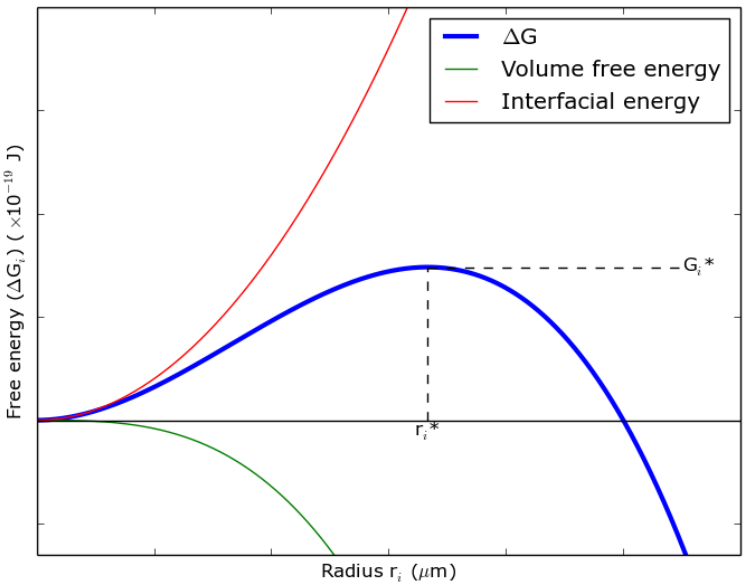

Figure 1.8: Free Gibbs energy (blue), volume free energy (green), and interfacial energy (red) of a germ of a cluster for homogeneous nucleation as function of the radius of the cluster.

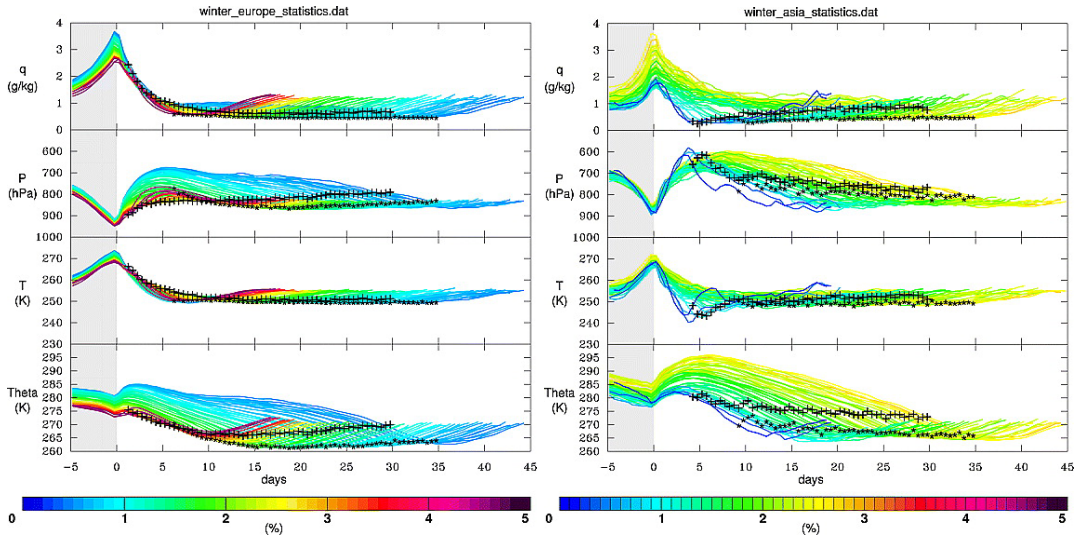

Figure 1.9: Meteorological parameter variations along trajectories from Europe and Asia. Left: Meteorological parameters (top plot, q; second plot, p; third plot, T; bottom plot, Q) along trajectories from the European box to the arctic lower troposphere. Every line represents an average over one of 60 transport time bins from half a day to 30 days, and its color shows the relative frequency of such cases. Days -5 to 0 (gray shaded) are the period before particles left the source region, the time when they entered the Arctic is marked with a plus, and 5 days later an asterisk is drawn. Right: Same as left panel, but for trajectories from the Asian box (Stohl 2006).

Table 1.1: Values from the literature quantifying the aerosol-cloud interaction using some variant of Eq. (1.25), are expressed here as ACI parameters. All values have been converted to the form, as in Eq. (1.25) for comparison purposes. All studies address low or liquid clouds

	method / instrument	Parameters used	ACI_τ	Parameter(s) controlled	region
Ground					
Feingold (2003b)	RS (Remote sensing)		0.10	LWP	Oklahoma (USA)
Garrett et al. (2004)	RS + in situ		0.15	LWP	Arctic
Kim et al. (2008)	RS + in situ		0.15	LWP, α^a	Kansas (USA)
Lihavainen et al. (2008)	in situ		0.24	LWP	Arctic
McComiskey et al. (2009)	RS + in situ		0.16	LWP, w^b	California
Sarna and Russchenberg (2016)	RS		0.01-0.1	LWP	Azores
Schmidt et al. (2014)	RS		0.18	LWP	Germany
Kim et al. (2012)	RS		0.17-0.36	LWP	USA
Airborne					
Twohy (2005)	in situ		0.27	no	NE^c Pacific Ocean
Raga and Jonas (1993)	in situ		0.09	no	British Isles; Azores
Martin et al. (1994)	in situ		0.25	no	SE^c California; S^c Atlantic; British Isles; Azores
Gultepe et al. (1996)	in situ		0.22	Tp.^{d}, w^b, LWC	Novia-Scotia (USA)
O'Dowd et al. (1999)	in situ		0.20	no	E^c Pacific; NE^c Atlantic
McFarquhar and Heymsfield (2001)	in situ		0.11	w^b, LWC	Indian Ocean
Ramanathan (2001)	in situ		0.21-0.33	no	global
Lu et al. (2007)	in situ		0.19	no	Houston (USA); NW Golf Mexico
Lu et al. (2008)	in situ		0.14	LWP	SW^c coast USA
Zamora et al. (2015)	in situ		0.05-0.16	LWP	Arctic
Painemal and Zuidema (2013b)	in situ		0.32	LWP	SE^c Pacific
Terai et al. (2012)	in situ		0.18	h^e	SE Pacific

Table 1.1: Continued

	method/ instrument	Parameters used	ACI_τ	L*	region
Satellite					
Nakajima et al. (2001)	AVHRR	N_d; N_a^f	0.17	no	global
Bulgin et al. (2008)	ASTER-2	r_e; τ_a^g	0.10-0.16	no	global
Kaufman et al. (2005)	MODIS	r_e; AI^h	0.046-0.174	no	Atlantic Ocean
Sekiguchi (2003)	AVHRR	r_e; N_a^f	0.1	no	global
Lebsock et al. (2008)	MODIS	r_e; AI^h	0.07	no	global
Sekiguchi (2003)	POLDER	r_e; N_a^f	0.07	no	global
Quaas (2004)	POLDER	r_e; AI^h	0.04(ocean)/0.012(land)	no	global
Quaas et al. (2005)	MODIS	N_d; τ_a^g	0.04	no	global
Costantino and Bréon (2013)	MODIS + CALIPSO	r_e, τ; AI^h	0.02 - 0.15	no	SE[c] Atlantic Ocean
Sporre et al. (2012)	MODIS + RS	r_e τ, N_d; N_a^f	0.17	no	Arctic
Satellite + Model					
Breon et al. (2002)	POLDER + back traj.	r_e; τ_a, AI^h	0.085(ocean)/0.04(land)	no	global
Chameides et al. (2002)	ISCCP + CTM	τ_c; τ_a^g	0.17(all)/0.14(low cloud)	no	E[c] Asia
Tietze et al. (2011)	PML2 + FLEXPART	τ, r_e; χ_{CO}^i	0.17	LWP , Tp.[d]	Arctic
Avey et al. (2007)	MODIS + FLEXPART	r_e, χ_{CO}	0.01-0.12	no	NE[c] USA

[a]: Adiabaticity; [b]: Updraft velocity; [c]: Acronyms N, S, E, W respectively stand for North, South, East, and West; [d]: Temperature; [e]: Cloud geometrical depth; [f]: Aerosol concentration; [g]: Aerosol optical depth; [h]: Aerosol index; [h]: Carbon monoxide concentration

CHAPTER 2

INSTRUMENTS, MODEL, REANALYSIS AND DATASET

Our study relies on the analysis of 3 different datasets in order to obtain independent information about cloud microphysical properties from satellite measurements, χ_{CO} from numerical tracer transport models, and meteorological parameters from reanalysis. In this chapter, we describe the different instruments and models that were used and how the datasets were combined.

2.1 Cloud parameters from satellite instruments

The Afternoon or "A-Train" satellite constellation is a group of six French and American satellites (Aura, PARASOL, CALIPSO, CloudSat, Aqua, and OCO-2) flying on a sun-synchronous orbit at a 705 km altitude and at 24,000 km per hour. All the platforms are flying only a few minutes apart from each other, as shown in Figure 2.1, and pass over the equator at 13:30 local time (Stephens et al. 2002). From this constellation we use data from POLDER-3 on PARASOL and MODIS on Aqua.

2.1.1 The POLDER/PARASOL Mission

POLDER-3 is a wide field of view imaging radiometer. The instrument was designed to provide the first global systematic measurements of multispectral, multidirectional solar radiations and polarizations reflected by the Earth/atmosphere system (Deschamps et al. 1994). The first two versions of the instrument, POLDER-1 and POLDER-2, flew respectively on JAXA/ADEOS-1 (Japan Aerospace Exploration Agency/Advanced Earth Observing Satellite) from November 1996 to June 1997 and on ADEOS-II from April 2003 to October 2003. POLDER-3 flew on PARASOL and was part of the A-train constellation from December 2004 to December 2013. On December 2009, PARASOL was removed from the A-Train to conform with regulations on atmospheric reentry.

The POLDER-3 camera on the PARASOL satellite platform (Polarization & Anisotropy of Reflectances for Atmospheric Sciences coupled with Observations from a Lidar) captures spectral, directional, and polarized measurements of reflected sunlight through a wide field of view (Fougnie et al. 2007). Multidirectional observations allow for a pixel to be observed from up to sixteen different view angles. The instrument measures radiance in 9 spectral channels between 443 and 1020 nm, including three polarized channels at 490, 670 and 865 nm. POLDER-3 cloud microphysical properties retrievals have a 36 km$\times$36 km spatial resolution. Cloud top pressure is derived from the cloud oxygen pressure (Bréon and Colzy 1999) (shown in Fig. 2.2).

2.1.2 MODIS

MODIS is a multispectral imaging radiometer developed by NASA on board EOS (Earth Observing System) Terra and Aqua satellites (King et al. 1992). The Aqua platform was launched in May 2002 on an orbit which later became the A-train orbit. Aqua is therefore sometimes considered the flagship of the A-train constellation. The instrument is particularly well suited to observe atmospheric properties but was designed to observe the atmosphere, land, and ocean and their interactions.

MODIS scans a wide swath of 2330 km centered on the satellite ground track. The MODIS instrument on board the Aqua satellite measures radiation in 36 different spectral bands with central wavelengths from 400 nm to 14 400 nm. For the effective radius, optical depth, and cloud top temperature we use Collection 5 Level-2 products (Platnick et al. 2003; King and Platnick 2006). Regarding the technique applied for computation of the MODIS Level-2 products, cloud top temperature is derived from the 11 μm infrared band. Cloud-droplet effective radius (r_e) and optical depth (τ) are retrieved from simultaneous cloud-reflectance measurements in three water absorbing bands (1.6, 2.1, 3.7 μm) and three nonabsorbing bands (0.65, 0.86, 1.2 μm) (Platnick et al. 2003). The characteristics for each band are provided in Table 2.1. The pixel resolution of the retrievals at nadir is 1 km$\times$1 km for cloud microphysics and 5 km$\times$5 km for cloud top temperature and pixel sized increase toward swath edges.

2.1.3 Parameters used in this study

To describe cloud radiative and microphysical properties we consider τ, r_e, cloud top temperature, and cloud top pressure from MODIS.

From POLDER, cloud top height is derived from the cloud oxygen pressure inferred from two spectral bands located in the oxygen A band (centered at 763 and 765 nm). Considering that the di-oxygen (O_2) absorption can be related to the penetration depth of radiation within the atmosphere, the oxygen transmittance from the top of the atmosphere to the cloud and back to space can be estimated. The cloud-top oxygen pressure can be inferred by comparing the value measured by POLDER to precomputed transmittance for varying cloud top pressure (Buriez et al. 1997). The advantages of using the cloud top pressure from POLDER is that it is less prone to systematic biases than MODIS cloud top pressure for low-level clouds, primarily because it is insensitive to temperature inversion (Tietze et al. 2011; Desmons et al. 2013) frequent in the Arctic (Kahl 1990; Solomon et al. 2011).

While POLDER is more accurate to estimate low-level cloud altitudes, MODIS is better at estimating high level cloud top pressure by measuring cloud brightness temperature. To avoid multilayer scenes, we do not consider pixels where 200 hPa separates MODIS and POLDER cloud top pressure. On the other hand, we consider POLDER cloud pressure when the pressure is higher than 800 hPa, MODIS cloud top pressure when the pressure is below 600 hPa, and a combination of both, weighted according to Figure 2.3, when cloud top pressure from MODIS and POLDER is between 600 hPa and 800 hPa.

To determine the cloud thermodynamic phase we use a combination of MODIS and POLDER-3 measurements. The algorithm takes advantage of multiangle polarization data, shortwave, thermal infrared, and visible measurements to retrieve a thermodynamic phase index Φ between 0 for liquid clouds and 200 for ice clouds with varying degrees of confidence (Riedi et al. 2010). Figure 2.4 shows the distribution of the thermodynamic phase index for clouds between 200 and 1000 m and between 1000 and 2000 m altitude from 2008 to 2010 over a region with latitudes greater than 65°. We observe different modes in the phase index corresponding to liquid clouds with Φ lower than 70, clouds with undetermined phase, mixed phase or multiple cloud layers, for which Φ lies between 70 and 140, and ice clouds with Φ greater than 140.

2.2 Passive tracer from numerical tracer transport models

In this study we colocate cloud parameters with CO concentrations from a numerical tracer transport model. CO, a passive tracer of aerosols, gives us an indication of the aerosol content. We used two different models: FLEXPART and GEOS-Chem.

2.2.1 CO as a passive tracer of aerosols

Carbon monoxide (CO) concentrations are correlated with aerosol concentrations from combustion (Longley et al. 2005; Lathem et al. 2013). However, while aerosols undergo wet and dry scavenging during transport, CO remains in the atmosphere. Garrett and Zhao (2006) used aircraft measurements in the Arctic and showed that if CO and CCN are uncorrelated, it is due to the precipitation processes. CO sink is the oxidization by reaction with the hydroxyl radical (OH) (Dimitriades and Whisman 1971), which itself is produced by photolysis of ozone. The photolysis mechanisms are tied to solar insolation, and so there is a strong seasonal cycle in CO. The lifetime of CO is months and is maximum during winter. In summer, the CO lifetime is about two weeks (Stohl 2006), this is why considering the CO as passive and inert is a good approximation to the real CO. In the numerical tracer transport model used in this study, the CO does not experience any sink process but is removed from simulation 31 days or 2 months after emission, depending on the considered model.

Longley et al. (2005) measured CO and aerosol concentration in Manchester and found a correlation coefficient of 0.78 when aerosol size is greater than 95 nm. Edwards et al. (2004) calculated the correlation between CO column and aerosol optical depth of 0.74.

CO can only be used to trace aerosols from combustion process, such as biomass-burning or fossil-fuel. From other sources, such as desert or marine origins, CO is not a by-product and, therefore, cannot be used as a passive tracer.

2.2.2 FLEXPART

For determining anthropogenic pollution tracer fields, we use the Lagrangian particle dispersion model FLEXPART (Stohl et al. 1998, 2005). The model is driven with 3 hourly operational analysis wind fields from the European Centre for Medium-Range Weather Forecasts (ECMWF) with 91 model levels and a horizontal resolution of $1^\circ \times 1^\circ$. We use

the same simulations as described by Stohl et al. (2013), which consider a black-carbon tracer undergoing removal processes, two fixed-lifetime black carbon tracers, and a carbon monoxide tracer. The CO tracer used for this study is considered passive in the atmosphere but is removed from the simulation 31 days after emission, thus focusing the simulation on "fresh" pollution. Any other sink is considered by the tracer transport numerical model. For the CO emissions, ECLIPSE (Evaluating the CLimate and air quality ImPacts of Short-lived pollutants) version 4.0 emission data (Stohl et al. 2015) are used. For the anthropogenic emissions considered here, the ECLIPSE emissions are based on the GAINS (Greenhouse gas – Air pollution Interactions and Synergies) model (Amann et al. 2011). The emissions are determined separately for every year of this study and, notably, include gas flaring emissions, which have been shown to be important for black carbon in the Arctic (Stohl et al. 2013). Emissions from the residential sector are temporally disaggregated using a heating degree day approach (Stohl et al. 2013). Only CO from combustion sources is considered, so other CO contributions from volatile organic compounds are not considered (Stohl et al. 2003).

Studies that have used FLEXPART CO concentration fields (χ_{CO}) have found satisfactory agreement between model output and measurements (Stohl 2006; Paris et al. 2009; Hirdman et al. 2010; Sodemann et al. 2011; Stohl et al. 2013, 2015; Eckhardt et al. 2015). In the Alaskan Arctic for the day of 18 April 2008, Warneke et al. (2009) described a slope of 0.9 for a linear fit between FLEXPART model output of χ_{CO} and airborne measurements of CO with a least-squares correlation coefficient of 0.63.

The FLEXPART model outputs used here have a temporal resolution of 3 h and a spatial resolution of $1^\circ \times 2^\circ$ (in latitude and longitude) divided into 9 different vertical levels. FLEXPART CO concentration (χ_{CO}) output is provided in units of $\mathrm{mg\,m^{-3}}$ but converted to units of ppbv (parts per billion by volume) to remove the atmospheric pressure dependence.

2.2.3 GEOS-Chem

We initially started to study aerosol-cloud interactions by using the numerical tracer transport model FLEXPART, but we changed to GEOS-Chem, when considering biomass-burning plumes, to extend the analysis time period from 3 to 6 years. χ_{CO} from GEOS-

Chem v9-0-03 is used as a passive tracer of aerosols from biomass-burning and fossil-fuel (Bey et al. 2001; Parrington et al. 2012). GEOS-Chem is a global 3-dimensional model of tropospheric chemistry driven by assimilated meteorological observations from the NASA Goddard Earth Observing System version 5 (GEOS-5). The model uses dynamic fields, such as advection from wind vector and surface pressure, convection from wet convective mass flux and detrainment, and boundary layer mixing from the mixed layer depth, which are referenced in Bey et al. (2001) to trace CO pathways from sources to the Arctic.

The model is run at a spatial resolution of 2° in latitude and 2.5° (a degradation of the native resolution of $0.5^\circ \times 0.667^\circ$) in longitude at 47 native vertical levels to track concentrations of pollution downwind of source regions. The only chemical sink for CO in GEOS-Chem is OH, and a lifetime of 2 months is considered. The model is extensively described in (Parrington et al. 2012). The horizontal and vertical structure of model CO in the lower troposphere compares favorably with CO measured in field campaigns (Fisher et al. 2010; Finch et al. 2014; Bey et al. 2001). For example, a statistical comparison of modeled and observed CO from the field campaign BORTAS-B showed a difference between the median of modeled CO and observed CO of -0.1 ppb (Finch et al. 2014). A vertical analysis from the same study showed that modeled and measured CO below 4 km correlate with a Spearmans rank correlation r_s = 0.65. We vertically and horizontally colocate χ_{CO} distributions with low-level liquid cloud microphysical properties and T_C obtained using the MODIS (MODerate-resolution Imaging Spectroradiometer) and POLDER-3 (POLarization and Directionality of the Earth's Reflectance) sensors (Platnick et al. 2003) for a period between March and September from 2005 to 2010.

The model considers 3 CO sources: i) fossil-fuel emissions from the Emission Database for Global Atmospheric Research (EDGAR), the European Monitoring and Evaluation Programme (EMEP), the Big Bend Regional Aerosol and Visibility Observationa (BRAVO), and STREETS, ii) biomass-burning emissions from the Global Fire Emission Data Set (GFED-3), and iii) biogenic emissions from the Model of Emissions of Gases and Aerosol from Nature (MEGAN) dataset. The model characterizes source regions of CO, but also the origin of a time dependent background of χ_{CO}: There are 5 fossil fuel CO source regions outlined in red in Figure 2.5: Northwest America, Northeast America, Europe, East Asia, and the rest of the world; 10 biomass burning CO source regions outlined in green in Fig-

ure 2.5: Northwest North America, Northeast North America, Southwest North America, Southeast North America, Europe, West Siberia, Mid Siberia, East Siberia, East Asia, and the rest of the world; CO generated by volatile organic compounds from methane, biofuel, isoprene, monoterpenes, methanol, and acetone.

We compare the CO from tracer and background concentration of GEOS-Chem with total CO measurements from 5 different ground-based stations within the arctic circle from the NOAA ESRL Carbon Cycle Cooperative Global Air Sampling Network (Novelli and Masarie 2014). The different stations are displayed in Figure 2.6 and consist of daily in situ flask measurement sites. Table 2.2 lists latitudes, longitudes, and altitudes of the different stations and the associated vertical bin from the numerical tracer transport model.

We temporally, horizontally, and vertically colocate GEOS-Chem χ_{CO} with CO flask measurements. Figure 2.7 shows the linear regression of modeled CO versus measured CO for all stations with the associated correlation coefficients. Table 2.3 lists the slope, the correlation coefficient, the standard deviation of the linear regression between modeled and measured CO concentration, the number of flask measurements, and the median of the difference between modeled and measured-CO-concentration distribution for the five arctic stations from the NOAA ESRL network. The slope of the linear regression of modeled CO as a function of the ground-based measurements of each station is between 0.6 and 0.8. While the modeled χ_{CO} is underestimated by up to -6.2 ppb on average at Summit, probably due to spatial and temporal averaging, the variations are similar with a correlation coefficient greater than 0.7. Figure 2.8 shows the time series of the measured CO for each station with the associated modeled CO from Geos-Chem. Considering spring 2006 in Barrow, several χ_{CO} retrieved by the model are underestimated compared to flask measurements during winter 2006 of about 60 ppb, however, variations are well represented by the model with a coefficient correlation with flask observations, for all the stations, of 0.77.

In a larger context, Monks et al. (2015) used the POLar study using Aircraft, Remote Sensing, surface measurements and models of Climate, chemistry, Aerosols, and Transport (POLARCAT) Model Inter-comparison Project (POLMIP), which regroups 11 atmospheric models with chemistry including GEOS-Chem, to evaluate the simulations of CO concentration in the Arctic. Their study concluded that GEOS-Chem shows better agreement

with the observations in winter and spring than other models but during summertime at the surface GEOS-Chem overestimates CO in the lower troposphere. A reason for the better agreement is a scheme for transition metal-catalysed loss of HO_2 on aerosol that produces water instead of H_2O_2 which increases CO lifetime (Mao et al. 2010). However, a comparison of modeled CO from GEOS-Chem with measurements from aircraft during Arctic Research of the Composition of the Troposphere from Aircraft and Satellites -A (ARCTAS-A) (in April 2008) and ARCTAS-B (in June-July 2008) shows correlation coefficients of respectively 0.99 and 0.80 (Monks et al. 2015).

2.3 Meteorological parameters from ERA-Interim datasets

ERA-Interim (ERA-I) reanalysis data from ECMWF (Berrisford et al. 2011) extends from 1989 to the present with an improved version released in 2011 (Dee et al. 2011). ERA-I reanalysis provides atmospheric properties retrievals by generating dynamical atmospheric datasets associated with successive short-term model forecasts constrained by observations. The reanalysis can be decomposed into 3 main parts: the model, the data assimilation method, and the observations. Here, we briefly introduce these three components of ERA-I.

The data assimilation uses 12 hourly analysis cycles. Observations of temperature, wind, humidity, ozone, surface pressure, 2 m temperature, 2 m humidity, soil moisture, soil temperature, snow, and ocean waves are compared to previous information from a forecast model to evaluate the evolution of the atmospheric state. The analyses initialize the model forecast for the next analysis cycle and so on. The efficiency of the model is observed through the required adjustments between the model results and the observations. Other parameters, such as precipitation or radiation fields, can then be obtained using model physics, such as precipitation or radiation fields. The number of assimilated observations in ERA-I is approximately 10^7 per day.

The temporal resolution is 6 h for 60 pressure levels. Reanalysis data from ERA-I shows good agreement with satellite retrievals and aircraft data for cloud fraction and cloud radiative forcing in the Arctic (Zygmuntowska et al. 2012). Wesslén et al. (2014) analyzed ERA-I data with the Arctic Cloud-Ocean Study (ASCOS) campaign measurements in 2008 and calculated biases of about 1.3 °C, 1 %, -1.5 hPa, and -0.4 $\mathrm{m\,s^{-1}}$, respectively, for tem-

perature, relative humidity, surface pressure, and wind speed, root mean square errors of about 1.9 °C, 3.7 %, 8.7 hPa, and 1.6 m s^{-1}, respectively, and correlation coefficients of approximately 0.85 for temperature and surface pressure, 0.31 for the relative humidity, and 0.98 for the wind speed.

The goal of this study is to use satellite, tracer transport models, and meteorological data sets to determine the effects of long-range aerosol transport on cloud microphysics due only to the pollution itself and not to the meteorological state. A particular focus is on temperature, SH, and LTS since these have been identified as a basic meteorological quantities that correlate with cloud microphysical properties (Matsui et al. 2006; Mauger and Norris 2007). LTS is derived from the potential temperature. Defining the potential temperature (θ) as

$$\theta = T \cdot \left(\frac{P_0}{P}\right)^{\frac{R}{c_p}}, \tag{2.1}$$

where T and P are the air temperature and pressure, P_0 equals 1000 hPa, and R and c_p are, respectively, the gas constant for air and the isobaric heat capacity, the LTS is defined as the potential temperature difference between 700 and 1000 hPa (Klein and Hartmann 1993).

$$\text{LTS} = \theta_{700} - \theta_{1000} \tag{2.2}$$

2.4 Colocation of multiple datasets

Level-2 dataset from MODIS is stored in granule, covering 5 minutes of data acquisition, at either 1 or 5 km pixel spatial resolution. POLDER-3 cloud products are provided in native pixel resolution that corresponds to 6 km×6 km. The PM dataset (POLDER-MODIS), used for comparisons between POLDER and MODIS is a merged dataset from the Level 2 official products of each instrument. For each POLDER orbit the associated MODIS granule is colocated. MODIS products are averaged within each 6 km×6 km super-pixel.

POLDER-MODIS, GEOS-Chem, FLEXPART, and ERA-I have a different spatial and temporal resolution. To colocate the different retrieved properties, we averaged the different datasets over time and space. We consider an example with FLEXPART spatial and temporal resolutions, but we use the same method with GEOS-Chem. CO tracer concentrations from a FLEXPART grid cell are defined as the average between two temporal points, averaged over a spatial box. For example, model CO concentrations at 03:00 UTC and at the latitude–longitude coordinates of (70°, 80°), represent an average over a box between

the latitudes of 70 to 71° and longitudes of 80 to 82° and between 00:00 UTC and 03:00 UTC. For an A-train satellite overpass time of 00:45 UTC, we match space-based retrievals to FLEXPART concentration output at 03:00 UTC representing the average concentration between 00:00 UTC to 03:00 UTC and then linearly interpolate ECMWF meteorological fields to the LTS and SH values for 01:30 UTC.

Regarding horizontal colocation, Figure 2.9 shows how the datasets are combined. We project data from satellite, model, and reanalysis datasets onto an equal-area sinusoidal grid such that the grid-cell resolution is $0.5^\circ \times 0.5^\circ$ at the equator corresponding to an area of 54 km $\times$ 54 km. The sinusoidal projection conserves the grid-cell area independently of longitude and latitude. One grid-cell can include up to 81 POLDER-MODIS pixels. Satellite and tracer transport model data are averaged over each grid-cell.

It has been argued that aerosol impacts on clouds may be artificially low where it is measured at low spatial resolution (McComiskey and Feingold 2012). In fact, aerosols impact cloud properties at the microscopic scale but the aggregation of data to a 54 km $\times$ 54 km spatial resolution causes biases which smooth the effect of aerosols.

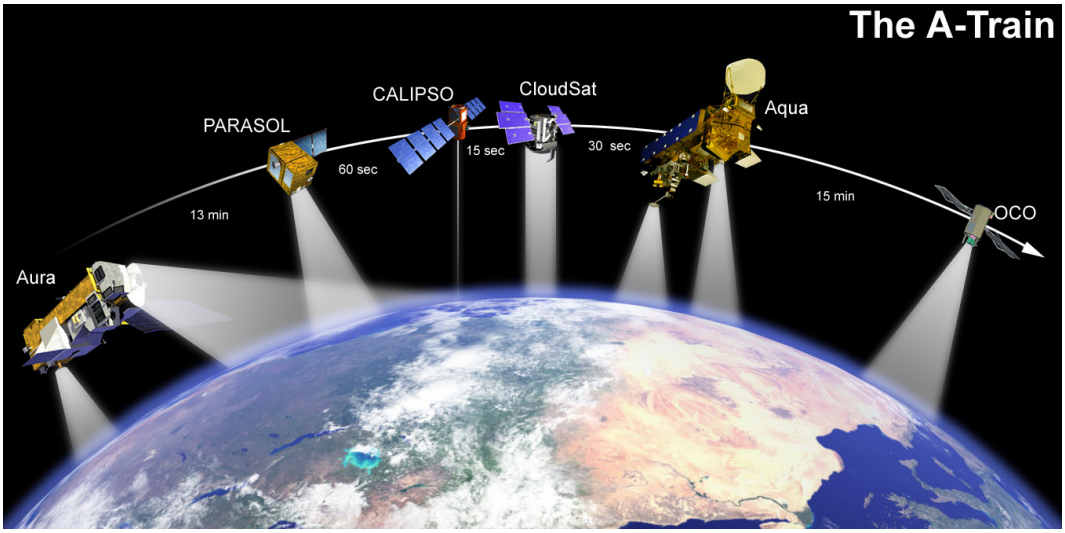

Figure 2.1: The A-train constellation. As of December 2013, PARASOL stopped recording data and OCO failed during the launch, but OCO-2 is now in orbit (NASA's Earth Observatory).

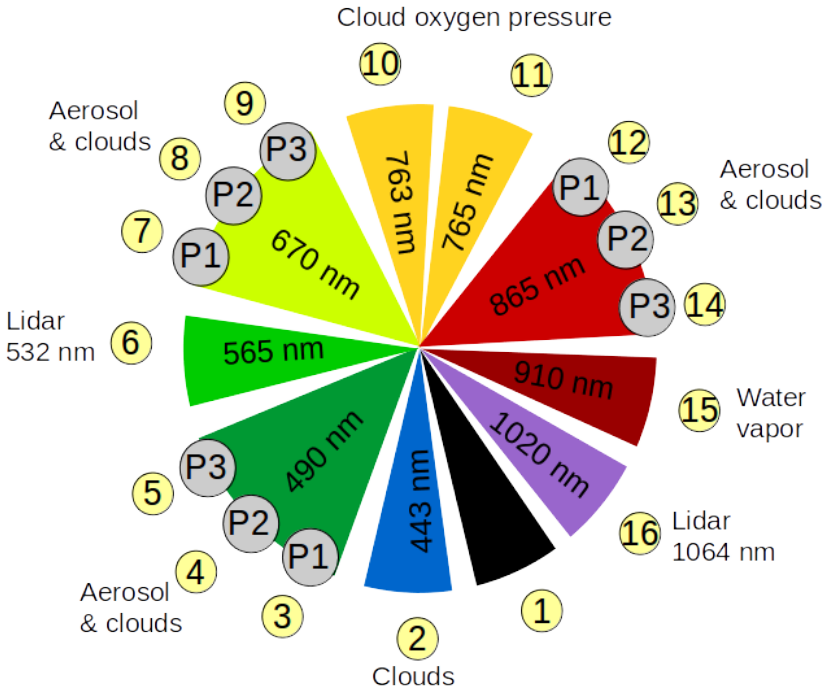

Figure 2.2: The different spectral channels of POLDER-3. P1 (+60°), P2(0°), and P3 (-60°) represent the 3 polarized directions of the filters (CNES).

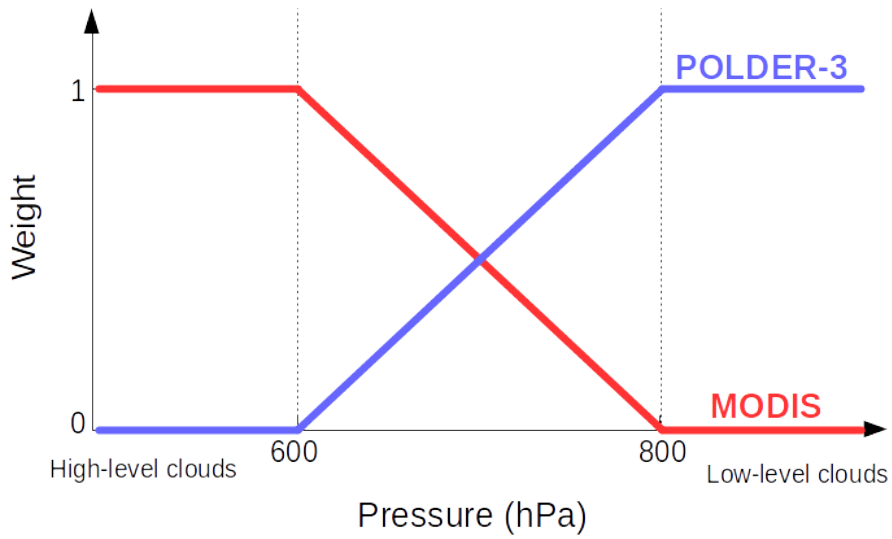

Figure 2.3: Weight attributed to POLDER and MODIS cloud top pressure when the cloud-top-pressure measurements are between 600 and 800 hPa.

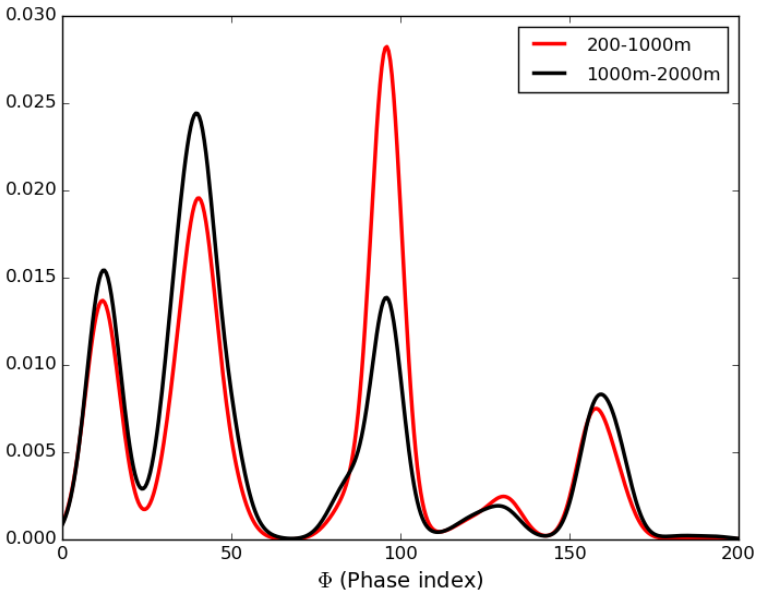

Figure 2.4: Normalized cloud thermodynamic phase index frequency distribution from the POLDER-MODIS algorithm, for pixels with the phase-index SD less than 10. Colors represent different cloud altitudes, between 200–1000 m in red and between 1000–2000 m in black.

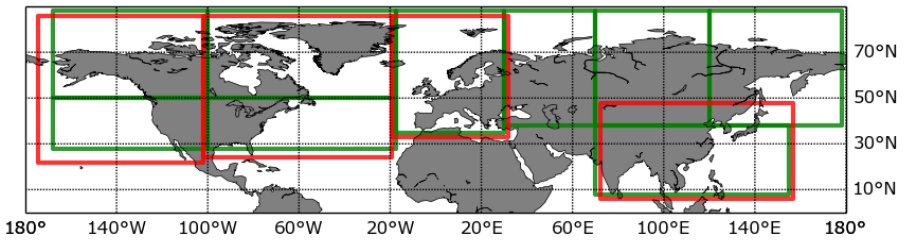

Figure 2.5: Source regions for the tagged CO simulation. Regions outlined in red denote fossil fuel tagged tracers; regions outlined in green refer to biomass-burning tagged tracers.

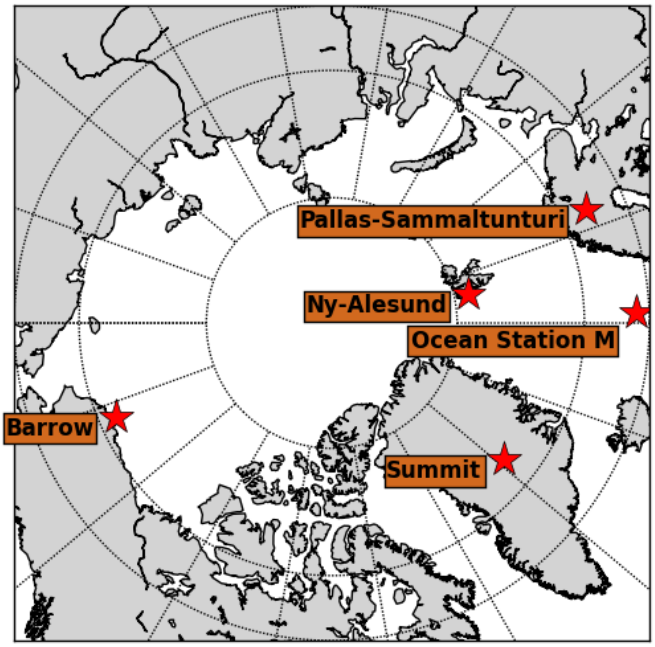

Figure 2.6: Stations from the NOAA ESRL network, from which the CO-concentration flask measurements are compared with modeled CO.

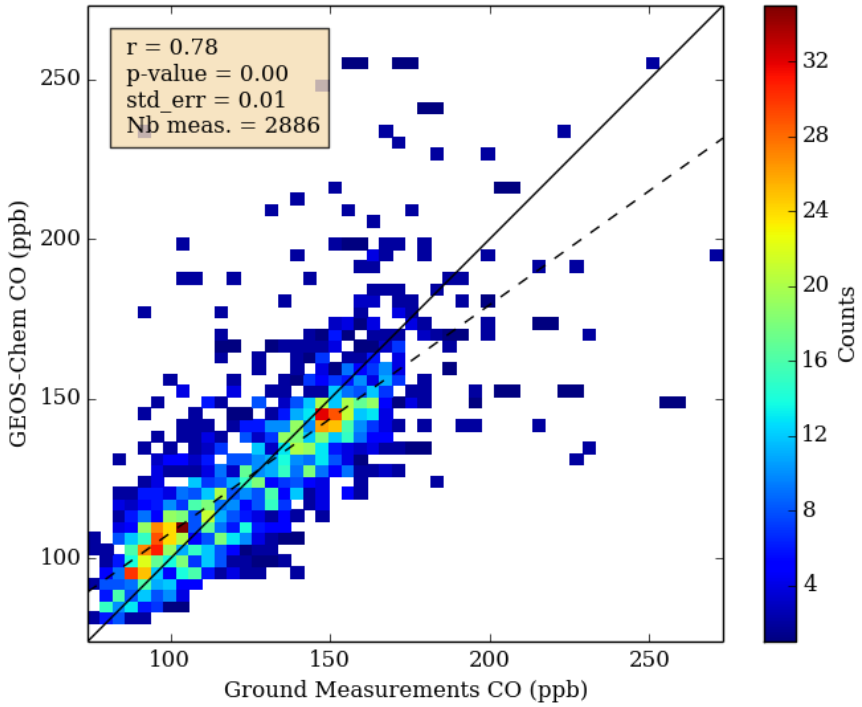

Figure 2.7: 2D distribution and linear regression of GEOS-Chem total CO concentration as function of CO-concentration observation from flask measurement from 5 different arctic stations between 2005 and 2010. Value of correlation coefficient (r), the p-value, the standard error, and the number of measurements are shown.

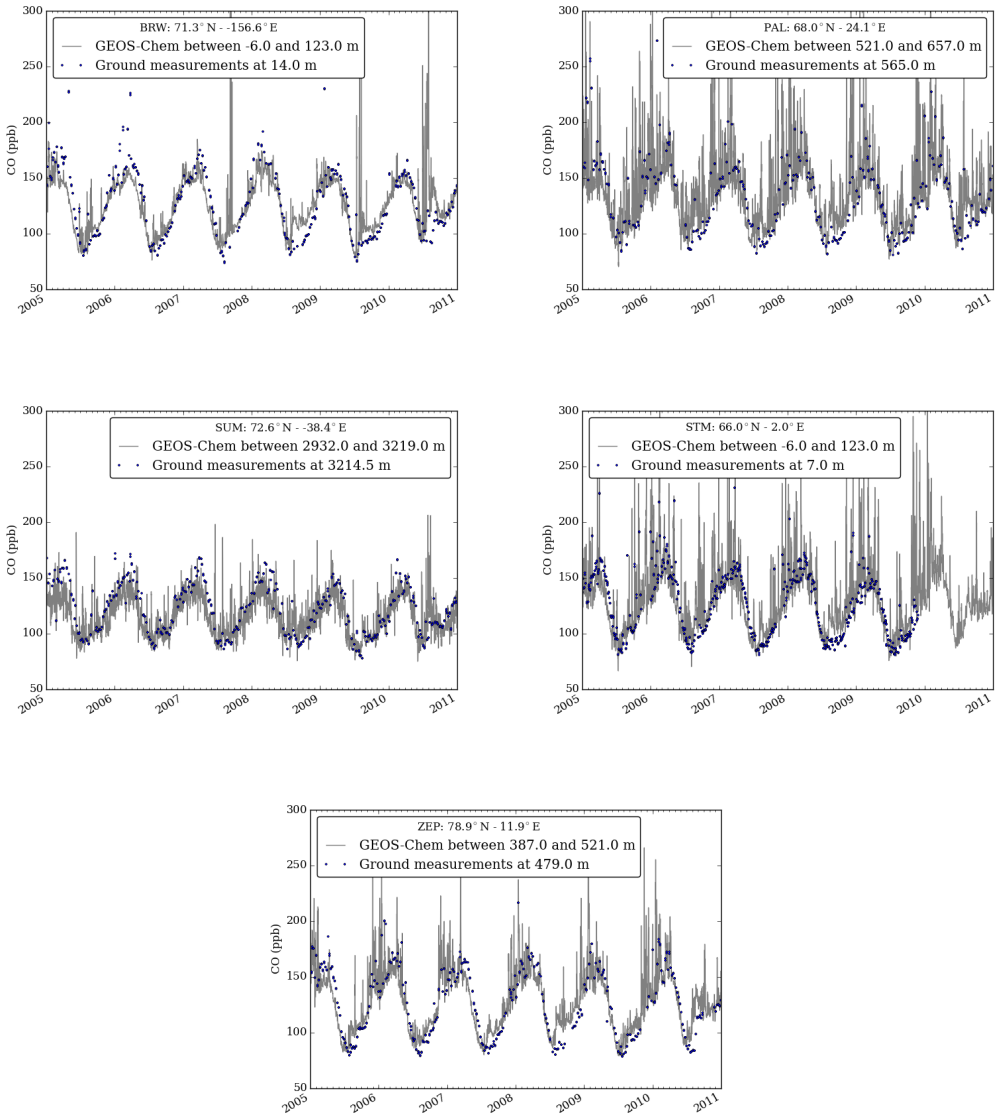

Figure 2.8: Time series of total CO concentration between 2005 and 2010 from GEOS-Chem (gray lines) with the associated total CO-concentration flask measurements (blue points) from NOAA ESRL from 5 arctic stations.

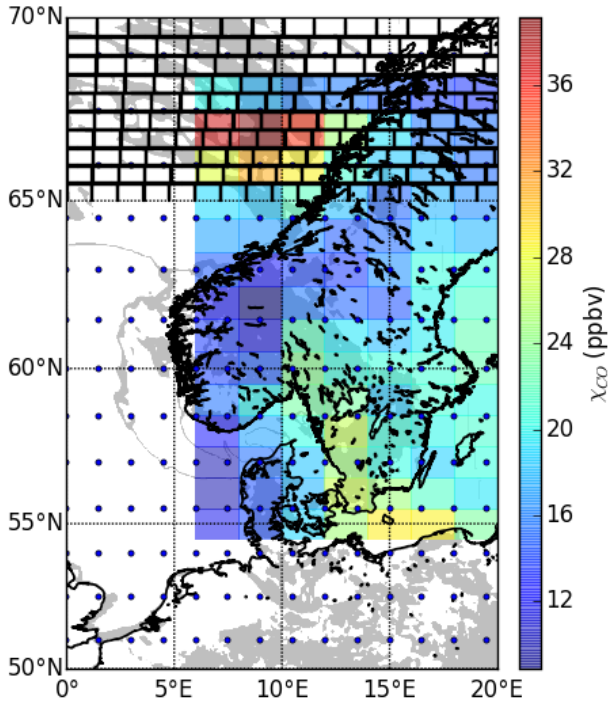

Figure 2.9: Illustration of the horizontal colocation method, showing satellite data corresponding to cloud top pressures below 1000 m altitude (gray shading), the average FLEXPART CO concentration between 1 and 2 km (colored shading), and the spatial resolution of temperature profiles and SH in blue points. The black grid, at the top of the map, corresponds to the sinusoidal equal-area grid used in this study for colocating each data set.

Table 2.1: Characteristics of spectral bands selected for the MODIS instrument aboard AQUA (Ackerman et al. 1998).

Band	Wavelength (nm)	Resolution (m)	Commentary
1	620-670	250	land/cloud/aerosol boundaries
2	841-876	250	
3	459-479	500	
4	545-565	500	
5	1230-1250	500	land/cloud/aerosol properties
6	1628-1652	500	
7	2105-2155	500	
8	405-420	1000	
9	438-448	1000	
10	483-493	1000	ocean color/
11	526-536	1000	phytoplankton/
12	546-556	1000	biogeochemistry
13	662-672	1000	
14	673-683	1000	
15	743-753	1000	
16	862-877	1000	
17	890-920	1000	
18	931-941	1000	atmospheric water vapor
19	915-965	1000	
20	3,660-3,840	1000	
21	3,929-3,989	1000	surface/cloud
22	3,929-3,989	1000	temperature
23	4,020-4,080	1000	
24	4,433-4,498	1000	
25	4,482-4,549	1000	
26	1,360-1,390	1000	
27	6,535-6,895	1000	cirrus cloud/ Water vapor
28	7,175-7,475	1000	
29	8,400-8,700	1000	cloud properties
30	9,580-9,880	1000	ozone
31	10,780-11,280	1000	surface/cloud
32	11,770-12,270	1000	temperature
33	13,185-13,485	1000	
34	13,485-13,785	1000	cloud top
35	13,785-14,085	1000	altitude
36	14,085-14,385	1000	

Table 2.2: Description of the 5 different stations, from NOAA ESRL, considered to compare χ_{CO} from GEOS-Chem and χ_{CO} from in situ samples. Latitudes, longitudes, altitudes of the stations are shown with the associated GEOS-Chem vertical box.

Station	latitude (°N)	longitude (°E)	altitude (m)	Geos-Chem vertical bin [min, max] (m)
Barrow	71.3	- 156.6	14.0	[-6.0, 123.0]
Ny-Alesund	78.9	11.9	479.0	[387.0, 521.0]
Pallas	68.0	24.1	565.0	[521.0, 657]
Ocean Station M	66.0	2.0	7	[-6, 123.0]
Summit	72.6	-38.4	3214.5	[2932.0, 3219.0]

Table 2.3: Results of the linear regression of total CO concentration from GEOS-Chem as function of the total CO concentration from in situ flask for five different arctic stations. From the linear fit the slope (α), the correlation coefficient (r), standard deviation (σ), the number of measurements, and the median of the difference between the two sets are shown.

Station	α	r	σ	Nb meas.	Model-Obs med. (ppb)
Barrow	0.6	0.70	0.02	554	-1.4
Ny-Alesund	0.8	0.86	0.02	569	2.5
Pallas	0.7	0.77	0.02	559	3.02
Ocean Station M	0.74	0.68	0.02	919	2.7
Summit	0.6	0.75	0.02	605	-6.2

CHAPTER 3

TEMPORAL AND GEOGRAPHICAL VARIABILITY OF PARAMETERS

We first analyze POLDER, MODIS, GEOS-Chem, FLEXPART, and ERA-I datasets separately to understand the seasonal and geographical variations of the different parameters examined in our study. The arctic region is peculiar in many aspects: the sea ice, the polar night, the absence of major local pollution sources, and the low topography surrounded by high mountains in Alaska and Greenland.

We discuss in this chapter four different topics: (i) the monthly variation of sea-ice extent, (ii) liquid and ice-cloud properties over the Arctic, (iii) χ_{CO}, a passive tracer of aerosols, from GEOS-Chem, and finally (iv) the variability of the specific humidity (SH) and the lower tropospheric stability (LTS) of the arctic atmosphere.

In this section we are not describing multiyear trends of the data to deduce a general increase or decrease of any parameter with time. Apart from cloud-top pressure distributions, results are shown only for low-level clouds with cloud-top pressure greater than 700 hPa.

3.1 Cloud properties

During the arctic night, the passive satellite instruments POLDER-3 and MODIS take no measurements in the visible channels and do not retrieve cloud optical properties. The instruments record data from March to October at latitudes greater than 65°, but during March and October the solar angle is too low for the instruments to retrieve good quality data so we did not consider these months here either. Also, at latitudes greater than 85° the problem of low solar angle remains and causes high uncertainties in cloud property retrievals from passive optical sensors. Therefore, we keep high latitude points above 85° for illustration purposes only but do not consider them in the analysis.

3.1.1 Cloud Phase

Figures 3.1 and 3.2 illustrate, respectively, the monthly liquid-cloud fraction and ice-cloud fraction of low-level clouds in the Arctic.

Regarding the liquid-cloud fraction, we notice that it reaches a maximum during August with a cloud fraction of 0.8, and more generally during summertime (June, July, and August). Moreover, the fraction is higher above the open ocean (0.85) than above land or sea ice (0.6). The Norwegian Sea, the Barents Sea, and the Atlantic Ocean have a liquid-cloud fraction that is especially high (0.85) through the year compared to other regions (0.65).

Mioche et al. (2014) observed similar results for mixed-phase clouds with the active sensor CALIOP, as shown by Figure 3.3. They observed a maximum of cloud fraction above the Atlantic Ocean and Norwegian Sea with a mixed-phase cloud fraction of 0.55 compare to the fraction of 40 elsewhere. The similarities between mixed-phase-cloud fraction from CALIOP and liquid-cloud fraction from POLDER suggest that the POLDER-MODIS algorithm primarily considers mixed-phase clouds as liquid clouds.

Figure 3.2 shows the ice-cloud fraction of low-level clouds. We first notice that the ice-cloud fraction, 0.25, is lower than the liquid-cloud fraction, 0.65. Unlike the liquid-cloud fraction, the ice-cloud fraction is higher in April (0.55) than in summer (0.25) due to lower temperatures during spring, thus favoring the ice-cloud formation.

3.1.2 Liquid cloud optical depth

Figure 3.4 shows the monthly average of τ for liquid clouds from April to September over the arctic region. τ over the European region does not vary and stays around 15 for the different months. Regions close to eastern Siberia and America have their lowest cloud-optical-depth values in July, with an optical depth of 5, whereas in April, τ is as high as 16.

3.1.3 Liquid cloud droplet effective radius

Figure 3.5 shows mean values of the liquid-cloud-droplet r_e from March to September retrieved by MODIS. Lower values appear related to sea-ice presence (c.f. the Appendix). Open ocean is associated with an average effective radius of 15 μm, whereas sea-ice surface is associated with an average effective radius of 11 μm. In addition to the 2.1 μm channel,

the MODIS algorithm uses a 1.2 μm channel over sea ice and a 0.865 μm channel over open ocean. Thus, the difference in r_e between the two surfaces of approximately 4 μm may be an artifact caused by the surface dependent channel used in retrieval. It should be noted that POLDER retrievals of liquid-cloud-droplet r_e, based on a polarization technique that is insensitive to surface properties, do not exhibit a discontinuity between open ocean and sea ice (not shown here). The overall conclusions described in this dissertation remain identical whether we are using MODIS r_e or POLDER r_e. We note that τ in Figure 3.4 is not obviously different over sea ice versus open ocean.

Larger values of r_e are observed above the open ocean (16 μm) than above land (12.5 μm), and the smallest values are retrieved above the sea ice (11 μm) (c.f. the Appendix). The difference between land and ocean can be due to physical considerations. The lower values of the effective radius over land compared to ocean have been observed in a global study by Breon et al. (2002), using POLDER, and explained by the presence of aerosols. The difference in humidity suggested by Wang et al. (2014) can explain that over arctic land and sea ice, where humidity is lower, smaller droplets are observed than over ocean.

3.1.4 Uncertainty on liquid cloud droplet effective radius

Figure 3.6 shows the uncertainty associated with the effective radius of liquid cloud droplets retrieved by MODIS over the Arctic region for a layer between 700 and 1,013 hPa. The larger effective radius uncertainty (average 56%) was retrieved over the sea-ice surface in July whereas the uncertainty above the open ocean was 14% on average for the same month.

The increase of uncertainty is due to the use of a different channel to retrieve cloud microphysical properties according to the surface albedo. Over sea ice, the MODIS algorithm uses longer wavelengths than the open ocean: instead of using the standard 0.87 in association with 1.6, 2.1, or 3.7 μm spectral window bands, the algorithm uses 1.24 in association with 1.6, 2.1, or 3.7 μm window bands for which the sea-ice surface albedo is lower (Platnick et al. 2001). The changes of channels decrease the uncertainty due to surface-reflectance underestimation and overestimation in the measured reflectance to respectively 7% and 22%. Nevertheless the sea-ice reflectance increases the uncertainty of overlying-cloud properties (Platnick et al. 2014).

3.1.5 Cloud top height

Figure 3.7 represents the distribution of liquid and ice-cloud top pressure retrieved by POLDER between 2005 and 2010, considering spring, summer, and fall. Data are unavailable from the passive satellite during the polar night. It should be noted that the fall distribution only considers September. The mode of the distribution for liquid-cloud top pressure during summer and spring is 850 hPa, whereas the liquid-cloud top mode for fall is at 700 hPa.

Regarding ice-cloud tops, the values are naturally lower (higher cloud top in altitude) than liquid-cloud tops. The minimum is reached in spring with the mode of cloud top distribution at 750 hPa. In summer the mode of cloud top distribution is at 600 hPa. Finally, the highest ice clouds are observed during fall, with the mode of cloud top distribution at 450 hPa.

3.2 Pollution concentrations

Figure 3.8 shows the climatology of the spatial variability of low-altitude χ_{CO} for the Arctic between 2005 and 2010 from the GEOS-Chem numerical tracer transport model. Both anthropogenic and biomass-burning χ_{CO} vary through the year.

Regarding anthropogenic χ_{CO}, the maximum is found during winter for which the mean concentration reaches 80 ppb. This high concentration is due to faster transport occurring in winter (Stohl 2006; Quinn et al. 2007b). During spring the concentration decreases and is at a minimum in summer (30 ppb) following the decrease of the polar-dome extent during summer making the entrance of air parcels in the Arctic more difficult (Stohl 2006). Pollution is concentrated primarily above the European and East Asian sectors.

Regarding the pattern of biomass-burning χ_{CO}, the minimum values are observed in winter and fall with, on average, values close to 10 ppb because of fires in the northern hemisphere occurring in spring and summer. The average of biomass-burning χ_{CO} reaches a maximum in summer (37 ppb) but is generally lower than anthropogenic χ_{CO}. In June, July, and August, χ_{CO} reaches 200 ppb in the Siberian and North American sectors, since this is where biomass burning is concentrated.

Figure 3.9 shows the pie chart of pollution source regions for which the plumes reach the Arctic for both biomass-burning and anthropogenic plumes at every altitude. Re-

garding the anthropogenic source-region contribution, we observe that there is not a high variation across the different seasons. The main part comes from eastern Asia (48%), the second major source contributor is either Europe (16%), the rest of the world (16%), or the only marginally smaller contribution from Northeast America (14%). Finally, Northwest America has the smallest contribution (4.5%).

The biomass-burning source contribution is different. In winter there is no biomass burning in the northern hemisphere, the CO contribution is primarily from the rest of the world (52%). From source regions, air parcels traveling to the high troposphere can move to another continent in 1 to 2 weeks (Stohl 2001; Stohl et al. 2003; Holzer et al. 2005), so it is realistic that CO from remote biomass burning can reach the Arctic. In spring, the contribution of the rest of world to biomass-burning aerosol content in the Arctic is high (45.4%) but as shown in Figure 3.8, the primary contribution to arctic pollution is from anthropogenic origins. In summer, the contribution from the rest of the world drops to 11% and major contributors to biomass-burning aerosol content in the Arctic are Siberia (43.3%) and America (39.4%). During fall, the same conclusions as in summer apply, the contribution from the rest of the world is 18.5% and major contributors to biomass-burning aerosol content in the Arctic are Siberia (43.7%) and America (34.0%). For every season, Europe's contribution to biomass-burning arctic CO is low (below 1%). East Asia's part is also low (below 6%) except during spring (19%).

In addition to the pie charts, Figure 3.10 shows the monthly biomass burning fraction for low-level pollution plumes. From November to April, CO concentration is mainly from anthropogenic sources. In December the biomass burning fraction increases in East Siberia and North America. During summer, the biomass burning fraction increases and reaches a maximum of 0.57 on average in August.

3.2.1 Temporal variations of CO concentration

A biomass-burning concentration fraction is defined as the ratio of CO concentration from biomass-burning over CO concentration from biomass-burning and anthropogenic sources. Anthropogenic plumes are defined by a biomass-burning concentration fraction below 0.2, whereas a fraction above 0.8 identifies a biomass-burning pollution plumes.

Figure 3.11 shows the temporal frequency of biomass-burning and anthropogenic pol-

lution plumes, as a function of year. Significant biomass-burning events generally took place in 2008, 2009, and 2010. For anthropogenic air parcels the results are constant, except for the rare clean-anthropogenic events in 2008 and 2010. We note that polluted biomass-burning situations, defined as the upper quartile of biomass-burning CO concentration, were particularly high in 2008 and 2010. Doing a study on only one year or one season intrinsically focuses on pollution events of anthropogenic or biomass burning which are not necessarily representative to the arctic region. Long-term and statistical studies aim to provide a more general picture of the Arctic.

3.2.2 Geographical variation

Figure 3.12 represents the latitude distribution of biomass-burning pollution plumes and anthropogenic pollution plumes considering clean and polluted situation from GEOS-Chem χ_{CO}. Clean and polluted are defined as, respectively, the lower and upper quartiles of χ_{CO}. Polluted and clean anthropogenic pollution plumes are mainly located between 70 and 80°.

Polluted biomass-burning pollution plumes are primarily located at lower latitudes than clean biomass-burning pollution. The median value of latitude for polluted biomass-burning events is near 73°, and the median of latitude for clean biomass-burning pollution plumes is near 78°. Clean parcels might correspond to longer transport pathways that enter the polar dome from above (Stohl 2006). Polluted biomass-burning pollution plumes have higher occurrences at lower latitudes because they enter the polar dome through fast transport from Siberia at low levels.

Figure 3.13 shows the distribution of the longitudinal distributions of biomass-burning pollution plumes and anthropogenic pollution plumes considering clean and polluted χ_{CO} from GEOS-Chem. Polluted and clean air parcels exhibit similar variations as biomass-burning and anthropogenic pollution plumes. Anthropogenic plumes are less present around 50°W and 100°E, but have a maximum of occurrence around 0°E. Biomass-burning plume occurrences show the same minimum at 50°W but present a maximum at -180°W.

The minimum presented by both anthropogenic and biomass burning casts a light over the topographic barrier of Greenland, at 50°W, which prevents low-altitude pollution plumes from reaching the Arctic. Also, the Atlantic Ocean has the particularity of having

the polar dome boundaries at latitude northern to 70° (Stohl 2006), therefore, it is not a favorable pathway for aerosols.

3.3 Meteorological parameters of the Arctic

In this dissertation we primarily focus on two parameters of critical importance for cloud formation in the Arctic: The SH as a proxy of the atmospheric humidity and the LTS. We also show maps of the horizontal and vertical winds, identified as important components of the aerosol-cloud interaction (McFarquhar and Heymsfield 2001).

3.3.1 Winds

Vertical winds from ERA-I can increase the value of ACI by favoring the entrainment of aerosols in the cloud, enhancing the aerosol-cloud interaction (Andersen and Cermak 2015). Su et al. (2010) showed that vertical velocity has a direct impact on cloud properties such as r_e, albedo, and τ. Figure 3.14 shows the pressure velocity at 700 hPa and the horizontal winds at 700 hPa for the four seasons. The vertical velocity is represented by the color and horizontal winds by barb a signage system indicating the direction and strength. The wind considered here is retrieved by the method of large-scale wind field (Stohl et al. 1997). The method assumes that the vertical shear of the horizontal wind is horizontally more homogeneous than the wind profile itself. High-resolution wind profile measurements can be associated with low-resolution wind vertical profile.

In the horizontal wind field, we notice the presence of the arctic vortex: the counter-clockwise wind direction around the pole indicates low pressure, which is especially strong in fall and winter. Above the central Arctic Ocean, winds are generally below 15.3 $m\,s^{-1}$, except in fall when the winds can go up to 30.6 $m\,s^{-1}$.

Regarding the pressure velocity, values are generally low between -0.20 and 0.20 hPa^{-1} or between -0.02 and 0.02 $m\,s^{-1}$. A vertical velocity between -0.5 and 0.5 $m\,s^{-1}$ can increase the effect of aerosols on aerosol-cloud interactions by 40%, by increasing drop collisions and decreasing the effective radius (Schmidt et al. 2014). Our vertical velocity ranges are smaller than the ones considered by Schmidt et al. (2014). Zhang et al. (2016) found that the vertical-velocity impact on the ACI is not the primary factor, compared to lower tropospheric stability, for example, when the velocity is weak. Our range of vertical velocity is

low (Su et al. 2010), so we do not constrain for vertical velocity in the rest of the study.

3.3.2 Specific humidity

Figure 3.15 shows the monthly averaged map of the SH at 700 hPa from ERA-I, retrieved between 2005 and 2010. There is an increase of the SH in the late spring and summer, with a maximum mean of SH above the ocean of approximately 1.9 g kg^{-1} in July that decreases to 0.5 g kg^{-1} in February. There is a persistent minimum in the northern region of Greenland, corresponding to the presence of sea ice, except in May where the minimum is around the Svalbard region.

SH above land is generally greater than above the ocean and this difference is intensified during summer, whereas values are more uniform during winter. For example, in August the SH above land has an average of 4 g kg^{-1}, whereas it does not exceed 2 g kg^{-1} above the ocean. In February the difference between land and the ocean does not exceed 0.3 g kg^{-1} for latitudes higher than 65°. Comparing to seasonal variations of open ocean (c.f. the Appendix), SH follows the same pattern, with a maximum in July and a minimum in February.

3.3.3 Lower tropospheric stability

LTS is defined as the difference in potential temperature between the surface and 700 hPa (Klein and Hartmann 1993). The topography in the Arctic is high in some regions and reaches 2,800 m on the eastern part of Greenland and the highest Alaskan peak, Denali, at 6,198 m. To avoid topographic effects, we only examine LTS values above the ocean.

Figure 3.16 shows the monthly averaged map of LTS from ERA-I between 2005 and 2010. The different maps show a decrease of the LTS during late spring and summer, with a minimum mean value of LTS of 16 K in October and an increase in February to 25 K.

Regarding geographical variations, the maximum of LTS lies generally above sea ice (c.f. the Appendix). In winter, the mean LTS above sea ice is 25 K and drops to 12 K over open ocean. In summer, the difference in mean LTS between the two surfaces is 1.5 K. A cold surface decreases the potential-temperature difference between the surface and 700 hPa, thereby, increasing the LTS.

3.3.4 Monthly variability coincident with liquid cloud

Figure 3.17 shows the 2D histogram of the SH and LTS for data between 2005 and 2010 coincident with liquid arctic clouds. Different colors correspond to different months with the maximum number of measurements of the associated value of SH and LTS. For example, the point corresponding to 17 K and 0.7 $g\,kg^{-1}$, respectively, for the LTS and the SH, occurs more often in May than other months.

Minimal values of SH are in April with values ranging from 0.15 and 0.4 $g\,m^{-2}$ and the maximum is in August and September with values ranging from 3 and 10 $g\,m^{-2}$. The variation is anticorrelated with sea-ice extent (e.g., the Appendix) which reaches a maximum in March and a minimum in September. For LTS, we do not have a clear separation between month as for the SH.

Figure 3.17 suggests that looking at a particular month or season of the year controls indirectly the meteorological conditions of the atmosphere. When a particular regime of SH and LTS is considered, a special season of the year is analyzed. As an example, in the following study, we consider SH from 2 to 4 $g\,kg^{-1}$ and LTS from 17 to 22 K (explained later). These values are characteristic of June, July, August, and September. Our study does not draw conclusions on specific cases, our large sample of data points allows us to control for different regimes of meteorological parameters.

Figure 3.17 refers to a monthly variability of meteorological parameters, but from this chapter we can conclude that CO concentration and CO source types vary by season and year: CO concentration is higher during winter and early spring, dominated by anthropogenic pollution plumes, whereas in summer biomass burning fraction increases but the total CO concentration decreases. Events are also varying depending on a yearly basis. Anthropogenic CO comes from Europe and Asia, and BB CO are from Siberia and North America. The use of large datasets covering several years and regions allows our results to not be biased by specific events.

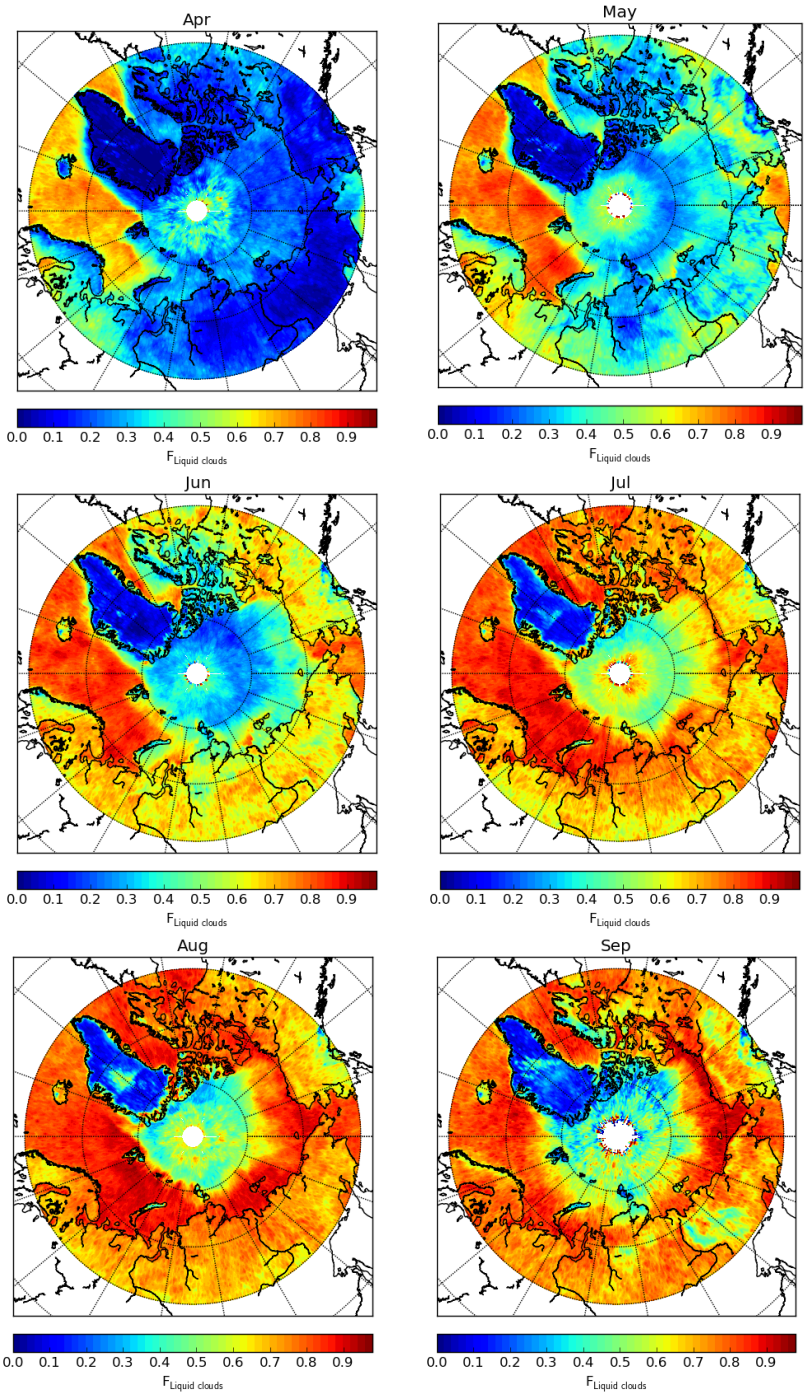

Figure 3.1: Monthly frequency of liquid clouds referring to low-level clouds over the Arctic from MODIS and POLDER instrument from April 2005 to September 2010 for a layer between 700 and 1,013 hPa.

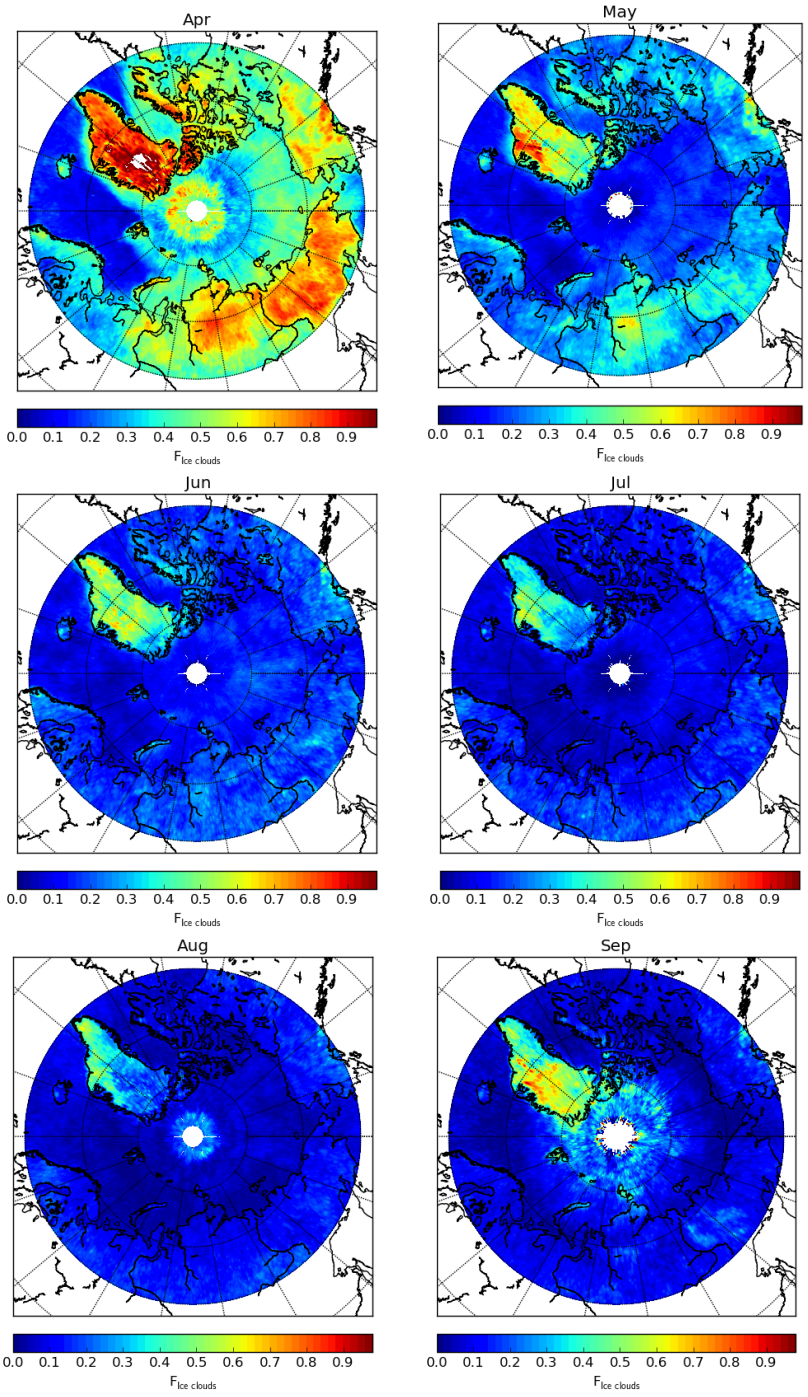

Figure 3.2: Monthly frequency of ice clouds referring to low-level clouds over the Arctic from MODIS and POLDER instrument from April 2005 to September 2010 for a layer between 700 and 1,013 hPa.

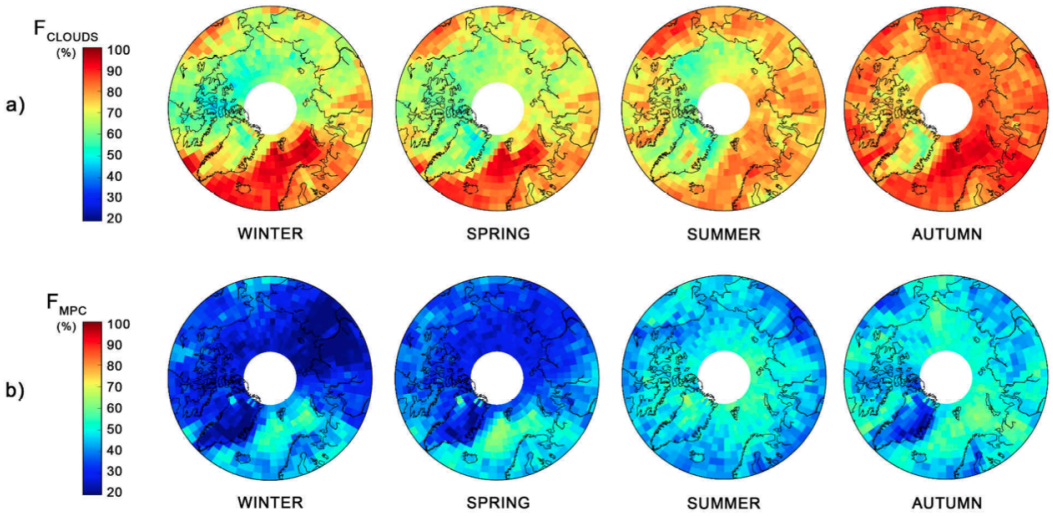

Figure 3.3: Stereographic projections of the seasonal occurrence of all clouds and mixes-phase clouds (MPCs). Row (a) corresponds to all clouds (referring to time) and row (b) corresponds to MPCs (referring to clouds). Occurrences are computed taking into account the 500 to 12,000 m altitude range (Mioche et al., 2014).

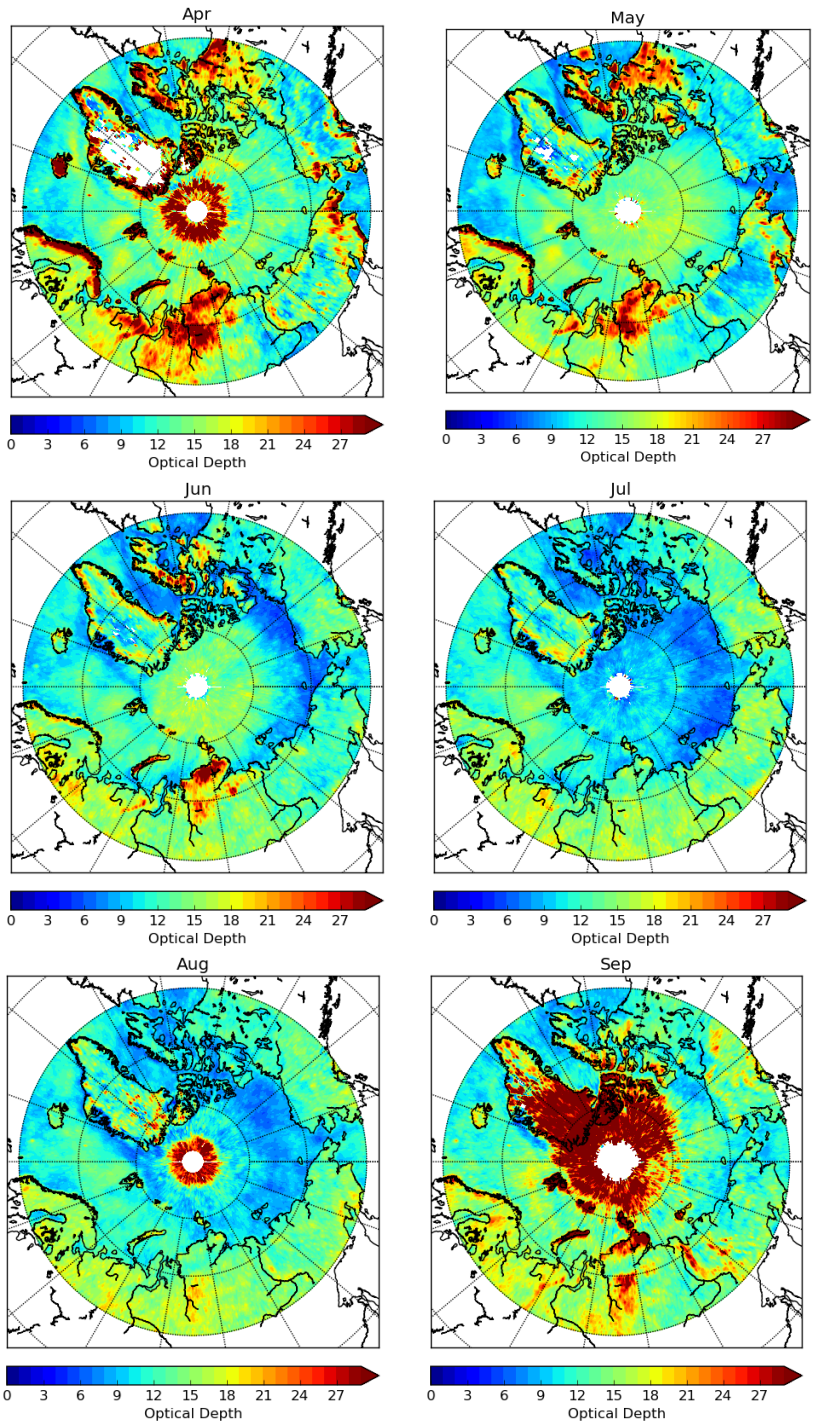

Figure 3.4: Monthly liquid cloud optical depth over the Arctic from MODIS instrument from April 2005 to September 2010 for a layer between 700 and 1,013 hPa.

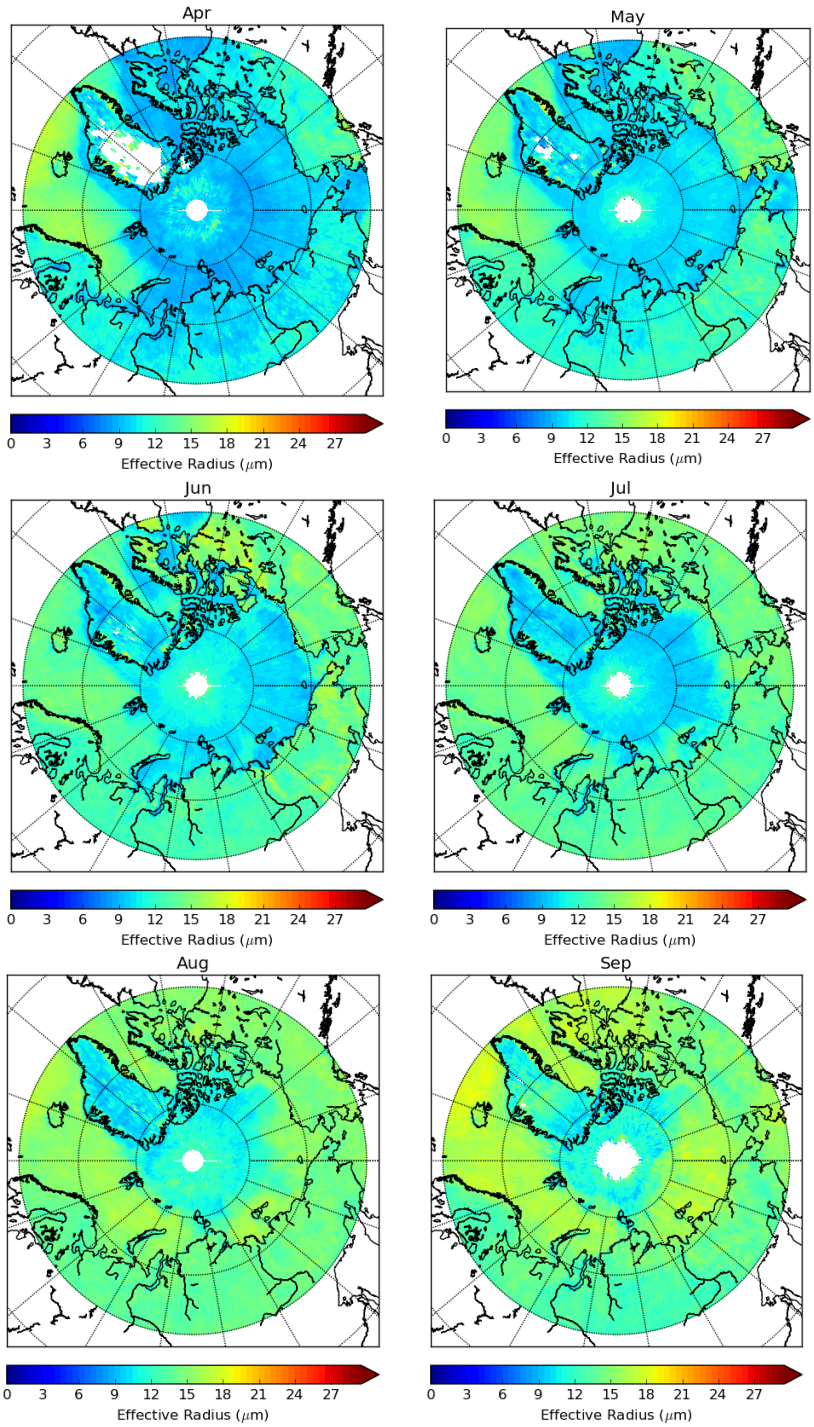

Figure 3.5: Same as Figure 3.4 but considering the liquid-cloud-droplet effective radius.

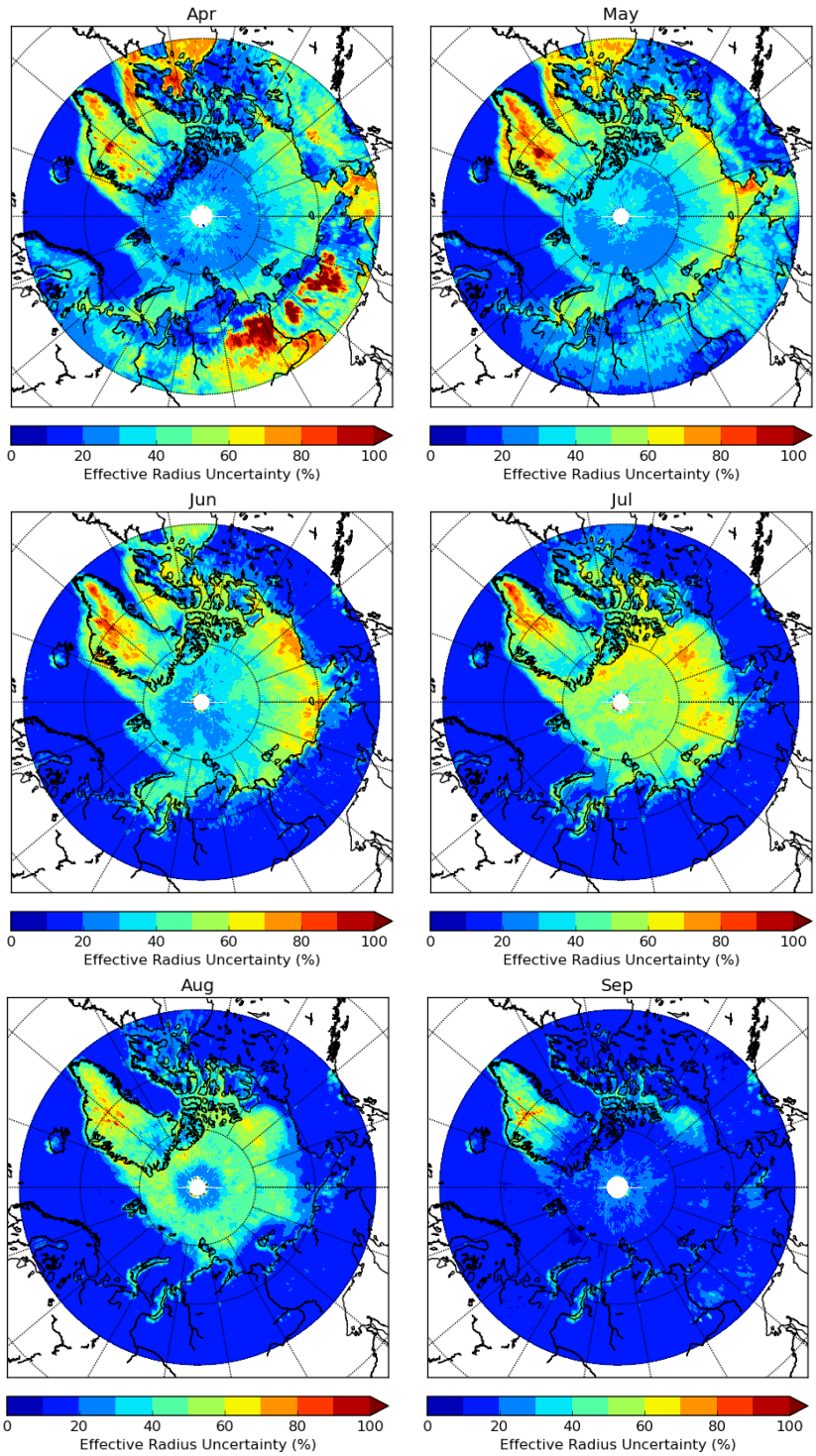

Figure 3.6: Monthly liquid cloud effective radius uncertainty over the Arctic from MODIS instrument from April 2005 to September 2010 for a layer between 700 and 1,013 hPa.

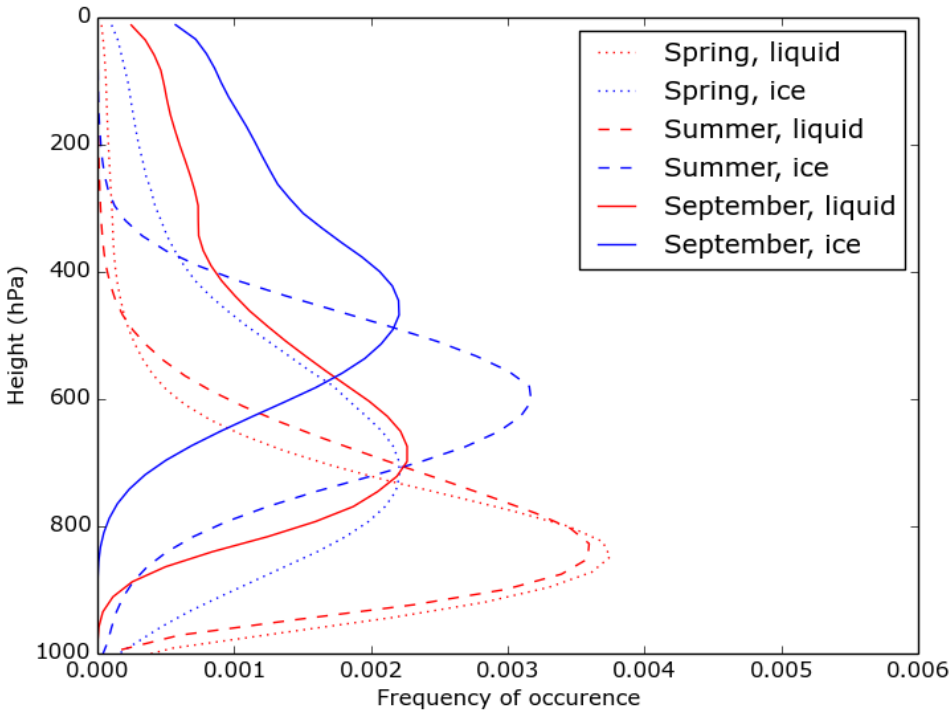

Figure 3.7: Normalized distributions of liquid and ice-cloud heights for different seasons from March 2005 to September 2010 above the arctic circle from POLDER-3 cloud top height.

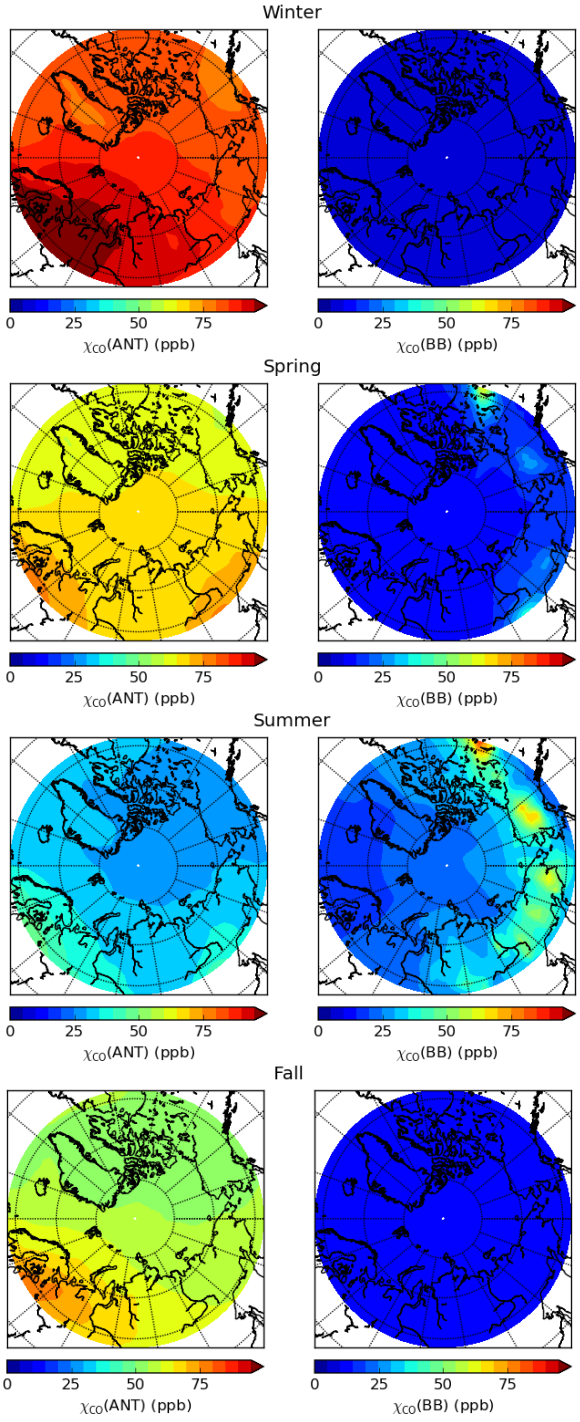

Figure 3.8: Map of the seasonal average of the CO concentration between 975 and 800 hPa and between 2005 and 2010 from GEOS-Chem. On the left, maps represent the anthropogenic CO concentration, and on the right maps represent the biomass-burning CO concentration.

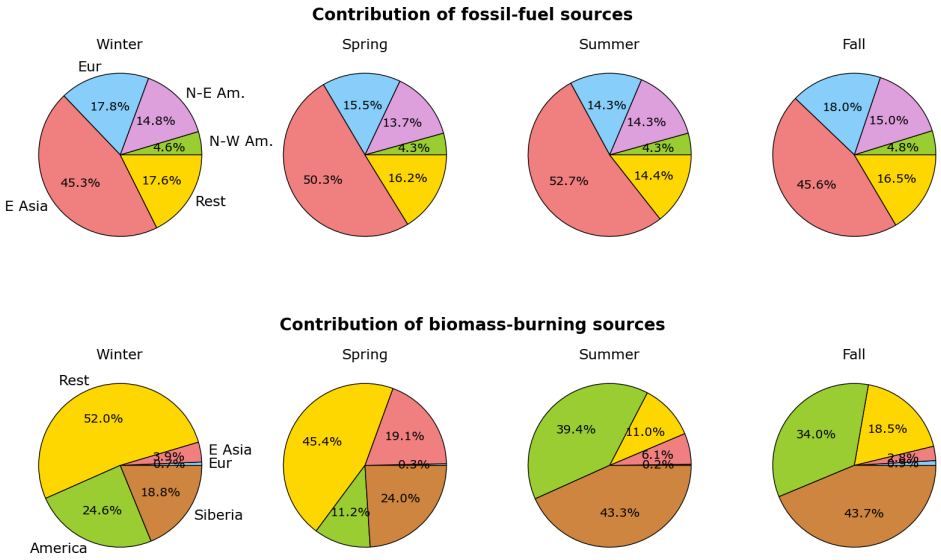

Figure 3.9: Pie charts of seasonal CO source regions from which pollution plumes reach the Arctic from GEOS-Chem model. The figure distinguishes fossil-fuel (top) and biomass-burning (bottom) combustion out of total.

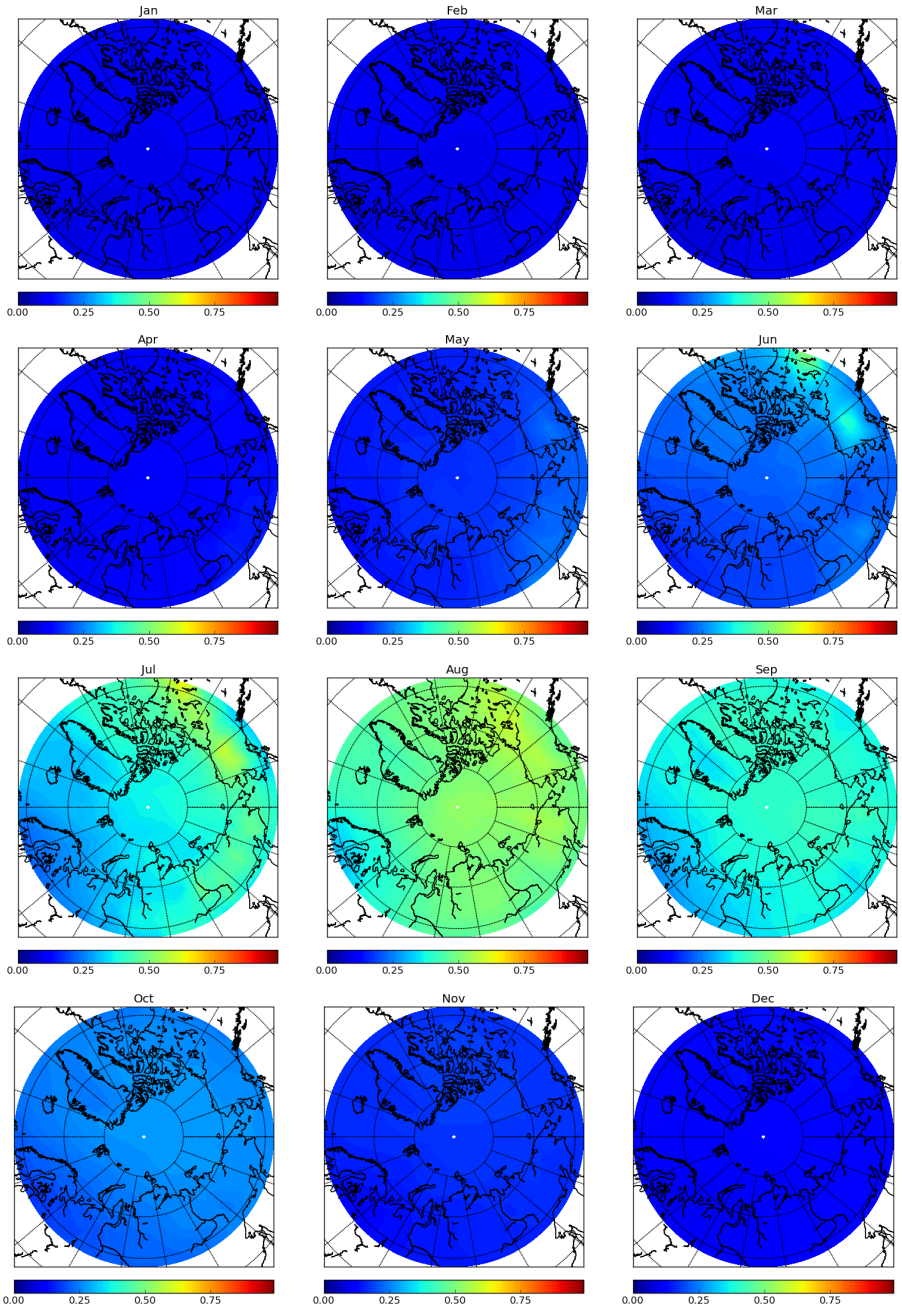

Figure 3.10: Map of the monthly average of biomass burning fraction between 975 and 800 hPa and between 2005 and 2010 from GEOS-Chem.

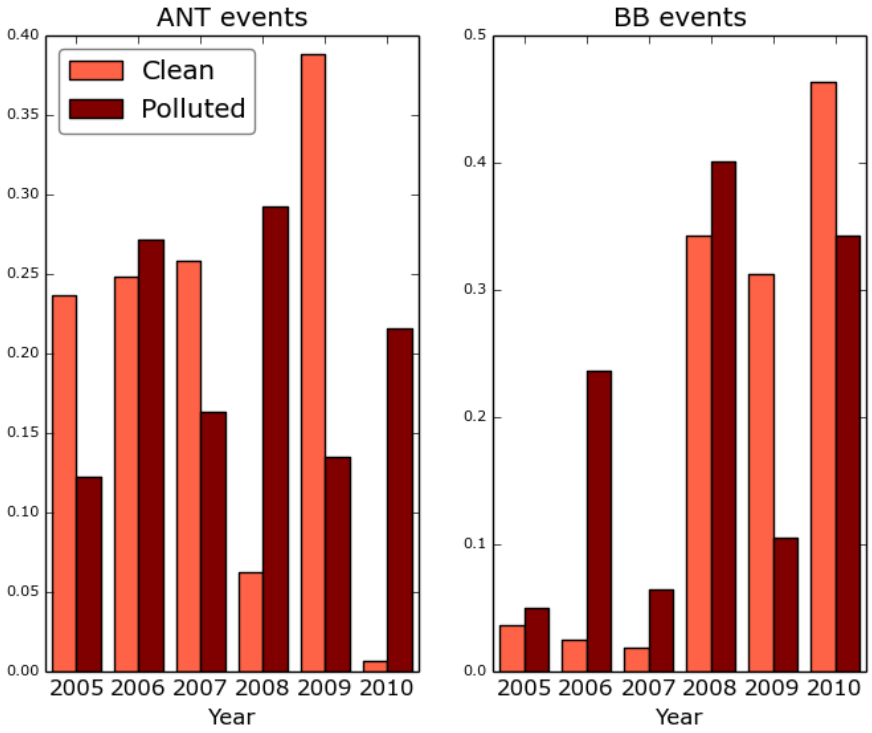

Figure 3.11: Temporal distribution of the CO-concentration yearly averaged from 2005 to 2010 retrieved by GEOS-Chem for the arctic region (latitude greater than 65°). We differentiate anthropogenic pollution plumes to biomass pollution by considering the biomass-burning concentration fraction. A fraction below 0.2 identifies anthropogenic pollution plumes and a fraction above 0.8 identifies a biomass-burning pollution plumes. Polluted and clean plumes are identified considering respectively the upper and lower quartile of CO concentration.

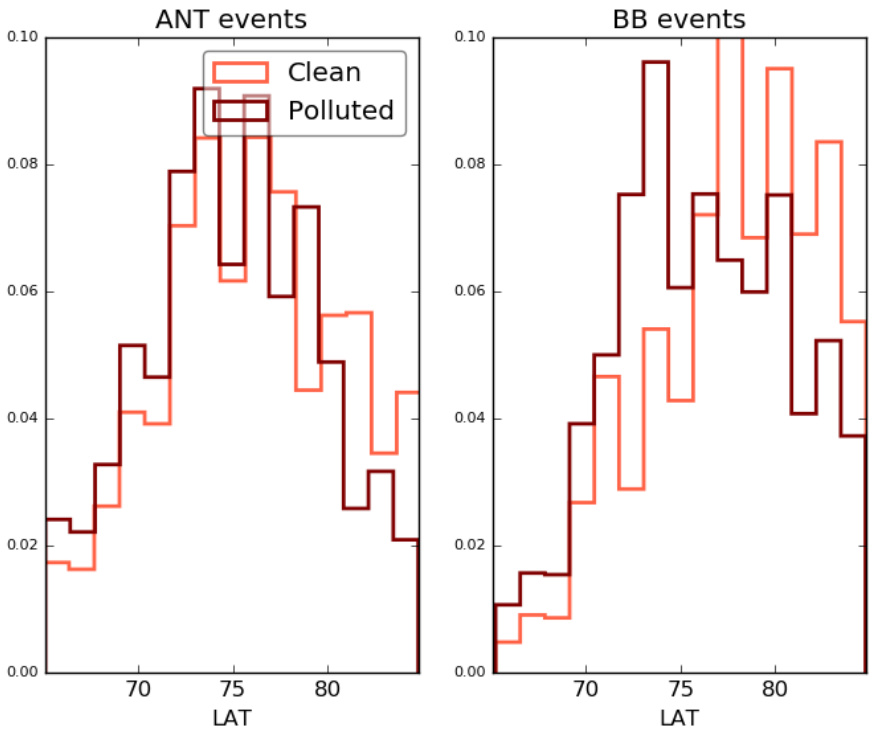

Figure 3.12: Geographical distribution of plumes by latitude.

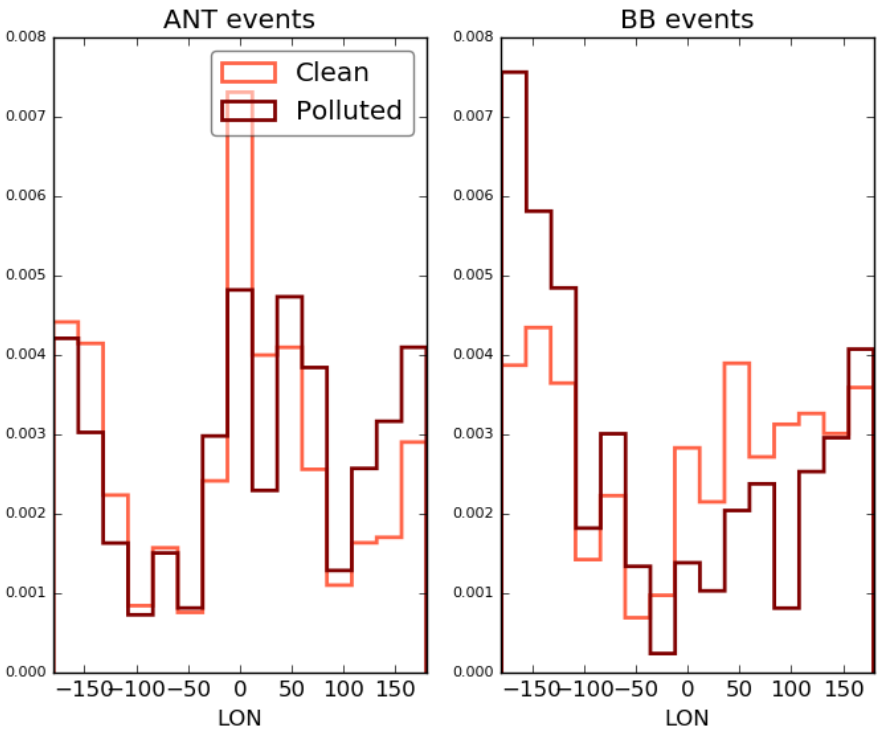

Figure 3.13: Same as Figure 3.11 considering the geographical distribution of longitudes.

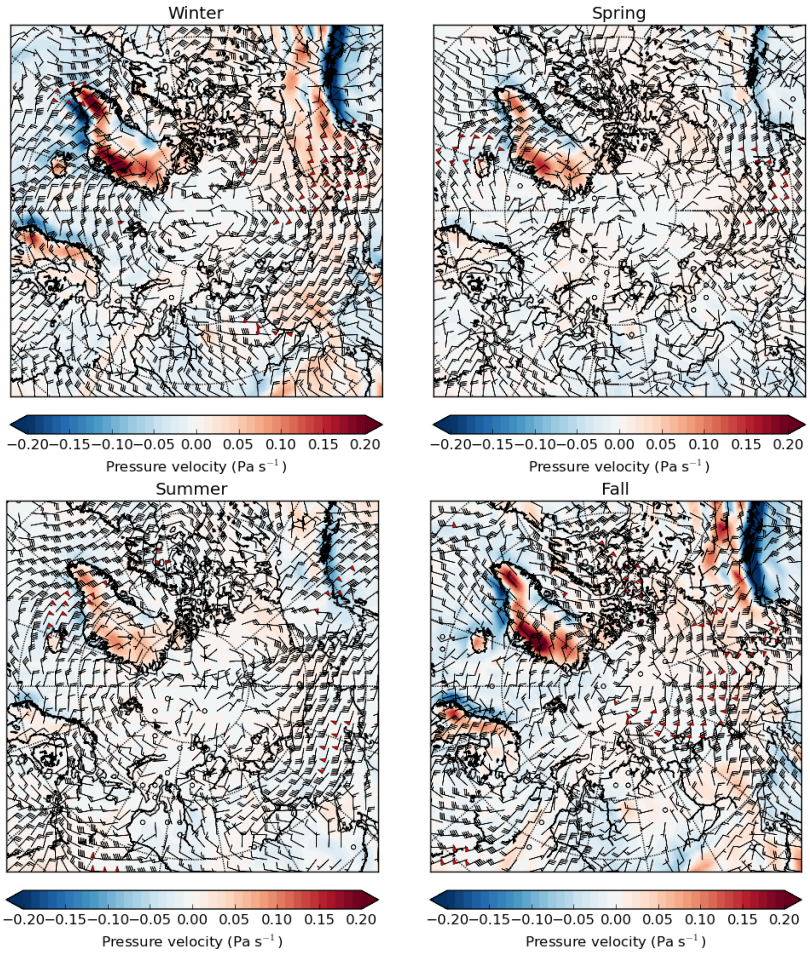

Figure 3.14: Map of seasonally averaged horizontal winds at 700 hPa between 2005 and 2010 from ERA-I displayed in wind barbs in knots. The pressure velocity at 700 hPa is also shown by the color scale. Winter is defined as January-February-March, spring is defined as April-May-June, summer as July-August-September, and fall as October-November-December.

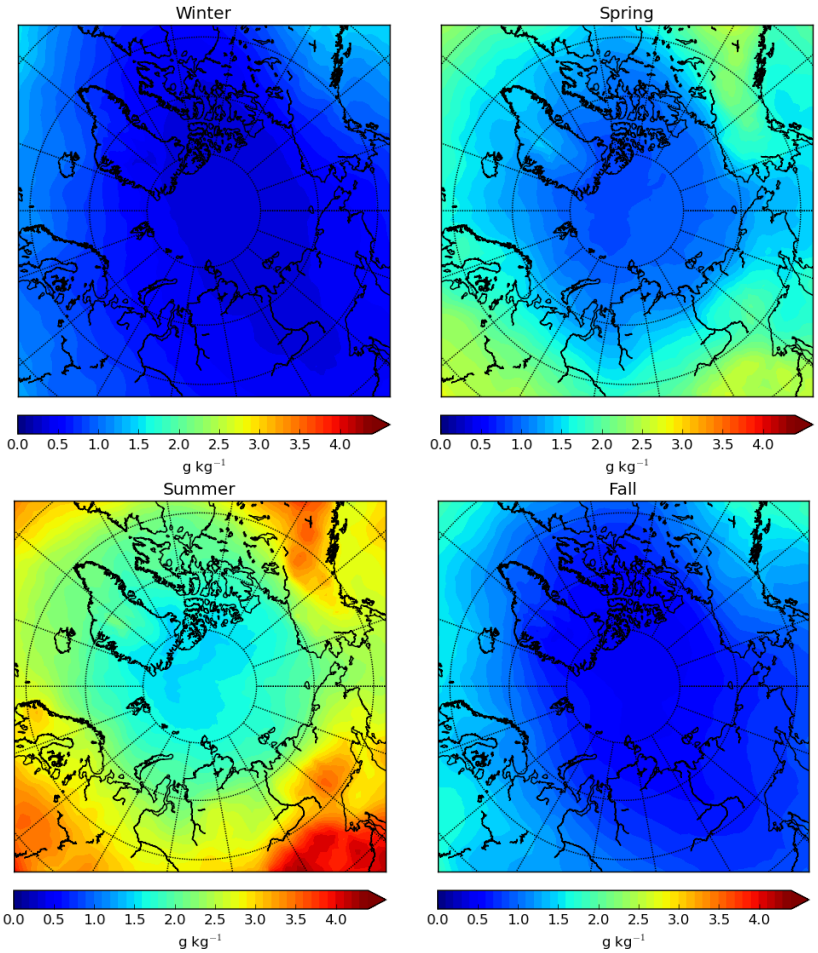

Figure 3.15: Map of seasonally averaged specific humidity at 700 hPa between 2005 and 2010 from ERA-I. Winter is defined as January-February-March, spring is defined as April-May-June, summer as July-August-September, and fall as October-November-December.

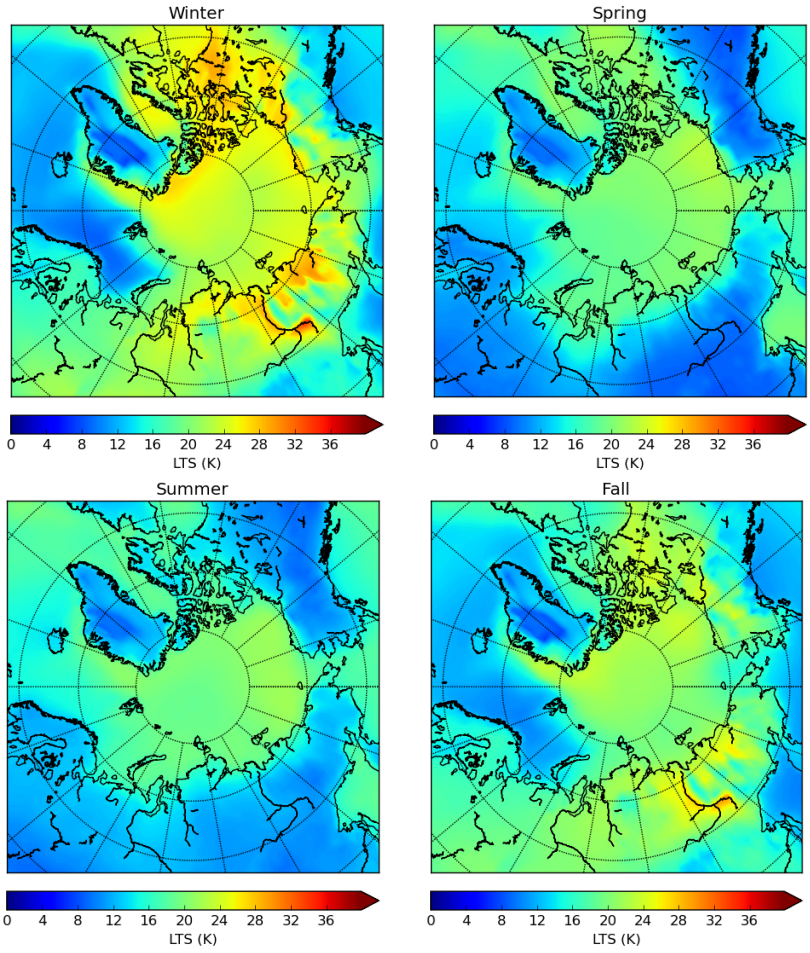

Figure 3.16: Same as Figure 3.16 but for the lower tropospheric stability.

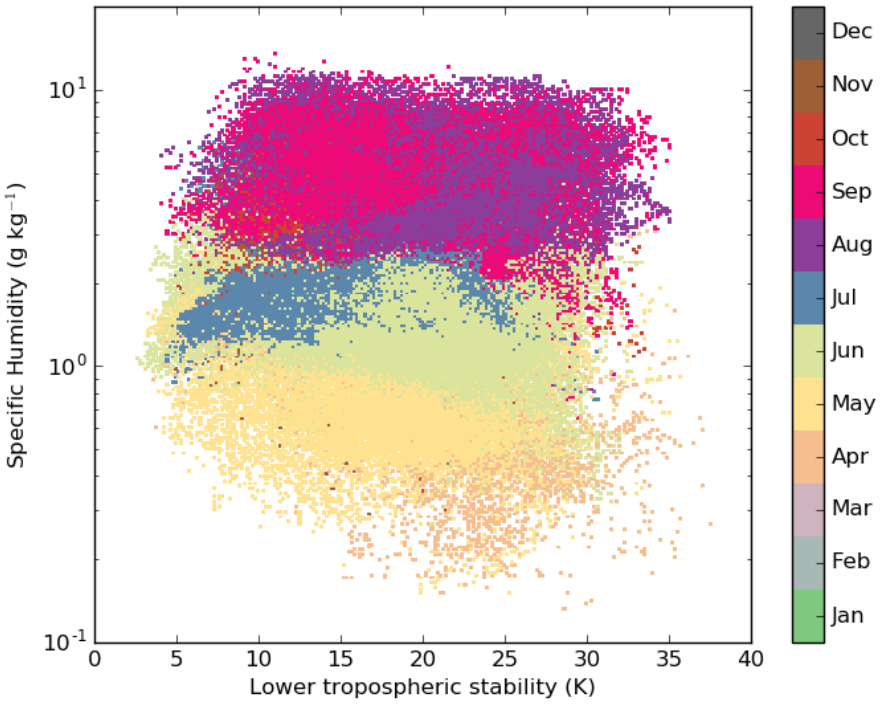

Figure 3.17: 2D histogram of the specific humidity and the lower tropospheric stability between 2005 and 2010 coincident with liquid low-level clouds with latitudes greater than 65°. Each point is associated with the month when it is most likely to be retrieved.

CHAPTER 4

EFFECT OF LONG-RANGE AEROSOL TRANSPORT ON THE MICROPHYSICAL PROPERTIES OF LOW-LEVEL LIQUID CLOUDS IN THE ARCTIC

The properties of low-level liquid clouds in the Arctic can be altered by long-range pollution transport to the region. Satellite, tracer transport model, and meteorological data sets are used here to determine a net aerosol-cloud interaction (ACI^{net}) parameter that expresses the ratio of relative changes in cloud microphysical properties to relative variations in pollution concentrations while accounting for dry or wet scavenging of aerosols en route to the Arctic. For a period between 2008 and 2010, ACI^{net} was calculated as a function of the cloud liquid water path, temperature, altitude, specific humidity, and lower tropospheric stability. For all data, ACI^{net} averages 0.12 ± 0.02 for cloud droplet effective radius and 0.16 ± 0.02 for cloud optical depth. It increases with specific humidity and lower tropospheric stability and is highest when pollution concentrations are low. Carefully controlling for meteorological conditions we find that the liquid water path of arctic clouds does not respond strongly to aerosols within pollution plumes. Or, not stratifying the data according to meteorological state can lead to artificially exaggerated calculations of the magnitude of the impacts of pollution on arctic clouds.

Chapter 4 is based on an article published in Atmospheric Chemistry and Physics. Coopman, Q., T. J. Garrett, J. Riedi, S. Eckhardt, and A. Stohl (2016). "Effects of long-range aerosol transport on the microphysical properties of low-level liquid clouds in the Arctic" in: Atmospheric Chemistry and Physics 16.7, pp. 4661-4674.

4.1 Introduction

Due to growing concentrations of greenhouse gases and complex feedback processes, the Arctic region has warmed approximately two times faster than the global average (Serreze and Francis 2006; Serreze et al. 2009; Richter-Menge and Jeffries 2011), a trend that is anticipated to continue through this century (Yoshimori et al. 2013; Overland and Wang 2013). Further, the Arctic is not pristine, even if it is remote from industrialized areas and major aerosol sources. Midlatitude aerosols can be transported to northern latitudes in relatively high concentrations when precipitation rates are low and there are strong temperature inversions that inhibit vertical mixing (Sirois and Barrie 1999; Law and Stohl 2007; Quinn et al. 2007b; Law et al. 2014). The origins of arctic haze tend to be pollution from Eurasia (Shaw 1995; Stohl 2006; Shindell et al. 2008; Ancellet et al. 2014), and boreal forest fires in North America, Eastern Europe, and Siberia (Stohl 2006; Stohl et al. 2006). Between spring and summer, the atmosphere becomes cleaner due to an increase in wet-scavenging (Garrett et al. 2010).

Such aerosols have the potential to alter cloud properties in the Arctic (Garrett and Zhao 2006; Lance et al. 2011). On one hand, thin low-level clouds with more numerous smaller droplets can radiate more long wave radiation thereby warming the surface (Garrett et al. 2002, 2004; Garrett and Zhao 2006). On the other hand, polluted clouds can reflect more sunlight, leading to a cooling effect (Lubin and Vogelmann 2007). Zhao and Garrett (2015) found that seasonal changes in surface radiation associated with haze pollution range from +12.2 $\mathrm{W\,m^{-2}}$ in February to -11.8 $\mathrm{W\,m^{-2}}$ in August. Annually averaged, the longwave warming and shortwave cooling nearly compensate, although the seasonal timing of the forcing may have implications for rates of sea ice melt (Belchansky et al. 2004; Markus et al. 2009).

The influence of aerosols on cloud microphysical properties is often quantified using an indirect-effect (IE) or aerosol-cloud interactions (ACI) parameter that expresses the ratio of relative changes in cloud microphysical properties to variations in pollution concentrations, most typically aerosol index, the aerosol optical depth, the aerosol concentration, or the cloud condensation nucleus (CCN) concentration (Feingold et al. 2001; Feingold 2003a). Where the parameter is expected to decrease with increasing aerosols or cloud condensation nuclei (e.g., the effective radius), the ratio is multiplied by negative one so

that the IE or ACI is positive.

Garrett et al. (2004) used ground-based retrievals of cloud-droplet effective radius and surface measurements of dried aerosol light scattering from Barrow (Alaska) to obtain a value for the cloud-droplet effective radius ACI that lies between 0.13 and 0.19. Satellite measurements show that ACI values for cloud-droplet effective radius range from 0.02 to 0.20 for midlatitude continental clouds (Nakajima et al. 2001; Feingold 2003b; Lohmann and Feichter 2004; Myhre et al. 2006) and from 0.03 to 0.15 for midlatitude oceanic clouds (Breon et al. 2002; Sekiguchi 2003; Kaufman et al. 2005; Myhre et al. 2006; Costantino and Bréon 2013; Wang et al. 2014). Satellite instruments have the advantage of providing data over large spatial scales, however satellite retrievals of aerosol concentrations are normally obtained from air columns close to the analyzed cloud. The assumption is made that plumes are horizontally homogeneous both within and without the cloud, and that they are vertically colocated with cloud top (Nakajima et al. 2001; Feingold et al. 2001; Sekiguchi 2003). For large-scale cloud studies, this method potentially introduces bias since it is not obvious that pollution should be uniform for different meteorological regimes.

Colocating satellite cloud retrievals with pollution tracer output from a chemical transport model offers an alternative approach for assessing the effect of pollution on clouds (Berg et al. 2011; Lance et al. 2011; Tietze et al. 2011). Cloud microphysical properties and pollution concentrations can be estimated at the same time, location, and meteorological regime (Schwartz et al. 2002; Kawamoto et al. 2006; Avey et al. 2007). Active tracers experience both sources and sinks through wet scavenging, dry deposition, and chemical reactions that can be difficult to accurately model. Passive pollution tracers, on the other hand, are determined only by source emission strength and subsequent dilution. An example of a passive tracer is carbon monoxide (CO), which is a combustion by-product that correlates with the anthropogenic CCN close to pollution sources (Longley et al. 2005). Since both are found in pollution plumes, CO can serve as a passive proxy for CCN that is relatively straight-forward to model. A difference is that, unlike CCN, CO is unaffected by wet and dry scavenging. In the absence of scavenging, a linear relation exists between CCN and CO and it should be possible to see changes in clouds when CO concentrations are high. But if CCN have been scavenged from pollution plumes, then the observed sensitivity of clouds to the pollution plumes should be expected to be low. Thus passive

tracers serve as an indicator of the net effect of pollution plumes on clouds that accounts for the effect of scavenging during transport en route to the clouds themselves.

More generally, the primary control on cloud microphysical properties is not aerosols but rather meteorological conditions during cloud formation (Chang and Coakley 2007; Brenguier and Wood 2009; Kim et al. 2008; Painemal et al. 2014; Andersen and Cermak 2015). For example, a reduced stability of the environmental temperature profile can allow for enhanced cloud-droplet growth through increasing convection (Klein and Hartmann 1993). This would be expected to lead to greater mixing of the aerosols with the cloudy air and greater aerosol impacts on cloud microphysical properties (Chen et al. 2014; Andersen and Cermak 2015). Also, in the Arctic during the winter, pollution plumes from Asia are often associated with higher values of potential temperature than pollution plumes from Europe (Stohl 2006). Thus, the observed impact of pollution plumes on clouds may be correlated with a particular meteorological regime.

Using the approach of colocating a passive tracer from a tracer transport model with satellite observations, Tietze et al. (2011) presented an analysis of pollution-cloud interactions over the Arctic from March to July 2008. Anthropogenic and biomass-burning aerosol pollution was represented using a CO passive tracer in the FLEXPART (FLEXible PARTicle dispersion model) tracer model (Stohl et al. 2005) as a proxy. CO was colocated with POLDER-3 (Polarization and Directionality of the Earth's Reflectance) and MODIS (Moderate Resolution Imaging Spectroradiometer) observations. Tietze et al. (2011) showed that the sensitivity of liquid-cloud effective radius (r_e) and optical depth (τ) to pollution has a maximum around the freezing point, and that the sensitivity decreases for both higher and lower temperatures. The optical depth was generally up to four times more sensitive than the effective radius. Their results also suggested that biomass-burning pollution has a smaller yet significant impact on liquid-cloud microphysical properties than anthropogenic pollution, and that the ACI parameters depend on altitude, liquid water path (LWP), and temperature.

Our study extends the Tietze et al. (2011) research by adding two years of data, 2009 and 2010 and, in addition to temperature, stratifying the results by lower tropospheric stability (LTS) and atmospheric specific humidity (SH) (Matsui et al. 2006; Mauger and Norris 2007). Our results highlight the importance of considering meteorological conditions when

assessing the aerosol impact on cloud microphysical properties to show that r_e and τ have similar sensitivities to pollution.

4.2 Data

The analyses in this study are based on a colocation of satellite retrievals of cloud properties, tracer transport model simulations of pollution locations and concentrations, and reanalysis datasets for meteorological fields. The different datasets are described in Chapter 2 and also presented in Table 4.1. Since the focus here is on the effect of anthropogenic pollution on clouds, only FLEXPART cells where anthropogenic sources comprise more than 80 % of total CO concentrations are considered for comparison with cloud properties.

4.3 Methodology

This study examines data between 2008 and 2010 over the ocean at latitudes greater than 65°. Passive satellite sensors measure interactions of solar radiation with the atmosphere so as to retrieve cloud microphysical parameters of interest from visible wavelength measurements so analyses are restricted to the period between 1 March and 30 September.

4.3.1 Colocation of satellite retrieval and model pollution tracer fields

Here, as with many prior studies looking at aerosol-cloud interactions in the Arctic, we consider only low-level clouds (Garrett et al. 2004; Garrett and Zhao 2006; Lubin and Vogelmann 2006; Mauritsen et al. 2011), with POLDER cloud top altitudes between 200 and 1000 m, and between 1000 and 2000 m. The cloud top pressure translates to cloud top altitude by a pressure profile specific to the Arctic region. These two layers correspond to the FLEXPART vertical bin resolution. We average POLDER and MODIS data that falls within the height bins so that they are colocated with the corresponding FLEXPART CO concentrations.

4.3.2 The net aerosol-cloud interactions parameter

Assuming a constant LWC and a monodisperse size distribution of cloud droplets, the droplet effective radius (r_e) decreases as the CCN number concentration N_c increases

following the relation (Feingold et al. 2001):

$$\frac{\mathrm{d}\ln r_\mathrm{e}}{\mathrm{d}\ln N_\mathrm{c}}\Big|_{\mathrm{LWP}} = -\frac{1}{3}. \tag{4.1}$$

Here, we take a different approach which is to examine how cloud properties change in response to changes in a CO tracer under the presumption that the CO tracer serves as a proxy for the potential of long-range pollution transport, of which CCN may be a part. Of course, $\mathrm{N_c}$ and CO tracer concentrations (χ_{CO}) do not represent the same quantity. However, cloud condensation nuclei and CO are both by-products of combustion. The two quantities are expected to be highly correlated close to pollution sources where relative changes in one can serve as a proxy for relative changes in the other (Avey et al. 2007; Tietze et al. 2011). The reason for using CO is twofold. First, CO is passive and therefore easier to represent in a dynamic model. Second the analysis here is less focused on the local physics of aerosol-cloud interactions and more focused on the actual impact of anthropogenic activities on clouds far from combustion sources. These are similar but not identical questions. The aerosol-cloud interactions (or the ACI) parameter addresses the precise physics of the extent to which aerosols can modify clouds. However, interactions are a two-way street: where aerosols have been scavenged en route to distant clouds, then the potential is for a pollution plume to be present but its impact on cloud properties weak. To account for scavenging, we employ the term ACI^{net} or the net aerosol-cloud interaction parameter. ACI^{net} is the same as the ACI while additionally accounting for any reduction of the ACI due to dry or wet scavenging of aerosols during transport. ACI^{net} can be interpreted as a measure of the sensitivity of a cloud at any given location to pollution plumes from distant sources. It allows for the passive components of a plume (e.g., CO) to remain while aerosols have been removed

$$\mathrm{ACI}_{\tau}^{net} = \frac{\mathrm{d}\ln\tau}{\mathrm{d}\ln\chi_{\mathrm{CO}}} \tag{4.2}$$

$$\mathrm{ACI}_{r_\mathrm{e}}^{net} = -\frac{\mathrm{d}\ln r_\mathrm{e}}{\mathrm{d}\ln\chi_{\mathrm{CO}}} \tag{4.3}$$

For example, in the absence of scavenging, $\mathrm{N_c}$, from Eq. (4.1) is linearly related with χ_{CO} and Eq. (4.3) will be bound by a theoretical maximum value of $\mathrm{ACI}_{\mathrm{r_e}}^{\mathrm{net}} = 1/3$ (Twomey 1977; Feingold et al. 2001). Further from source regions, the correlation of CO concentration and aerosols is invariant to dilution but it may be affected by wet and dry scavenging

(Garrett et al. 2010, 2011). If scavenging rates are low, CO and CCN tend to covary, but when precipitation is high along transport pathways then aerosols are removed and values of ACI^{net} will tend to be lower. Garrett et al. (2010) found that at Barrow, Alaska, when the temperature exceeds 4 °C at the surface, wet scavenging efficiently removes CCN from the atmosphere. In this event, cloud microphysical properties will not affected by pollution plumes.

Since r_e and the optical depth (τ) are linked through $\tau = \frac{3}{2}\frac{LWP}{\rho_w r_e}$ for homogeneous clouds it follows that

$$\frac{\mathrm{d}\ln\tau}{\mathrm{d}\ln\chi_{CO}} = -\frac{\mathrm{d}\ln r_e}{\mathrm{d}\ln\chi_{CO}} + \frac{\mathrm{d}\ln \mathrm{LWP}}{\mathrm{d}\ln\chi_{CO}} \tag{4.4}$$

or,

$$\mathrm{ACI}_{\tau}^{net} = \mathrm{ACI}_{r_e}^{net} + \mathrm{ACI}_{\mathrm{LWP}}^{net}. \tag{4.5}$$

Figure 4.1 shows an example of how ACI^{net} is calculated for temperatures between −12 and 6 °C and altitudes between 1000 and 2000 m, for all LWP values. We first calculate $ACI_{r_e}^{net}$ as the linear fit of the natural logarithm of the effective radius to the natural logarithm of CO concentrations. The fit used in this study is based on the robust linear method (RLM) (Huber 1973, 2011; Venables and Ripley 2013). RLM uses an iterative least squares algorithm: every measurement has initially the same weight; The weights of each point are updated giving a lower weight to points that appear as outliers with respect to the entire dataset. The process iterates several times and stops when the convergence tolerance of the estimated fitting coefficients lies below 10^{-8}. The slope is therefore less sensitive to outlier points. In Figure 4.1, points indicated by the red line are weighted similarly to those indicated by black and blue lines. The slope retrieved by the linear fit, in Figure 4.1, is -0.13 ± 0.016. Referring to Eq. (4.3), $ACI_{r_e}^{net}$ equals +0.13 ± 0.016.

4.3.3 Stratifying the data for specific humidity and lower tropospheric stability

Figure 4.2 presents a 2-D histogram of frequency distribution of the SH and the LTS (See Chapter 2 for the definition of SH and LTS). The LTS ranges from 2.1 to 37 K and the SH from 0.13 to 11 $g\,kg^{-1}$. The median values for SH and LTS are 2.0 $g\,kg^{-1}$ and 19 K, respectively.

Table 4.2 describes the method used here to stratify the dataset according to meteorological conditions. We identify a range in LTS and SH that occupies 15 % of the total space of observed values but that is centered at the mode of the respective distributions. The total LTS range is 2.1 to 37 K, so the interval size is 5.3 K. The SH is distributed over several orders of magnitude. To better represent the distribution, we use a logarithmic scale for this parameter. The logarithm base 10 of SH has an interval of 0.28. The most common values of a meteorological state, defined here as the maximum number of measurements, is delimited by the red rectangle in Figure 4.2. The rectangle corresponds to a range between 2.0 $g\,kg^{-1}$ to 4.0 $g\,kg^{-1}$ for SH, and a range of 16.5 K to 21.8 K for LTS. From Figure 3.17, these ranges correspond to a time period from June to September. It is these ranges that are focused upon for calculation of the ACI^{net} parameter. We assume these intervals are sufficiently narrow that the variability within the interval has limited impact on cloud microphysics.

We also consider clouds with values of LWP greater than 40 $g\,m^{-2}$ separately from clouds with LWP values less than 40 $g\,m^{-2}$. This approach separates clouds according to their thermal radiative properties since a cloud with low LWP will tend to act as a gray-body and potentially be radiatively susceptible to pollution at thermal wavelengths (Garrett and Zhao 2006; Lubin and Vogelmann 2006; Mauritsen et al. 2011). Thick clouds act as blackbodies, and their longwave radiative properties are determined by temperature only (Garrett and Zhao 2006; Garrett et al. 2009).

4.4 Results

4.4.1 Net Aerosol-Cloud Interactions

Figure 4.3 summarizes ACI^{net} values calculated using combined POLDER-3, MODIS, and FLEXPART data for the period between 2008 and 2010 for latitudes greater than 65°

over ocean, stratifying by cloud top temperature in bins of 2° between -12 and 6°C. The results are categorized according to bins in temperature, altitude and LWP, and LTS and SH stratified. The number of grid-cells used to calculate each $\mathrm{ACI^{net}}$ parameter per bin ranges from 100 to 3300. The ACI^{net} parameter is almost always positive but sometimes close to zero. $\mathrm{ACI}_{r_e}^{net}$ ranges from 0 for graybody clouds between 1000 to 2000 m altitude with a cloud top temperature between -6 and -4 °C, to 0.34 for blackbody clouds between 1000 and 2000 m altitude with a cloud top temperature between 4 and 6°C. $\mathrm{ACI}_{\tau}^{net}$ ranges from -0.10 for all clouds between 200 and 1000 m altitude with a cloud top temperature of -11 °C, to 0.35 at 3°C for blackbody clouds between 1000 and 2000 m altitude. In general, $\mathrm{ACI}_{\tau}^{net}$ and $\mathrm{ACI}_{r_e}^{net}$ are of the same order of magnitude and the maximum values of $\mathrm{ACI^{net}}$ are found for clouds with temperatures above the freezing temperature.

We define the uncertainty in $\mathrm{ACI^{net}}$ as the 95 % confidence limit in the calculation of the slope of the linear fit. The uncertainty in the calculated values of $\mathrm{ACI}_{r_e}^{net}$ is generally less than 0.1, except for clouds with temperatures between 4 and 6 °C and between -12 and -10 °C, where the uncertainty bar is approximately 0.2. For the optical depth, the uncertainty is typically approximately 0.1, although larger values are observed for high and low cloud top temperatures.

For blackbody clouds between 1000 and 2000 m altitude, the average values of $\mathrm{ACI}_{\tau}^{net}$ and $\mathrm{ACI}_{r_e}^{net}$ equal 0.20 and 0.14 respectively. For cloud tops between 200 and 1000 m altitude, $\mathrm{ACI}_{\tau}^{net}$ and $\mathrm{ACI}_{r_e}^{net}$ equal 0.14. For graybody clouds between 1000 and 2000 m, $\mathrm{ACI}_{\tau}^{net}$ and $\mathrm{ACI}_{r_e}^{net}$ equal 0.12 and 0.08 respectively. For cloud tops between 200 and 1000 m altitude, $\mathrm{ACI}_{\tau}^{net}$ and $\mathrm{ACI}_{r_e}^{net}$ equals 0.14 and 0.12 respectively. Thus, the value of ACI^{net} appears to be fairly robust to altitude and cloud thickness and to whether r_e or τ is considered. Table 4.3 presents the average $\mathrm{ACI}_{\tau}^{net}$ and $\mathrm{ACI}_{r_e}^{net}$. For all cases, ACI^{net} values are near 0.13 ± 0.03.

4.4.2 Dependence of ACI^{net} on pollution concentration, specific humidity, and lower tropospheric stability

In what follows, we examine the influence of LTS, SH, and pollution concentration on $\mathrm{ACI^{net}}$. Table 4.4 shows values of $\mathrm{ACI}_{r_e}^{net}$ and $\mathrm{ACI}_{\tau}^{net}$ for graybody and blackbody clouds, and for $\chi_{\mathrm{CO}} < 5.5\,ppbv$ and $\chi_{\mathrm{CO}} > 10.0\,ppbv$, corresponding respectively to the lower and upper quartile of CO tracer concentration, and for a range in LTS and SH. For graybody

and blackbody clouds, $\mathrm{ACI}_{\tau}^{net}$ and $\mathrm{ACI}_{r_e}^{net}$ are highest for low values of χ_{CO}. The difference in ACI^{net} values between low and high polluted environments is slightly greater for $\mathrm{ACI}_{r_e}^{net}$ than for $\mathrm{ACI}_{\tau}^{net}$. Table 4.4 suggests that cloud effective radius and cloud optical depth are most sensitive to pollution when pollution concentrations are low. Previous studies have hypothesized that the effect of CCN on cloud microphysical properties saturates when cloud-droplet concentrations are high (Breon et al. 2002; Andersen and Cermak 2015). This effect does not explain the differences presented in Table 4.4 because Eq. (4.2) and Eq. (4.3) already take into account the potential for linear saturation by considering the logarithms of χ_{CO} and cloud parameters.

We now present the sensitivity of the ACI^{net} parameter to 5 different ranges of meteorological parameters delimited by the percentiles values presented in Table 4.5. We do not stratify the data according to LWP. Figures 4.4 and 4.5 show the influence of pollution loading on the cloud-droplet effective radius and cloud optical depth for each of the different SH and LTS regimes. Figure 4.4 presents the ACI^{net} parameter with respect to the cloud optical depth and cloud-droplet effective radius as a function of the SH, stratifying the data by LTS according to the method described in Section 3.3. Figure 4.5 is the same as Figure 4.4 except that it shows ACI^{net} as a function of LTS for a range of SH.

Figure 4.4 shows that $\mathrm{ACI}_{r_e}^{net}$ and $\mathrm{ACI}_{\tau}^{net}$ tend to increase with the SH independent of LTS. The ACI^{net} parameter is close to zero, or negative, for low values of SH. It increases rapidly with SH, saturating at a maximum value of about $2.5\,\mathrm{g\,kg^{-1}}$. We note that cloud top temperature and SH are weakly correlated. The correlation coefficient (r^2) of the linear regression of the two parameters is 0.20. The same applies for the SH and the LWP. The correlation coefficient of the two parameters is 0.05.

$\mathrm{ACI}_{r_e}^{net}$ increases with LTS from 0.02 for values of LTS ranging between 2.1 and 14 K to 0.09 for values of LTS between 23 and 38 K. The $\mathrm{ACI}_{\tau}^{net}$ dependence on LTS is larger: $\mathrm{ACI}_{\tau}^{net}$ equals 0.10 for LTS values between 2.1 and 14 K and it equals 0.32 for LTS values between 21 and 38 K.

4.5 Discussion

The results presented here show values of the ACI^{net} parameter with respect to the cloud-droplet effective radius and optical depth, for clouds over oceans north of 65° lying

between 200 and 2000 m, and for the years between 2008 to 2010. We find $\mathrm{ACI}^{\mathrm{net}}$ values that range from 0.00 to 0.34 for the cloud-droplet effective radius, and from -0.10 to 0.35 for the optical depth.

Prior studies examining the Arctic region have retrieved ACI values ranging from -0.10 to 0.40 (Garrett et al. 2004; Lihavainen et al. 2009; Zhao et al. 2012; Sporre et al. 2012). Tietze et al. (2011) calculated $\mathrm{ACI}^{\mathrm{net}}$ values ranging from 0.00 to 0.17 using a similar satellite-FLEXPART colocation method. What differs in this study is that we examine solely anthropogenic pollution, and that we extend the dataset from one to three years, stratifying the dataset according to SH and LTS. The larger $\mathrm{ACI}^{\mathrm{net}}$ values we find in this study suggest a higher sensitivity of cloud microphysical properties to pollution plumes from distant sources than was found by Tietze et al. (2011).

However, Tietze et al. (2011) also found values of $\mathrm{ACI}_{\tau}^{net}$ that were greater than $\mathrm{ACI}_{r_{\mathrm{e}}}^{net}$, by a factor of four, and they attributed this difference to unknown dynamic or precipitation feedback that makes $\mathrm{ACI}_{\mathrm{LWP}}^{net}$ greater than zero (Eq. (4.5)). In contrast, our results show that the $\mathrm{ACI}_{r_{\mathrm{e}}}^{net}$ and $\mathrm{ACI}_{\tau}^{net}$ parameters are more similar, suggesting no such feedback. Table 4.6 compares the differences between $\mathrm{ACI}_{\tau}^{net}$ and $\mathrm{ACI}_{r_{\mathrm{e}}}^{net}$ that are presented in Table 4.3, along with their corresponding values when no control is made for SH and LTS. The difference between $\mathrm{ACI}_{r_{\mathrm{e}}}^{net}$ and $\mathrm{ACI}_{\tau}^{net}$ is largest when meteorological parameters are not controlled for. For all clouds considered, the maximum difference increases from 0.04 when the data are considered within narrow meteorological bands to 0.12 when the data are not. This result is important since it suggests that the hypothesized feedback discussed by Tietze et al. (2011) may have in fact been due to the natural sensitivity of clouds to local meteorology. Not controlling sufficiently for meteorology may lead to artifacts that exaggerate the magnitude of the aerosol indirect effect.

In contrast to most prior efforts, satellite-retrieved cloud properties are not compared to CCN or aerosol concentrations but rather to pollution concentrations — specifically CO simulated from a tracer transport model. CO serves as a proxy for CCN close to pollution sources although far from sources CCN and CO can become decoupled due to scavenging en route to distant clouds. The comparison we present through the $\mathrm{ACI}^{\mathrm{net}}$ parameter implicitly accounts for this possibility. For temperatures below $-6\,^{\circ}\mathrm{C}$, low values of $\mathrm{ACI}^{\mathrm{net}}$ are observed. Tietze et al. (2011) hypothesized that at such temperatures,

cloud supersaturations may be too small to activate aerosols as CCN or that clouds with lower temperatures have followed longer transport pathways nearer the surface (Stohl 2006) and therefore had greater exposure to dry deposition.

Table 4.4 suggests that ACI^{net} values are lowest when pollution concentrations are high. Figure 4.6 presents the normalized distribution of potential temperature for polluted and pristine clouds, defined as the upper and lower quartile, for graybody clouds. We present results for graybody clouds because the ACI^{net} differences between polluted and clean cases are largest; results for blackbody and all clouds are not shown here, but have similar results regarding the potential temperature distribution.

Highly polluted air parcels are associated with potential temperatures around 280 K whereas pristine air parcels have a lower potential temperature – around 272 K. We hypothesize that higher values of potential temperature suggest pollution sources from further south, so wet scavenging is more likely to occur during transport and this decreases the correlation between a CO tracer and CCN, therefore lowering the ACI^{net} parameter. Also, polluted air parcels and aerosols do not necessarily have the same physical and chemical properties at lower and higher latitudes, and this difference may impact the influence of aerosols on cloud microphysics and aerosols (Bilde and Svenningsson 2004; Dusek et al. 2006; Ervens et al. 2007; Andreae and Rosenfeld 2008).

In general, we observe that when moisture increases, the cloud sensitivity to pollution increases. From model simulation of stratocumulus, Ackerman et al. (2004) found that when the relative humidity (RH) above the cloud top is high, cloud LWP increases with N_c consistent with theoretical arguments (Albrecht 1989; Pincus and Baker 1994), but that when the RH is low, the LWP decreases when N_c increases, as supported by some observations (Coakley and Walsh 2002). The difference was attributed to the consequence of dry air into a cloud layer. Humidity inversions are common above low-level cloud tops in the Arctic (Nygärd et al. 2014), so similar phenomena may be playing a role.

Studies of the indirect effect at midlatitudes suggest that values of ACI are highest under unstable conditions (Chen et al. 2014; Andersen and Cermak 2015). Our results from the Arctic show the reverse, that conditions of high LTS are associated with higher values of ACI^{net}. Klein and Hartmann (1993) showed that, in general, higher values of LTS lead to greater stratiform cloudiness, except in the Arctic where radiative cooling prevails

over convection as the driving mechanism for cloud formation. This result is similar to results found by Kim et al. (2008) who found that aerosol-cloud interactions are strongest in clouds with adiabatic liquid water content profiles. Such clouds might be expected more frequently when LTS is high and there is reduced vertical mixing.

Finally, we find $\mathrm{ACI}_{\tau}^{net}$ is more sensitive to changes in LTS than $\mathrm{ACI}_{r_\mathrm{e}}^{net}$. A consequence is that for values of LTS greater than 23 K, $\mathrm{ACI}_{\tau}^{net}$ and $\mathrm{ACI}_{r_\mathrm{e}}^{net}$ differ by about 0.20. In a stable atmosphere with high LTS it appears that $\mathrm{ACI}_{\mathrm{LWP}}^{net}$ increases more strongly in response to aerosols than in unstable environments (Klein and Hartmann 1993; Qiu et al. 2015).

Our study has been focused on low-level arctic clouds in order to simplify interpretations and allow comparison with other studies (Garrett et al. 2004; Garrett and Zhao 2006; Lubin and Vogelmann 2006; Mauritsen et al. 2011). Precipitation is more likely to occur for air parcels lifted in higher altitude (Law et al. 2014), decreasing the ACI^{net}. Nevertheless, if meteorological parameters are sufficiently constrained, we could extend the present results to higher altitude clouds.

4.6 Conclusion

Satellite, numerical tracer transport model, and meteorological reanalysis data sets from 2008 to 2010 are used here to calculate the sensitivity of cloud-droplet effective radius and optical depth in the Arctic to anthropogenic pollution transported from midlatitudes. We focused on latitudes north of 65° for a period between March 2008 and October 2010. Using ECMWF reanalysis data, we stratified the dataset according to temperature, LTS, SH, altitude, and LWP. We find that the sensitivity of cloud properties to pollution, as quantified by values of $\mathrm{ACI}^{\mathrm{net}}$, lies close to a theoretical maximum value of $1/3$, assuming that a simulated CO tracer correlates well with CCN. Further, $\mathrm{ACI}_{r_\mathrm{e}}^{net}$ and $\mathrm{ACI}_{\tau}^{net}$ seem to increase with SH and LTS, highlighting that meteorological parameters have an important impact on aerosol-cloud interactions.

Globally, Klimont et al. (2013) have estimated that there was a drop of about 9281 Gg in anthropogenic sulphur dioxide emissions between 2005 and 2010 due to a reduction in European and American emissions and a flue gas desulfurization program on power plants in China. This reduction in emissions has led to a decrease of sulfate concentrations at Arctic surface station (Hirdman et al. 2010). In the Arctic, the effect of a decrease in midlatitude

pollution emissions may some day be offset by greater levels of Arctic industrialization (Lindholt and Glomsrød 2012) and shipping (Pizzolato et al. 2014; Miller and Ruiz 2014) that introduce new local aerosol sources. Further, an increase in the extent of open ocean due to sea-ice retreat may be expected to lead to an increase in the atmospheric humidity (Boisvert and Stroeve 2015) and from the results presented here, a higher sensitivity of clouds to aerosols. However, this study also suggests that any associated decrease in LTS could partially counteract this effect.

Climate warming is thought to stimulate boreal forest fires (Westerling et al. 2006). The impact of pollution from biomass burning has not been included in the present research. Given biomass-burning aerosol can act as efficient ice nuclei (Markus et al. 2009), the analyses presented here might be extended to explore aerosol-induced changes in cloud thermodynamic phases.

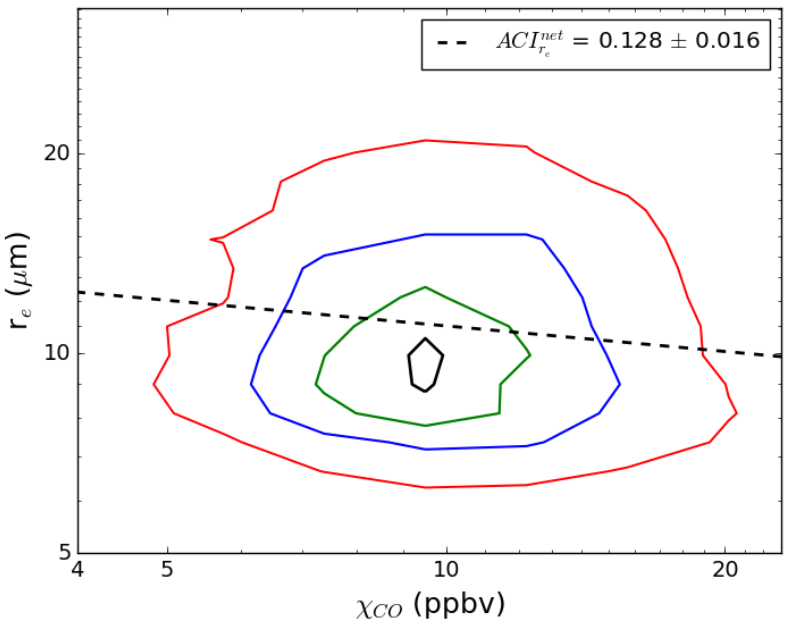

Figure 4.1: Calculation of the $ACI_{r_e}^{net}$ parameter from a probability distribution of values in the effective radius and CO tracer concentration for liquid clouds with cloud top altitudes between 1000 m and 2000 m, and cloud top temperatures between −12 and 6.0 °C. The color scale indicates higher density of values in linear intervals. The $ACI_{r_e}^{net}$ number indicates the negative slope of the linear fit (dashed line).

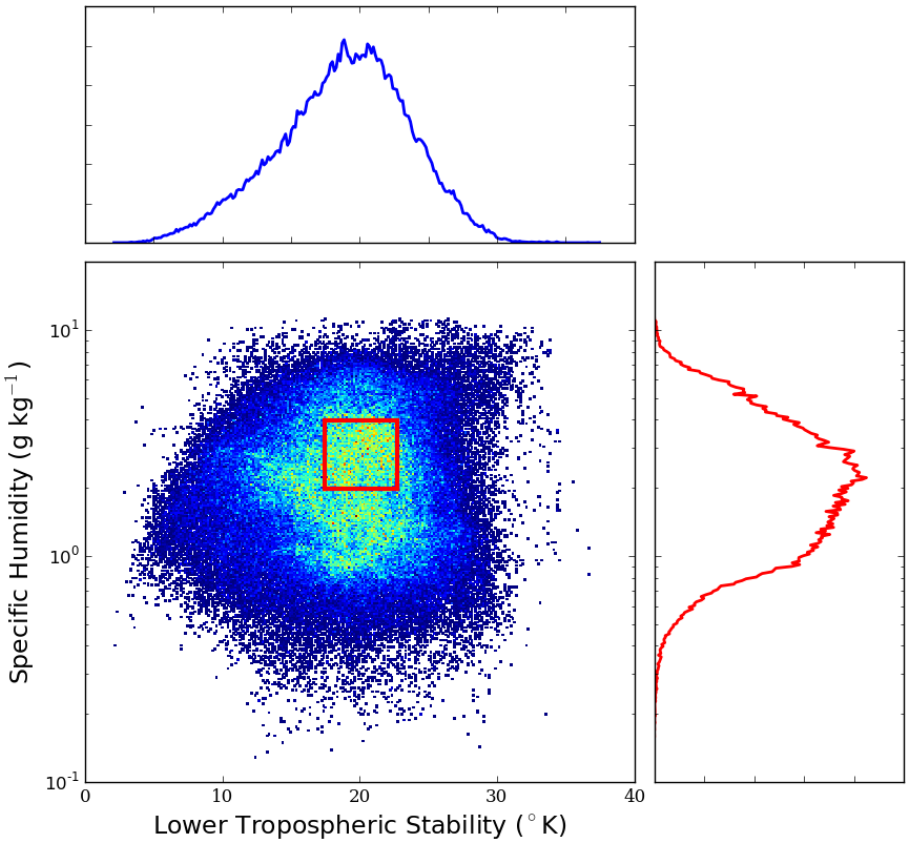

Figure 4.2: 2-D histogram of the SH and the LTS retrieved by ECMWF reanalysis from 2008 to 2010. The red rectangle corresponds to the range where there is a maximum of measurements within a bin corresponding to 15 % of the total range length of the corresponding parameter.

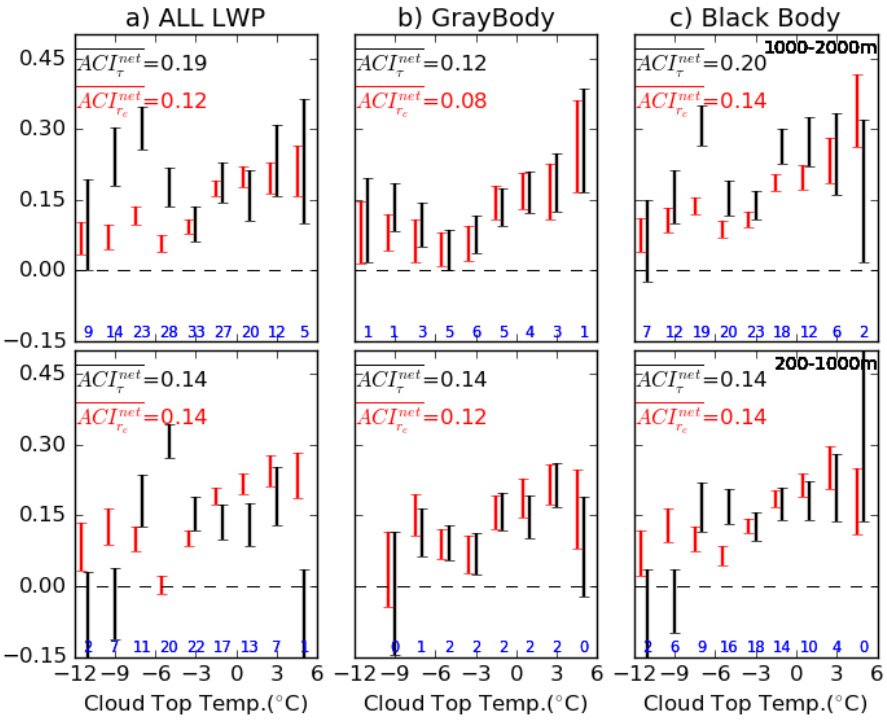

Figure 4.3: ACI^{net} for different values of cloud top temperature, LWP, and cloud altitude. ACI^{net} parameter of the effective radius (r_e) (red) and optical depth (τ) (black), as a function of temperature calculated for liquid clouds between 200–1000 m (lower row) and 1000–2000 m (upper row). The bars indicate the 95 % confidence limit in the calculation of the mean ACI^{net} value. Each column corresponds to different thresholds for LWP (blackbody: LWP $> 40\,g\,m^{-2}$, graybody: LWP $< 40\,g\,m^{-2}$). Blue numbers indicate the number of grid-cells, in hundreds, that are used to calculate each ACI^{net} value. In each figure the ACI^{net} value averaged over the temperature and weighted according the inverse of the uncertainty is indicated.

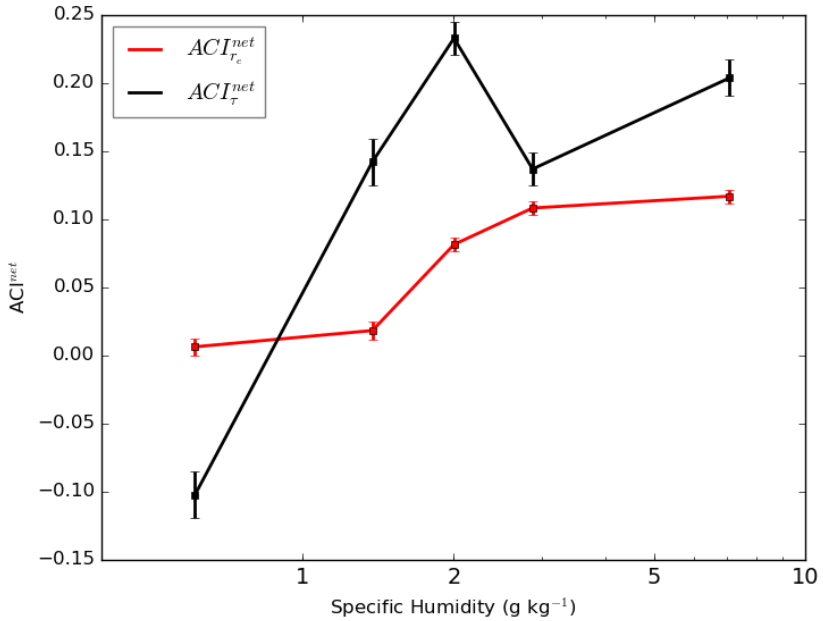

Figure 4.4: $\mathrm{ACI}^{net}_{r_e}$ (red) and $\mathrm{ACI}^{net}_{\tau}$ (black) for different bins of the SH, stratified by LTS between 17 and 22 K. Each marker is placed in the middle of the corresponding bin.

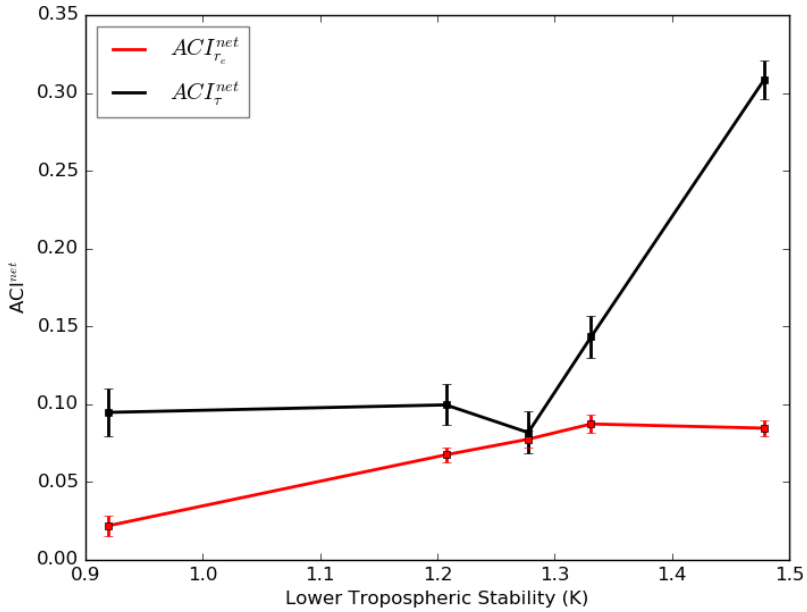

Figure 4.5: $\mathrm{ACI}^{\mathrm{net}}_{\mathrm{r_e}}$ (red) and $\mathrm{ACI}^{net}_{\tau}$ (black) and $\mathrm{ACI}^{net}_{\tau}$ as a function of the lower tropospheric stability, stratified by SH between 2.0 and 4.0 g kg^{-1}.

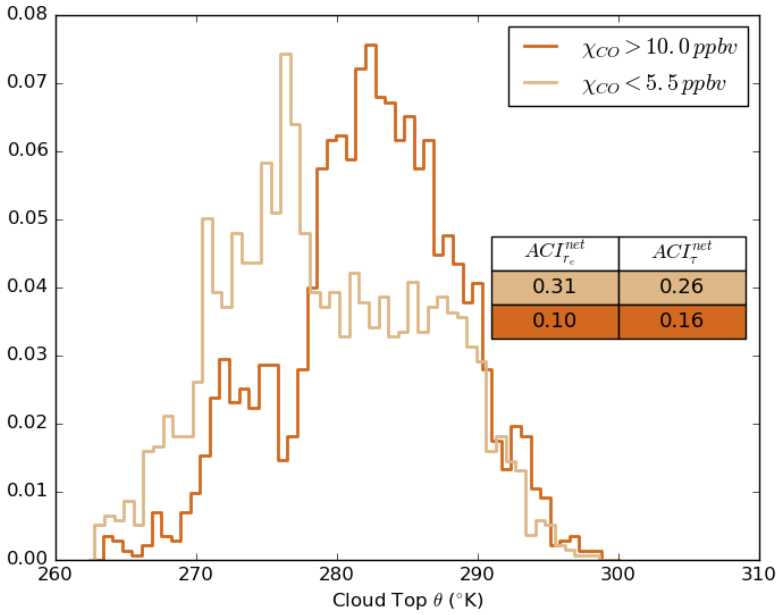

Figure 4.6: Normalized distribution of the cloud top potential temperature when clouds are associated with CO tracer concentrations (χ_{CO}) greater than 10 ppbv and less than 5 ppbv. The values of $ACI_{r_e}^{net}$ and ACI_{τ}^{net} associated with each histogram are presented also in Table 4.3.

Table 4.1: Cloud products, pollution tracer, atmospheric reanalysis used in this study with the corresponding spatial and temporal resolution.

Parameter(s)	From:	Resolution(s)
Cloud parameter (T, r_e, τ)	MODIS, POLDER-3	Spatial resolution: 36 km^2
CO tracer concentration from anthropogenic sources	FLEXPART	Spatial resolution: $1^\circ \times 2^\circ$, Temporal resolution: 3 h
Specific humidity, temperature profile	ERA-I (ECMWF)	Spatial resolution: $1.5^\circ \times 1.5^\circ$, Temporal resolution: 6 h

Table 4.2: Summary of the different ranges of the logarithm of the SH and the LTS over the region of interest, detailing the method used to determine the final range of parameters considered. The Δ defines the difference between the maximum and the minimum of the total range. The considered range is chosen to keep the maximum number of measurements within a fixed interval of 15 % of the range, corresponding to the red square on Figure 4.2.

	$\log_{10}$ (Specific Humidity)	LTS ($^\circ$)
Total Range [Min, Max]	$[-0.89, 1.0]$	[2.1, 38]
Δ Total Range	1.9	36
15 % Interval	0.28	5.4
Stratified Range [Min, Max]	[0.30, 0.60] = [2.0, 4.0] (g kg^{-1})	[17, 22]

Table 4.3: ACI$^{\text{net}}$ parameter calculated for the optical depth and the effective radius considering all clouds, graybody clouds, and blackbody clouds, averaged from values presented in Figure 4.3 and weighted considering the inverse of the uncertainty in the mean..

	All LWP	Graybody	Blackbody
$\text{ACI}_{r_e}^{net}$	0.12	0.10	0.14
ACI_{τ}^{net}	0.16	0.13	0.17

Table 4.4: ACI^{net} parameter calculated for the optical depth and the effective radius considering all clouds, graybody clouds, and blackbody clouds, for two different regimes of CO concentration representing lower and upper quartiles of CO concentration.

	All LWP		Graybody		Blackbody	
	$ACI^{net}_{r_e}$	ACI^{net}_{τ}	$ACI^{net}_{r_e}$	ACI^{net}_{τ}	$ACI^{net}_{r_e}$	ACI^{net}_{τ}
$\chi_{CO} < 5.5\,ppbv$	0.23	0.36	0.31	0.26	0.28	0.24
$\chi_{CO} > 10\,ppbv$	0.09	0.35	0.09	0.16	0.14	0.16

Table 4.5: Percentile values of SH and LTS used to define different regimes of the meteorological parameters.

	Specific Humidity ($g\,kg^{-1}$)	LTS (K)
Minimum	0.13	2.1
20th percentile	1.2	14
40th percentile	1.7	18
60th percentile	2.4	20
80th percentile	3.6	23
Maximum	11	37

Table 4.6: Difference between ACI^{net}_{τ} and $ACI^{net}_{r_e}$ (i.e., ACI^{net}_{LWP}) for graybody, blackbody, and all clouds when lower tropospheric stability and SH are stratified and when they are not stratified. The averaged ACI^{net} values are shown in Table 4.3.

	All LWP	Graybody	Blackbody
Stratified	0.04	0.03	0.04
Not Stratified	0.12	0.04	0.08

CHAPTER 5

IMPACT OF ANTHROPOGENIC AND BIOMASS BURNING PLUMES ON ARCTIC CLOUDS

The rate of warming in the Arctic (Richter-Menge and Jeffries 2011) depends upon the response of low-level cloud microphysical and radiative properties to high concentrations of cloud condensation nuclei (CCN) advected from midlatitude sources (Garrett and Zhao 2006; Tietze et al. 2011; Zhao and Garrett 2015; Coopman et al. 2016; Zamora et al. 2015). Cloud droplet absorption and the scattering radiative cross-section increase with higher concentrations of cloud condensation nuclei (CCN) from distant anthropogenic (ANT) and biomass-burning (BB) pollution sources (Tietze et al. 2011; Shupe et al. 2013; Coopman et al. 2016; Zamora et al. 2015). The challenge in assessing the magnitude of the effect has been to decouple aerosol impacts from how clouds change solely due to natural meteorological variability (Stevens and Feingold 2009; Coopman et al. 2016; Gryspeerdt et al. 2016). Here we address this issue by using a large, multiyear satellite, meteorology, and tracer transport model dataset to show that the response of arctic clouds to anthropogenic aerosols lies close to a theoretical maximum (McComiskey et al. 2009) and is two to eight times higher than observed elsewhere globally (Nakajima et al. 2001; Quaas et al. 2005). However, a previously described response of cloud radiative properties to BB plumes (Tietze et al. 2011; Lance et al. 2011; Zamora et al. 2015) appears to be overstated as the interactions are infrequent and cloud modification appears better explained by coincident changes in temperature, humidity and atmospheric stability.

5.1 Introduction

While the Arctic remains remote from industrialized regions, air originating from midlatitudes can be loaded with biomass-burning (BB) and anthropogenic (ANT) aerosols (Shaw 1982; Quinn et al. 2007b; Fisher et al. 2010; Warneke et al. 2010). Aerosols can act

as CCN, that make cloud droplets smaller and more numerous, thereby leading to clouds that are more efficient at emitting longwave and reflecting shortwave radiation, especially effective in the arctic region and always underestimated in former studies (Shindell et al. 2013).

Arctic cloud formation is favored by high humidity (Cox et al. 2015). Unlike at mid-latitudes, Klein and Hartmann (1993) have shown that arctic stratus formation is favored by low LTS. Clouds with higher temperatures (T_C) tend to be more turbulent with greater available moisture, hence they have higher water contents, larger droplets, and are more likely to precipitate. Our study aims to robustly evaluate how ANT and BB aerosol sources affect clouds over the entirety of the Arctic independent of local thermodynamic considerations (Stevens and Feingold 2009; Gryspeerdt et al. 2016). To do this, we use space based data sets for the retrieval of cloud properties, and quantify the magnitude of aerosol-cloud interactions (ACI) by comparing cloud properties with pollution concentrations. The ACI parameter has previously been introduced as the ratio of relative changes in cloud optical depth τ and cloud droplet effective radius r_e to relative changes in CCN concentrations. The theoretical maximum value of ACI is 0.33 assuming a one to one correspondence between CCN and droplet number concentration and a fixed cloud liquid water path (LWP) (McComiskey et al. 2009).

5.2 ACI^{net} parameter

Retrieving aerosol concentrations and cloud properties at the same location is impossible from space, so we take a slightly different approach. Here, we derive values of a net ACI (ACI^{net}) parameter from ensembles of retrieved cloud properties and temporally, vertically, and horizontally colocated concentrations of a pollution tracer carbon monoxide χ_{CO}, where CO is set as a purely passive, chemically nonreactive species within a chemical transport model (Coopman et al. 2016).

$$ACI_{r_e}^{net} = -\frac{d \ln r_e}{d\, ln \chi_{CO}} \tag{5.1}$$

$$ACI_{\tau}^{net} = \frac{d \ln \tau}{d \ln \chi_{CO}}. \tag{5.2}$$

CO by itself does not interact with clouds, of course, but its utility for studies of aerosol-cloud interactions is that it serves as an indicator of the presence of polluted air that may

be loaded with aerosols (Garrett et al. 2006). Both CCN and a passive CO tracer are highly correlated close to combustion sources (Longley et al. 2005) and they are equally diluted along transport pathways, so the spatial and temporal distributions of the two pollutants should generally be expected to correlate. Then, ACI^{net} provides a measure of the local sensitivity of clouds to pollution from distant sources (Coopman et al. 2016). The theoretical maximum value of ACI^{net} assuming that CO and CCN are perfectly correlated and LWP is fixed remains 0.33.

5.3 Data used

Distributions of χ_{CO} are obtained from the numerical tracer transport model GEOS-Chem v. 9-01-03. We vertically and horizontally colocate χ_{CO} distributions with low-level liquid cloud microphysical properties and cloud top temperature (T_C) obtained using the MODIS (MODerate-resolution Imaging Spectroradiometer) and POLDER-3 (POLarization and Directionality of the Earth's Reflectance) sensors for a period between March and September from 2005 to 2010. ERA-Interim reanalysis meteorological datasets are co-located with satellite and numerical simulation datasets. In the reanalysis, we use specific humidity (SH) at 700 hPa as a proxy of lower-atmosphere humidity and LTS is defined as the difference in potential temperature between 700 hPa and 1000 hPa (Klein and Hartmann 1993).

5.4 Case study of 31 July 2010

To illustrate why large datasets can be more useful than individual case studies for assessing the magnitude of ACI^{net}, Figure 5.1 shows a BB event on 31 July 2010 at 2130 UTC where a biomass burning plume from northeastern Siberia with high SH and high χ_{CO} was advected to the Beaufort Sea region. From the shapes and locations of the 4 g kg^{-1} SH and the 100 ppb χ_{CO} isolines it is clear that the two covary. Clouds were also present in the polluted tongue, so the implication is that any observed change in cloud τ could mistakenly be attributed to higher pollution levels when they are more reasonably explained by increased moisture.

5.5 Results and discussion

Table 5.1 shows that BB and ANT plumes represent, respectively, 0.4% and 37% of the cloudy dataset. A possible reason BB grid cells are relatively few is that BB events tend to occur when temperatures are high, condition that is generally unfavorable for cloud formation (Monks et al. 2012). Moreover, BB aerosol regimes have median values of SH, LTS, and T_C that are, respectively, 5.1 g kg^{-1}, 23.8 K, and 0.4°C, whereas ANT regimes have median values of 1.9 g kg^{-1}, 17.7 K, and -8.4°C. For comparison, the entire dataset has median values of 2.6 g kg^{-1}, 18.7 K, and -4.4°C. Therefore, cloudy air dominated by BB aerosols tends to be warmer, moister, and more stable than typical air parcels dominated by ANT aerosol regimes.

Sorting the data according to polluted and clean aerosol regimes defined by the upper and lower quartiles in χ_{CO}, Figure 5.2 shows that polluted BB aerosol regimes are associated with higher LTS, SH, and T_C than clean BB aerosol regimes while the opposite is observed for ANT aerosol regimes. Clean and polluted regimes are respectively defined as the lower and upper quartile in CO concentration. Levene statistical tests applied to SH, LTS, and T_C indicate that to within a 95% confidence interval, clean and polluted air parcels dominated by both ANT and BB aerosol regimes are characterized by different meteorological states (Levene values > 30 in each case). Distributions of meteorological parameters within BB and ANT plumes differ because the plumes tend to occur during different weather conditions. The bottom quartile of χ_{CO}(BB) is 155 ppb whereas the bottom quartile of χ_{CO}(ANT) is 54 ppb.

In order to examine the sensitivity of clouds to aerosol concentrations independently of this meteorological variability, we limit the dataset to a narrow range of meteorological conditions that covers a representative range of T_C, LTS, and SH for both ANT and BB polluted plumes. We limit the dataset to a temperature range between T_C(BB) - $\sigma_{T_C(BB)}$ and T_C(ANT) + $\sigma_{T_C(ANT)}$ where T_C(BB) and T_C(ANT) represent the median value of T_C associated with BB and ANT plumes and $\sigma_{T_C(BB)}$ and $\sigma_{T_C(ANT)}$ the associated standard deviations. The dataset is also controlled for both SH and LTS, the ranges cover 15% of the span of LTS and SH, centered at the respective mode of each of their distributions. This limits the analysis to 1,980,186 grid cells or 20% of the total dataset lying within a range between -7.8°C and 4.8°C for T_C, between 16.5 K and 21.8 K for LTS, and between

$2.0\,\mathrm{g\,kg^{-1}}$ and $4.0\,\mathrm{g\,kg^{-1}}$ for SH. With the dataset constrained in this manner, the correlation coefficient of χ_{CO} to meteorological conditions drops from -0.18 to -0.03 for LTS, from 0.28 to 0.09 for SH, and from 0.39 to 0.17 for T_C. Aerosol-cloud interactions are normally evaluated within a narrow range of liquid water path (LWP) since $r_e \propto \tau/\mathrm{LWP}$ so we further stratify the dataset into four LWP bins between $44\,\mathrm{g\,m^{-2}}$ and $96\,\mathrm{g\,m^{-2}}$.

Figure 5.3 shows values of $\mathrm{ACI}^{\mathrm{net}}_{r_e}$ in each of the four LWP bins as a function of the relative fraction of BB pollution to total pollution $\chi_{CO}(BB)/\chi_{CO}(Tot)$ and whether the dataset is controlled for meteorological variability. Regarding the relative fraction of BB pollution to total pollution, we divide the data into five quintiles: a fraction below 0.2 nominally identifies ANT dominated aerosol regimes whereas a ratio greater than 0.8 indicates a BB dominated aerosol regime. Controlling for each of LTS, SH, LWP, and T_C, the number of cloudy grid cells in each LWP bin lies between 331 and 565 for BB plumes (1,777 grid cells total) and between 40,705 and 47,610 for ANT plumes (175,316 grid cells total). The difference between $\mathrm{ACI}^{\mathrm{net}}_{r_e}$ and $\mathrm{ACI}^{\mathrm{net}}_{\tau}$ is shown when the two quantities are statistically different.

In general, $\mathrm{ACI}^{\mathrm{net}}_{r_e}$ and $\mathrm{ACI}^{\mathrm{net}}_{\tau}$ are similar; differences are statistically significant but do not exceed 12% when there is no control for meteorological parameters. When no control is made for meteorological covariance, $\mathrm{ACI}^{\mathrm{net}}$ is positive for both BB and ANT dominated aerosol regimes, although values of $\mathrm{ACI}^{\mathrm{net}}$ in BB aerosol regimes are generally lower by approximately 60%.

However, when the dataset is limited to the narrow meteorological range previously described, $\mathrm{ACI}^{\mathrm{net}}$ associated with ANT aerosol regimes increases and is close to the 0.33 theoretical maximum but $\mathrm{ACI}^{\mathrm{net}}$ for BB aerosol regimes drops to near zero. Here, based on an analysis of 175,316 grid cells, $\mathrm{ACI}^{\mathrm{net}}_{r_e}$ values in ANT aerosol regimes range from 0.23 to 0.30 with probability values or the correlation (p-values) lower than 0.05 (not shown). On the other hand, from an analysis of 1,777 grid cells in BB aerosol regimes, values of $\mathrm{ACI}^{\mathrm{net}}_{r_e}$ range from -0.10 to 0.10 with p-values greater than 0.1. No statistically significant relationship between BB aerosols and cloud properties is observed and a previously observed correlation between χ_{CO}(BB) and cloud microphysical parameters (Zamora et al. 2015; Tietze et al. 2011; Lance et al. 2011) is better explained by a correlation with meteorology. In fact, the Pearson correlation coefficients between χ_{CO} in BB dominated regimes and LTS

(0.19), SH (0.31), and T_C (0.25) are higher than the correlation coefficient between χ_{CO} and τ (0.17). The correlation of τ with SH (0.25) is particularly high.

A limitation of our method is that it cannot explain why there is a higher sensitivity of clouds to ANT aerosol plumes than to BB plumes. It may be that pyrogenic aerosols are not particularly effective CCN (Andreae and Rosenfeld 2008) at the low supersaturations that might be expected for stable arctic stratus (Earle et al. 2011). Or, given that concentrations of CO within BB plumes tend to correlate with moisture, BB aerosols may be particularly subject to removal by wet scavenging (Di Pierro et al. 2013). Another explanation is that BB plumes are more subject to high-altitude transportation (Fromm 2005; Brock et al. 2011) and therefore more subject to removal processes (Law et al. 2014). In any case, as shown by Table 5.1, interactions between BB plumes and clouds tend to be rare.

5.6 Conclusion

Only very few satellite studies have looked at aerosol cloud interactions controlling for meteorological parameters (Chen et al. 2014; Andersen and Cermak 2015) and even fewer in the Arctic. In terms of combined spatial and temporal coverage, and the constraints for meteorological variability, this study is the most comprehensive study to date of aerosol-cloud interactions in the Arctic (Garrett et al. 2004; Zamora et al. 2015). Compared to satellite observations of ACI values between 0.04 and 0.17 for subpolar regions (Nakajima et al. 2001; Quaas et al. 2005), ACI in the Arctic is two to seven times higher. The arctic atmosphere is characterized by high LTS and adiabatic clouds. Unlike midlatitude regions — where mixing processes decrease cloud sensitivity to aerosols (Kim et al. 2008) — the Arctic is less influenced by dry-air entrainment and is characterized by a stable atmosphere where cloud microphysical changes are mainly driven by aerosols.

In the present study we do not provide information on radiative impacts of changes in aerosol regimes. Nevertheless, to put our results into a wider context, direct effect of aerosol has been compared with indirect effect (Hegg et al. 1996; Haywood and Boucher 2000). The indirect effect is associated with a larger uncertainty than the direct effect but the indirect effect is potentially more important than the direct effect (Haywood and Boucher 2000) especially in the Arctic (Hegg et al. 1996).

The effect of aerosol-cloud interactions on surface temperatures in the Arctic is more

complicated than at midlatitudes because increasing τ can also lead to a higher longwave cloud emissivity (Garrett and Zhao 2006); either a significant net warming or cooling occurs depending on τ, the season, and sea-ice cover (Zhao and Garrett 2015). In the future, a combination of reductions in emissions of midlatitude pollutants and increased wet scavenging in a warmer climate is anticipated to reduce the arctic aerosol burden by 61.0% by the end of the century (Klimont et al. 2013). Based on the ACI values found here, this can be expected to correspond to an 18% decrease in τ, with any additional increase in τ due to increasing arctic maritime transportation and industrialization (Peters et al. 2011). However, the dynamic response of cloud amount to aerosols is itself a function of aerosols and meteorological conditions (Garrett et al. 2009; Chen et al. 2014) so how the high sensitivity of arctic clouds to aerosols will play out remains to be determined.

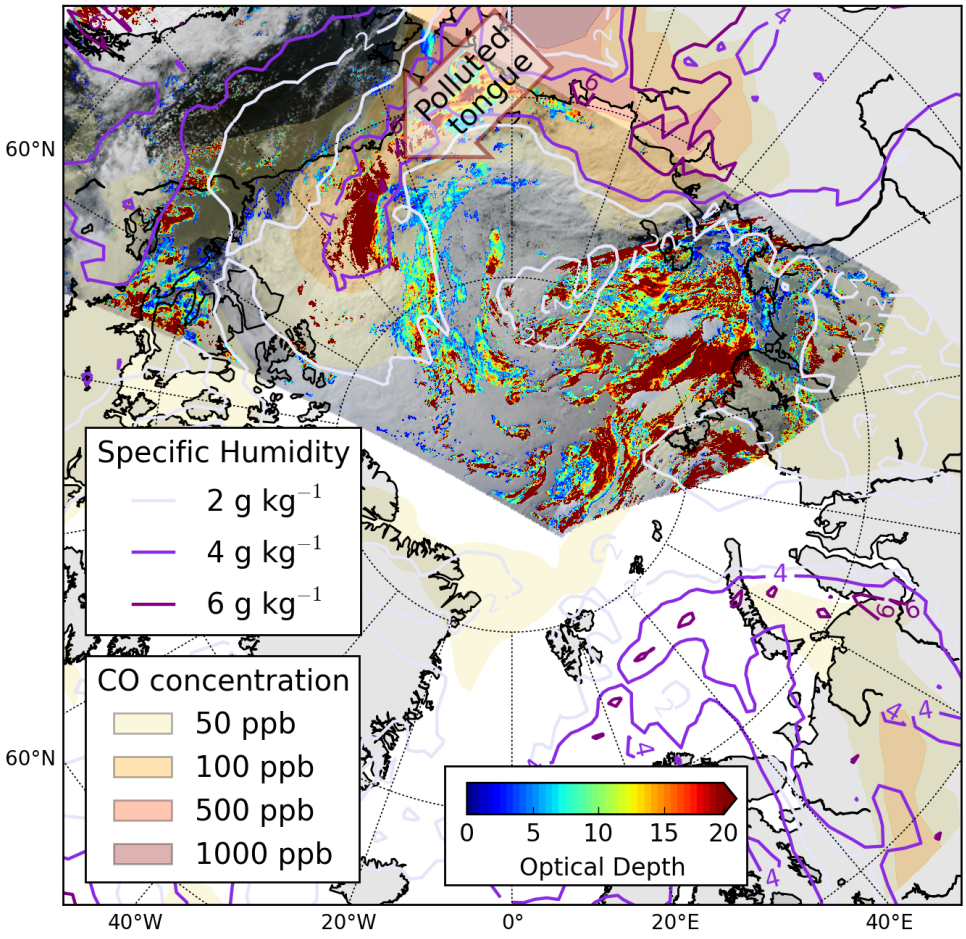

Figure 5.1: Low-level τ, SH at 700 hPa and χ_{CO} of the first 3 km on 31 July at 21:30 UTC. The SH and the χ_{CO} are respectively retrieved by ERA-Interim reanalysis, and GEOS-Chem and they are both showing by the contour plots. Values of τ are retrieved by the instrument Aqua on MODIS platform satellite.

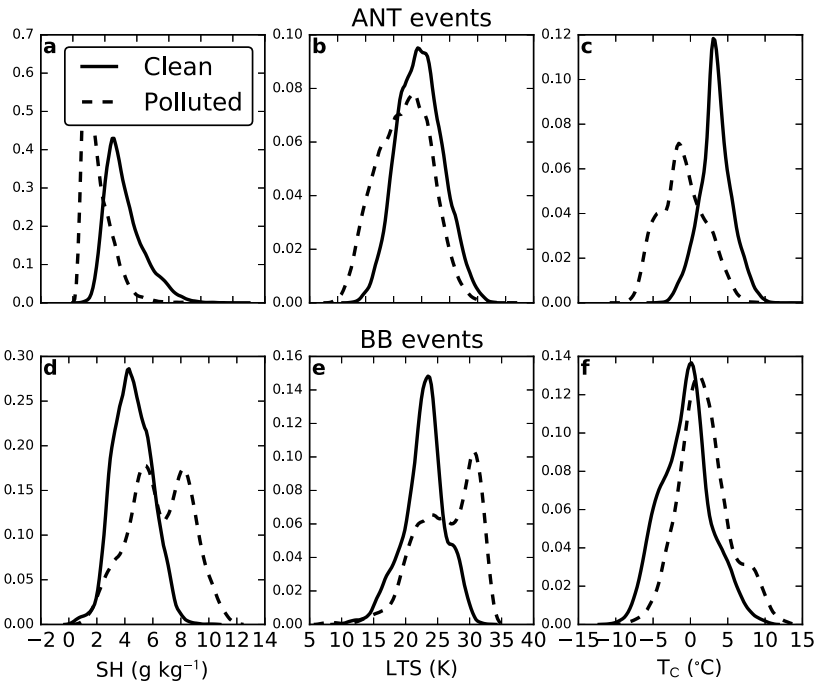

Figure 5.2: Normalized probability density function of meteorological parameters. Normalized probability density function of (a,d) SH, (b,e) LTS, and (c,f) T_C for clean and polluted air parcels during (a,b,c) ANT and (d,e,f) BB aerosol regimes. Clean and polluted BB air parcels corresponding to the lower and upper quartiles in CO concentration have values of χ_{CO} less than 155 ppb and greater than 262 ppb, respectively. Clean and polluted ANT air parcels have values of χ_{CO} less than 54 ppb and greater than 82 ppb.

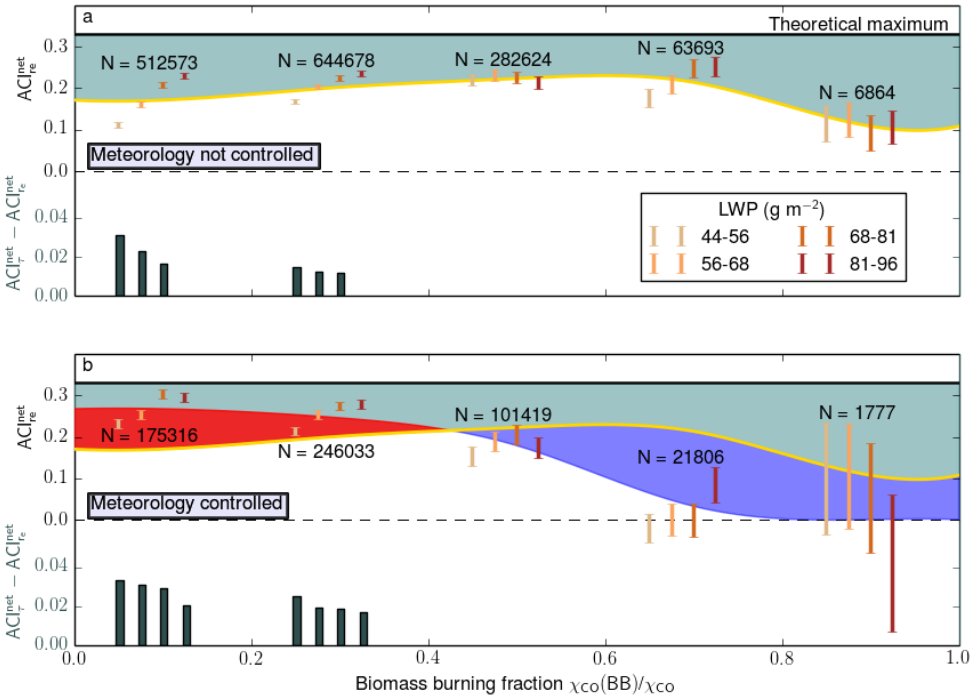

Figure 5.3: $ACI_{r_e}^{net}$ for different meterological states. $ACI_{r_e}^{net}$ (a) as function of biomass burning fraction $\chi_{CO}(BB)/\chi_{CO}$, LWP, and (b) whether the dataset is limited to a narrow range of LTS and SH with T_C between -7.8°C and 4.8°C. Error bars indicate 95% confidence ranges for the calculated value of ACI^{net}. N indicates the number of equal-area grid cells containing clouds that went into the calculation of the ACI^{net} parameter for the combined 4 LWP bins. ACI_{τ}^{net} - $ACI_{r_e}^{net}$ is shown only when the difference between the two values is statistically significant (Methods). The light blue area bounded by the yellow line represents the difference between the $ACI_{r_e}^{net}$ averaged over the 4 LWP bins and a theoretical maximum value of 0.33. Red and blue areas represent the calculated increase and decrease, respectively in $ACI_{r_e}^{net}$ that is due to controlling for meteorology.

Table 5.1: Meteorological parameters associated with ANT and BB aerosol regimes. Median values of the specific humidity (SH), the lower-tropospheric stability (LTS), and cloud-top temperature are associated with BB and ANT aerosol regimes and for all grid cells.

	ANT plumes	BB plumes	Entire dataset
SH ($g\,kg^{-1}$)	1.9	5.1	2.5
LTS (K)	17.7	23.8	18.7
T_C (°C)	-8.4	0.4	-4.4
Nb. of data point	3,777,125	37,732	10,119,668

CHAPTER 6

IMPACT OF ANTHROPOGENIC POLLUTION PLUMES ON THERMODYNAMIC PHASE TRANSITION

6.1 Introduction

The Arctic is sensitive to global warming, and an increase in surface temperature faster and more intense than in any other region in the world has been observed (Serreze et al. 2009; Sanderson et al. 2011). The warming intensification is due to feedback processes, such as the surface albedo through the sea-ice melting leading to the so-called ”arctic amplification” (Screen and Simmonds 2010). The arctic radiative balance is largely influenced by clouds (Curry et al. 1996; Garrett et al. 2009). Clouds interact with both shortwave radiation, cooling the surface, and longwave radiation, warming up the surface. The net effect depends on the season, the surface, cloud microphysical properties, and cloud macrophysical properties (Zhao and Garrett 2015). Unfortunately, arctic clouds are still poorly understood and future climate models are too uncertain to provide confident predictions (Stephens 2005; Boucher et al. 2013). A key parameter of the cloud radiative impact is the distribution of the cloud thermodynamic phase (Choi et al. 2014; Komurcu et al. 2014).

The physical and chemical properties determining ice nucleation rates are still poorly understood. Measurements of nucleation rates from laboratory and field studies, from the past two decades, can differ by orders in magnitude (Pruppacher 1995; Jeffery and Austin 1997).

Even if the Arctic is remote from major pollution sources, it is not necessarily pristine and high concentration of aerosols can be found in the atmosphere (Marelle et al. 2015). The low precipitation rate during winter and early spring allows pollution plumes from midlatitude to reach the Arctic (Stohl 2006; Garrett et al. 2010). Meteorological conditions

favor the presence of aerosols and set the "arctic haze."

In the upper troposphere, homogeneous nucleation mainly occurs at temperatures lower than -38°C, but aerosols can decrease the energy barrier and favor the phase transition, as described by the heterogeneous ice nucleation theory. Aerosols facilitate the transition through different processes: contact nucleation, deposition nucleation, and freezing nucleation. Efficient candidates of ice nuclei are mineral dusts (Rogers et al. 1998; DeMott et al. 2003) and the supercooling temperature required to create the transition from liquid to ice (ΔT*) can be up to 5.2°C (Sassen 2003). Organic materials associated with biomass burning can also act as efficient IN and decrease ΔT* as low as 1°C (Fukuta and Mason 1963; Popovitz-Biro et al. 1994). The magnitude of the energy needed for the phase transition to occur is proportional to $1/\Delta T^2$ (Pruppacher 1995).

Rangno and Hobbs (2001), from aircraft measurements of arctic stratocumulus, analyzed possible mechanism of ice production. From the observations of the high ice particle concentration retrieved in moderately supercooled arctic clouds, Rangno and Hobbs (2001) explained that ice concentrations can be enhanced by the fragmentation and shattering of drops during freezing in free fall. They suggested that cloud tops with large liquid droplet ($r_e > 10\mu$m) at temperatures between -20° and -10°C are characterized by ice concentration greater than ice nuclei due to the fragmentation of ice crystals. In the light of results presented in Chapters 4 and 5, which show that anthropogenic aerosols decrease efficiently the liquid cloud droplet effective radius, a decrease of ice formation is therefore expected in relation with an increase of anthropogenic aerosols.

In this study, we examine ice phase frequency, defined as the frequency of ice clouds compared to liquid and ice clouds, as a function of cloud top temperature for specific meteorological parameter regimes (specifically specific humidity (SH) and lower tropospheric stability (LTS), for different values of pollution content and cloud droplet radius. Previous work has used the exponential function of ice frequency as a function of temperature like in Cloud-Aerosol Lidar with Orthogonal Polarization algorithm (Hu et al. 2009), or functions used in cloud models (Le Trent and Li 1991; Del Genio et al. 1996). Here, instead a hyperbolic tangent function of the ice frequency (X_{ice}) is used to fit observations:

$$X_{liq,ice} = (1 + tanh(a_1 \times T + a_2))/2. \tag{6.1}$$

We define the ice fraction as the ratio of ice pixels over the total number of liquid and ice pixels for a given temperature bin. We do not claim here that the hyperbolic function better represents a one-to-one relationship between ice fraction and temperature, but it presents the following advantages:

- The hyperbolic function effectively represents the observation of ice fraction (Doutriaux-Boucher and Quaas 2004); Mathematically, we can ensure that the ice fraction tends to 100% below -40°C and to 0% above 0°C, boundaries of the classical nucleation theory.

- The constant a_1 controls the flatness of the curve. Thus, a lower absolute value of a_1 represents a slower water-ice transition with respect to temperature. The a_2 constant controls the 50% ice-fraction temperature shift.

- The parameter $-a_2/a_1$ represents the temperature for which the ice-cloud fraction is equal to the liquid-cloud fraction (e.g., $X_{liq,ice} = 50\%$). This temperature is considered here as the median freezing temperature. a_2/a_1 is the apparent ΔT^*.

In this manner, use of hyperbolic fitting function simplifies study of liquid-solid water transitions in Arctic clouds as a function of meteorological and aerosol concentration regime.

However, we consider neither mixed-phase clouds nor clouds with a phase for which the confidence in cloud phase is not high enough (Riedi et al. 2010). We can ensure that the sum of ice and liquid fractions is equal to 100% for each temperature bin, and the radiative and the microphysical cloud properties are not biased by cloud phase retrieval errors.

6.2 Data

We vertically, horizontally, and temporally colocate cloud data from POLDER and MODIS with meteorological parameters from ERA-Interim reanalysis (Berrisford et al. 2011) from ECMWF (European Centre for Medium-Range Weather Forecasts), especially LTS and SH as a proxy of humidity, from 2005 to 2010. Finally, carbon monoxide (CO) is used as a passive tracer of aerosols from the numerical tracer transport model GEOS-Chem (Goddard Earth Observing System).

Thermodynamic phase transitions from liquid to ice clouds can be favored by the presence of desert dust in the Arctic (Xie 1999; DeMott et al. 2003; Quinn et al. 2007b).

In order to not be biased by this effect so that we obtain only the effects of anthropogenic aerosols, we discard pixels for which desert-dust aerosol optical depth comprises more than 80% of the total aerosol optical depth for different aerosol types (desert dust, sea salt, organic matter, black carbon, and sulphate) obtained from MACC (Monitoring Atmospheric Composition & Climate) reanalyses from ECMWF (Stein et al. 2010; Antonakaki and Arola 2013). Since the focus here is on the effect of anthropogenic pollution on clouds, only GEOS-Chem spatial bins where anthropogenic sources comprise more than 80 % of total CO concentrations are considered for comparison with cloud properties.

Meteorological parameters can enhance or inhibit interactions between clouds and aerosols (c.f. Chapters 4 and 5) and act on cloud microphysical properties (Garrett and Zhao 2006; Chen et al. 2014; Andersen and Cermak 2015). In order to control for these impacts, we limit LTS to a range between 15.2 K and 22 K and SH from 0.8 g kg^{-1} and 4 g kg^{-1}. These ranges correspond to 15% of the span of LTS and SH centered at the respective mode of each of their distributions (c.f. Fig. 4.2). We estimate that within this range, meteorological parameters are sufficiently constrained that any observed supercooling freezing temperature change can be attributed to the aerosols concentration or change in droplet effective radius and not to a correlation between the aerosol concentration or droplet effective radius and meteorological parameters (c.f. Chapters 4 and 5).

6.3 Results and discussion

Figure 6.1 shows an example of the ice fraction as a function of temperature for four distinct anthropogenic CO concentration regimes as defined by quartiles in χ_{CO}. The left panel shows the raw data and the right panel shows curves fitted by the hyperbolic tangential of Eq. (6.1). The observed curves reach an ice fraction of 0 above 0°C and 1 below -40°C which is consistent with classical ice nucleation theories and observations. The ice fraction associated with the most polluted regimes (e.g., with CO concentration greater than 70 ppb) are associated with the highest freezing temperatures and lowest values of ΔT^* (17°C). The implication is that the anthropogenic pollution plumes decrease ΔT^*.

We use the International Satellite Cloud Climatology (ISCCP) cloud classification to define several cloud types according to their optical depth τ and cloud top pressure (P_{top}) represented in Figure 6.2 (Rossow et al. 1991). The ISCCP proposes a classification of

nine different types of clouds according to the values of cloud optical depth and pressure adapted for remote sensing studies. Three bins of optical depth and three bins of cloud top pressure (P_{top}) are used. Clouds are separated into three tropospheric layers: from 1,000 to 680 hPa for low-level clouds including stratocumulus, stratus, and cumulus; from 680 to 440 hPa for altocumulus, altostratus, and nimbostratus; and high-altitude clouds with P_{top} greater than 440 hPa including cirrus, cirrostratus, and cirrocumulus.

For this study, we consider only stratocumulus ($1000<P_{top}(hPa)<680$; $3.6< \tau <23$), stratus ($1000< P_{top}(hPa)<680$; $23< \tau$), nimbostratus ($680<P_{top}(hPa)<440$; $23< \tau$), and altostratus ($1000< P_{top}(hPa)<680$; $3.6< \tau <23$). These cloud classes have statistically significant samples of both ice and liquid clouds which allow the calculation of ice fraction for temperature bins of 1°C between -40 and 0°C.

Figure 6.3 shows ΔT* as a function of the liquid-cloud-droplet r_e for these cloud types. On average, ΔT* decreases by 1°C between the lower and higher quartile in r_e. For example, ΔT* for stratocumulus clouds is 15.3°C for liquid-cloud r_e smaller than 7.5 μm and drops to 14.3°C for liquid-cloud r_e greater than 15 μm. On average for all cloud types, ΔT* decreases of 0.9°C between the regimes defines as the upper and lower quartile in r_e. Rangno and Hobbs (2001) observed this result and showed that, in arctic stratus, larger liquid-cloud droplets tend to increase ice concentration.

Figure 6.4 shows the parameters a_1 and a_2 from the hyperbolic tangential fit from Eq. (6.1) for different χ_{CO} regimes. The a_2 parameter increases with χ_{CO} for each cloud types meaning that ΔT* decreases with increasing χ_{CO}. For stratocumulus, a_2 ranges from -3.2 to -4.6. On the other hand, the parameter a_1 decreases when χ_{CO} increases meaning that the speed of the liquid-ice transition increases while the CO concentration increases. For stratocumulus, it ranges from -0.14°C^{-1} for χ_{CO} below 44 ppb to -0.26°C^{-1} for χ_{CO} greater than 75 ppb. Averaged for the 4 cloud types, a_1 decreases on average by 0.08°C^{-1} between the lower and upper quartiles χ_{CO} regimes. Anthropogenic aerosols decrease the supercooling freezing temperature and accelerates the transition.

In order to compare the χ_{CO} effect on ΔT* with the r_e effect on ΔT* (Fig. 6.3), Figure 6.5 shows ΔT* for four χ_{CO} regimes delimited by the quartile values. For the different cloud types, ΔT* decreases with increasing CO concentration. For example, the ΔT* of stratocumulus clouds ranges from 22.1°C for χ_{CO} below 44 ppb to 17.2°C for χ_{CO} greater than

75 ppb. On average for all cloud types, ΔT^* decreases by 5.5°C between the lower and upper quartile in χ_{CO}.

The liquid-cloud-droplet mean r_e is represented in Figure 6.5 by the color bar. For example, the mean r_e for stratocumulus ranges from 12.4 μm for $\chi_{CO} < 44$ ppb to 10.4 μm for $\chi_{CO} > 75$ ppb. The same conclusions can be drawn for all cloud types. The difference in ΔT^* between the upper and lower quartile in r_e classes (0.85°C) is lower than the difference in ΔT^* between the extreme χ_{CO} regimes (5.5°C).

As described in Chapters 4 and 5, the presence of anthropogenic aerosols in the Arctic decreases liquid-cloud-droplet r_e. Figure 6.3 shows that smaller liquid droplet effective radius increases the freezing supercooling temperature, and Figure 6.4 suggests that an increase in aerosol concentration decreases the freezing supercooling temperature. These three results seem contradictory, suggesting that another effect is interfering while CO concentration increases and is beyond the induce liquid-droplet effective-radius decrease.

The free-energy barrier of an ice embryo is related to the ΔT^* as function of $1/\Delta T^{*2}$ as described in Eq. (1.35) (Pruppacher and Klett 1997). Table 6.1 shows the ratio of energy between the upper quartile in χ_{CO} (e.g., χ_{CO} is greater than 75 ppb) and the lower quartile in χ_{CO} (e.g., χ_{CO} is below 44 ppb), for the four cloud categories, inferred from values of ΔT^* from Figure 6.5. On average, polluted plumes decrease the free energy barrier by about 42%. The changes are particularly important for high-altitude clouds with a decrease of 48% for altostratus against 33% for stratus clouds.

We can hypothesize on the reasons of the decrease in freezing free energy due to the presence of anthropogenic aerosols. Aerosols, in the Arctic, decreases the liquid-droplet effective radius and increase the droplet concentration through the first indirect effect (Lihavainen et al. 2008; Tietze et al. 2011; Sporre et al. 2012). The increase of cloud droplet concentration increases the collision of droplet with each other, and enhances the formation of ice by contact freezing (Niehaus and Cantrell 2015). The free-energy barrier changes due to aerosol concentration variations, may be important through changes to the net radiative properties of arctic clouds. Because ice crystals grow by deposition, aggregation, and riming, precipitating when the size crosses a threshold, the potential is for a shorter lifetime of clouds (DeMott et al. 1998).

6.4 Conclusion

We evaluated the supercooling temperature required to trigger the liquid-ice phase transition of arctic clouds under specific regimes of meteorological parameters determined from ERA-I reanalysis. Cloud properties retrieved from POLDER and MODIS were colocated with χ_{CO} from the numerical tracer transport model GEOS-Chem that served as a passive tracer of aerosol plumes. The freezing-temperature sensitivity of clouds to pollution plumes was analyzed, while meteorological parameters were constrained. Our results confirm one of the conclusions from Rangno and Hobbs (2001), which stated that smaller liquid-cloud-droplet r_e increases the concentration of ice crystals. The hypothesis formulated in the introduction, which stated that the increase of anthropogenic aerosols, leading to a decrease in liquid effective radius, would increase the freezing supercooling temperature is refuted. Despite an observed decrease of r_e under polluted regimes, the presence of aerosols decreases ΔT^* by 5°C. The decrease in ΔT^* leads to a decrease in the free-energy barrier of the liquid-ice phase transition of 42% on average.

The anthropogenic pollution in the Arctic is decreasing (Hirdman et al. 2010) but new local sources, such as gas flaring or shipping, might increase the aerosol concentration in the Arctic (Peters et al. 2011). From the results shown in this study, the energy barrier could be greatly diminished, enhancing the precipitation and potentially reducing the lifetime of arctic clouds and changing their net radiative properties (DeMott et al. 1998). As stated in the introduction of this chapter, an important aspect of the Arctic is the high fraction of mixed-phase clouds (Mioche et al. 2014). Mixed-phase-cloud radiative properties play an important part in the arctic warming (Klein et al. 2009; Gayet et al. 2009; Uchiyama et al. 2013) and their response to enhanced aerosol concentration needs to be further studied.

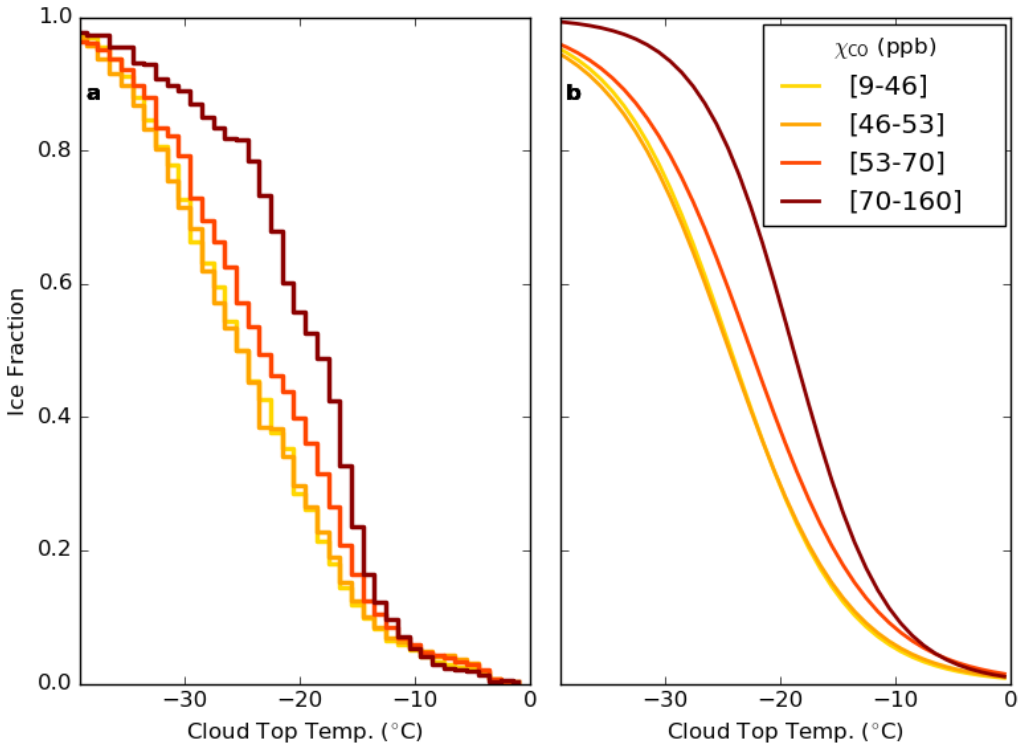

Figure 6.1: Ice fraction as function of cloud top temperature with the corresponding hyperbolic tangential fit. (a) Ice fraction as function of cloud top temperature for 4 χ_{CO} regimes defined by χ_{CO} distribution quartiles. (b) Hyperbolic tangential fit of the ice fraction as function of the cloud top temperature, for the 4 χ_{CO} regimes, presented by Equation (6.1).

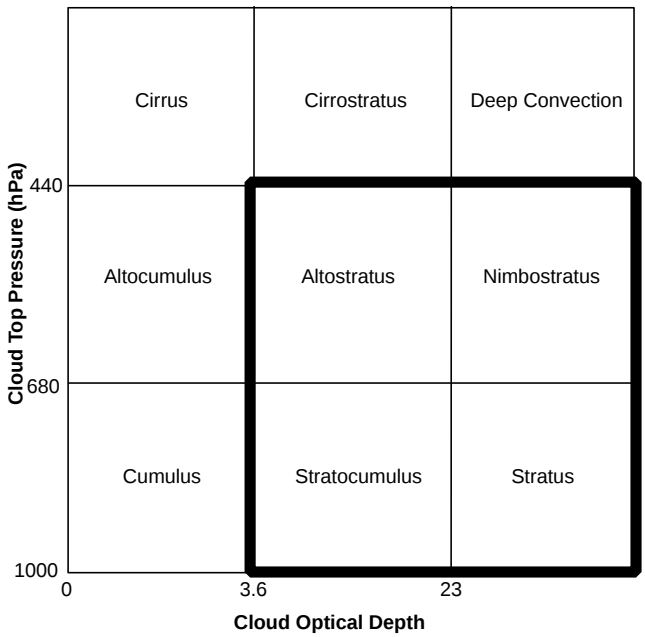

Figure 6.2: Cloud repartition by the ISCCP as a function of the cloud top altitude and cloud optical depth. Boxes with a thicker border are the cloud types considered in this study.

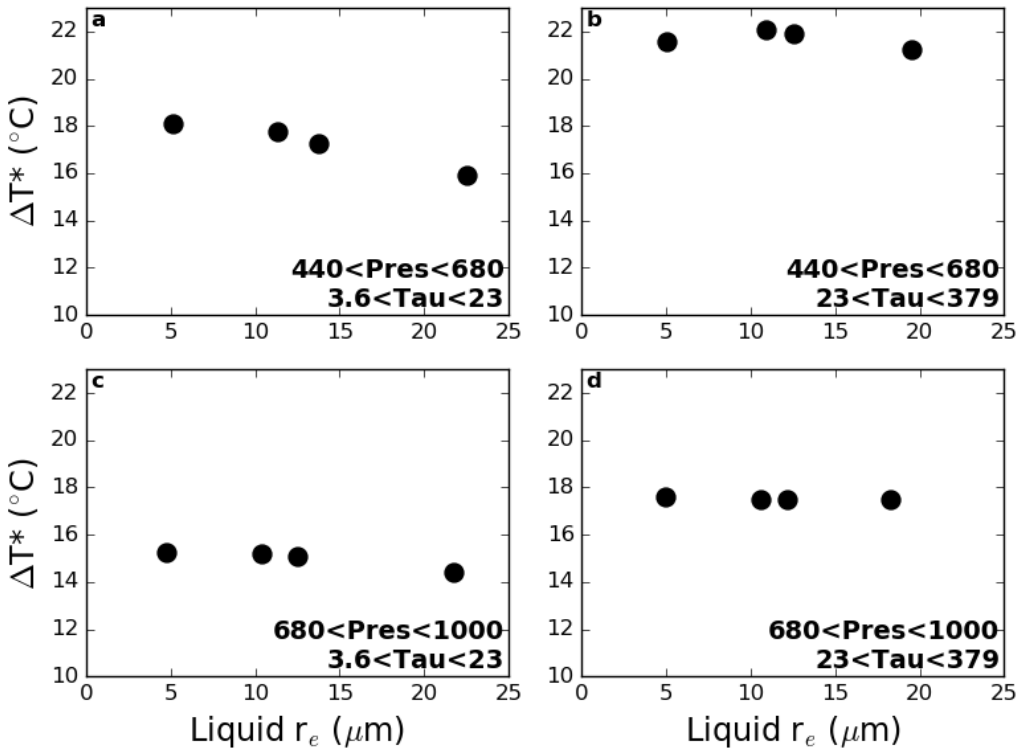

Figure 6.3: ΔT* as function of the liquid-cloud-droplet effective radius for 4 cloud categories differentiated by their optical depth and top pressure.

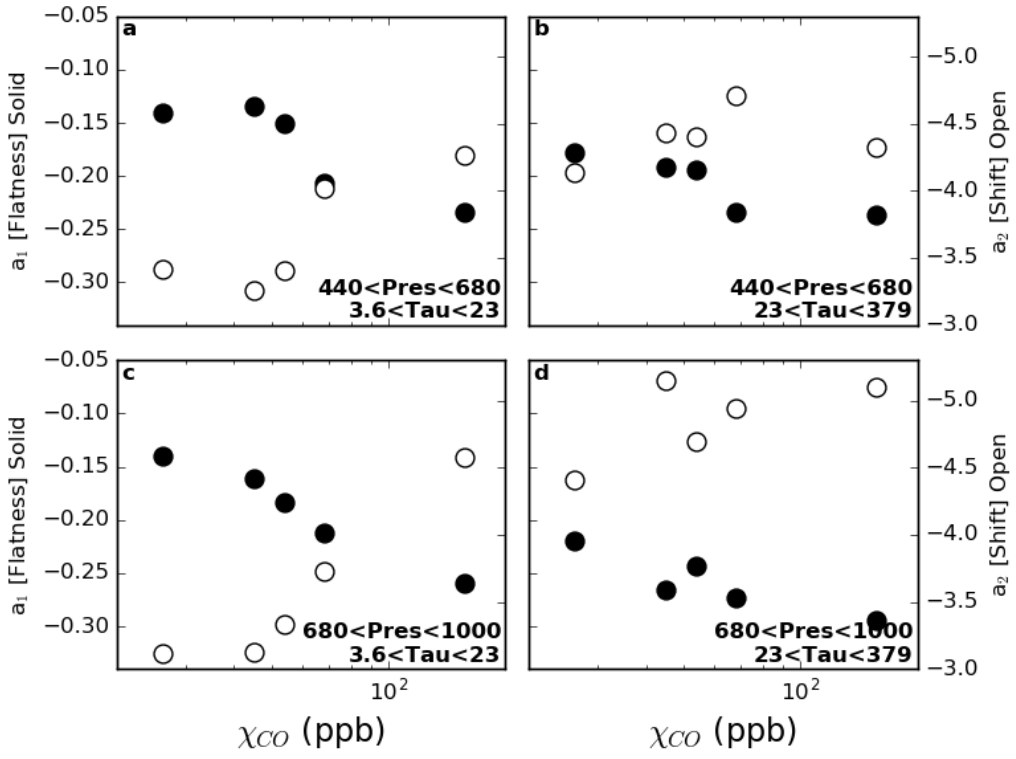

Figure 6.4: Parameters a_1 (solid) and a_2 (hollow), from Eq. (6.1), as function of the CO concentration (χ_{CO}). Parameters a_1 and a_2 defined respectively the flatness and the shift of the hyperbolic tangential fit of the ice fraction versus the cloud top temperature. Results are presented for 4 cloud categories differentiated by their optical depth and top pressure.

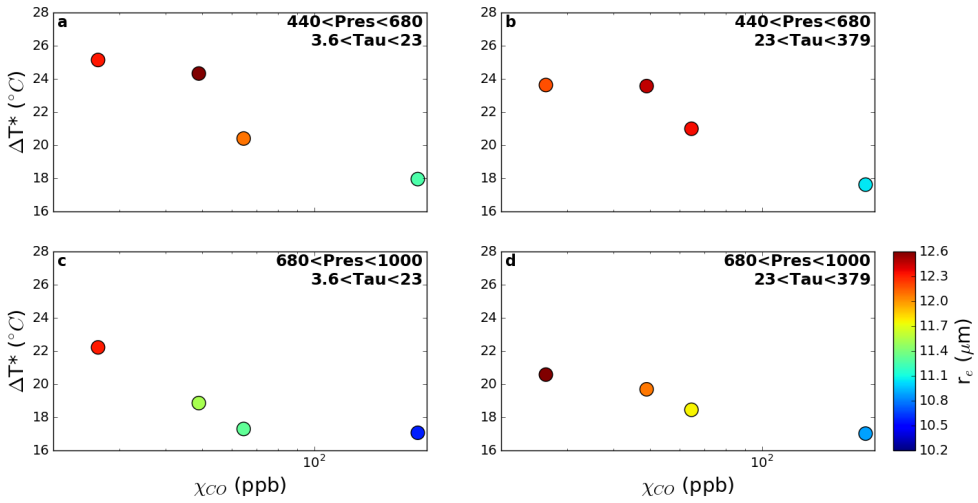

Figure 6.5: ΔT* as function of the CO concentration (χ_{CO}) for 4 cloud categories differentiated by their optical depth and top pressure. The color scale corresponds to the associated mean liquid-cloud droplet effective radius.

Table 6.1: Ratio of the free energy barrier of the thermodynamic phase transition between polluted and clean air pollution plumes is inferred from Figure 6.5.

	Altostratus	Nimbostratus	Stratocumulus	Stratus
ΔT* (°C) (clean)	25	23.9	22	20.6
ΔT* (°C) (polluted)	18	17.8	17	17
ΔG (polluted)/ΔG (clean)	0.52	0.55	0.60	0.67

CHAPTER 7

SUMMARY AND FUTURE WORK

7.1 General Conclusions

The Arctic is a region of high interest due to the observed rapid warming and the direct consequence of climate change leading to sea-ice melting. Changes in arctic climate can have major ecological consequences that could disturb the eco-system and the oceanic circulation with an impact on Earth's climate. Unlike midlatitude clouds, arctic clouds have a warming impact on the Arctic due to the presence of sea-ice and absence of sun radiation during winter. It is essential to assess cloud radiative and microphysical properties to better understand the present warming and the different factors that influence it. Aerosols are known to influence surface temperature (e.g., the parasol effect) (Crutzen and Ramanathan 2003) and change cloud radiative and microphysical properties: aerosols can act as cloud condensation nuclei or ice nuclei that facilitate, respectively, the vapor to liquid or liquid to solid water transition in the atmosphere. Aerosols can also change the microphysical properties of liquid clouds through the first indirect effect. This interaction leads to smaller cloud droplets and brighter clouds in the shortwave if the liquid-water content is held constant.

Different approaches have been developed to analyze interactions between aerosols and clouds using ground based, in situ, satellite, or a combination of satellite and model datasets. We choose the last option and colocating data from the satellite instruments MODIS and POLDER, both part of the A-train, with numerical tracer transport model output from FLEXPART and GEOS-Chem. Here, both numerical tracer transport models are used to describe carbon monoxide (CO) concentrations as a proxy for aerosols. The main reason that CO is used as a passive tracer of aerosols is that both quantities are highly correlated at the sources and that CO is not impacted by cloud process. Aerosols are removed from numerical simulations when they interact with clouds making it difficult to use this variable for studying aerosol-cloud interactions. In order to focus on

pollution-cloud interactions, we account for meteorological variability using reanalysis dataset to control for specific humidity (SH) and lower tropospheric stability (LTS). Any observed difference in cloud parameters is solely due to aerosols and not to a correlation of meteorological parameters with aerosol concentrations. In our study, we focus on clouds over the Arctic ocean between 2005 and 2010 at latitudes greater than 65°.

Chapter 3 is devoted to an overview of climatological analyses of clouds, CO, and meteorological parameters. This chapter shows variations in optical depth in the Arctic, and differences in CO concentration between the seasons. We find that meteorological parameters are highly correlated with season. Constraining for meteorological parameters, the seasonal variability is diminished. The study illustrates that while in situ studies are important, they only focus on a particular time of the year that can be under the influence of a specific event, such as high biomass-burning concentration or strong atmospheric instability. A broad statistical analysis is needed to assess the effect of aerosols on clouds independently of the impact of meteorological variability.

Chapter 4 addresses the effect of anthropogenic aerosols on liquid clouds over the Arctic. We use FLEXPART numerical tracer transport model output of CO from 2008 and 2010 and cloud observation from POLDER and MODIS satellite instruments. We control for meteorological variability in order to better represent aerosol-cloud interactions. Anthropogenic aerosols are most of the time secondary aerosols, coated with sulfate during their transport which makes them efficient cloud condensation nuclei (CCN). In our study we compared the net aerosol cloud interaction parameters (ACI^{net}) for different cloud top altitudes, cloud top temperatures, liquid water path (LWP), LTS, SH, and aerosol concentration regimes. We observe that ACI^{net} increases with temperature. This sensitivity can be explained by a lower correlation of CO with aerosols due to dry scavenging. We also find that ACI^{net} depends on aerosol concentration and ranges between 0.10 at CO concentration (χ_{CO}) greater than 10 ppbv and 0.31 at χ_{CO} lower than 5.5 ppbv: low aerosol concentrations are associated with high ACI^{net}. We explain the difference by either reduced correlation of CO with aerosol due to longer transport, or differences in aerosol chemistry due to different sources. There is an increase of ACI^{net} with LTS that appears to be unique to the Arctic. Considering changes in optical thickness, the ACI^{net} equals to 0.10 for LTS less than 14 K and is as high as 0.31 for LTS greater than 23 K. The difference can be associated with

the lower LTS regime that favors arctic-cloud formation compared to midlatitude-cloud formation. The arctic sea ice decreases the atmospheric stability and, therefore, influences the ACI. ACI^{net} also increases with SH. Considering changes in optical thickness, the ACI^{net} equals to -0.10 for SH less than $1.2\,g\,kg^{-1}$ and is as high as 0.20 for SH greater than $3.6\,g\,kg^{-1}$. This effect shows either competition of liquid droplets when the atmosphere is dry or entrainment of dry air within cloud tops which evaporates preferentially small liquid cloud droplets (Ackerman et al. 2004). The comparison of ACI values from the different studies from Table 1.1 from the introduction has to be done carefully. For example, two different geographical regions may have different meteorological states and consequently have potentially different values of ACI, setting aside ACI variability due to aerosol type and chemistry.

In Chapter 5, we compare the effect on low-level liquid clouds of pollution plumes from biomass-burning and anthropogenic sources. We use the CO concentrations from GEOS-Chem from 2005 to 2010. We find that if we do not constrain for meteorological variability, both anthropogenic and biomass-burning plumes have an average ACI^{net} of 0.17 ± 0.10. On the contrary, if the LTS and SH of the atmosphere are controlled for, the ACI^{net} associated with biomass-burning plumes decreases to 0.05 ± 0.20 and to the point that there is no correlation between the CO concentration and cloud optical depth and effective radius. On the other hand however, values of ACI^{net} associated with anthropogenic pollution plumes have a value that increases and lies close to a theoretical maximum value of 0.33 when meteorological parameters are constrained. It appears that CO concentrations from biomass-burning pollution plumes are positively correlated with both SH and LTS whereas CO concentrations from anthropogenic pollution plumes are negatively correlated with SH and LTS. Not controlling for meteorology parameters, allows a variation of aerosol content correlated with a variation of meteorological parameters, enhancing the ACI^{net} for biomass-burning aerosols, and reducing the ACI^{net} for anthropogenic aerosols. Two theories may explain the low values of ACI^{net} for biomass-burning plumes: (i) biomass-burning plumes are associated with wet scavenging during summer, which reduces the correlation between CO and aerosols or (ii) aerosols from biomass-burning plumes are less hydrophilic than anthropogenic aerosols and act as inefficient CCN. Referring to Table 1.1, our value of ACI^{net} associated with anthropogenic plumes is one of the highest compared

to other studies and lies closest to the theoretical maximum of the first indirect effect. Our value of ACI^{net} confirms that arctic cloud microphysical and radiative properties are more sensitive to aerosols than in other regions.

Chapter 6 examines the phase transitions from liquid to ice in low-level clouds. We use CO concentrations from the numerical tracer transport model GEOS-Chem for a period between 2005 and 2010 and focus on anthropogenic pollution plumes to obtain a significant number of data points for statistical analysis. We use a tangent hyperbolic function to represent the ice fraction, defined as the ratio of number of ice-cloud pixel over the number of ice- and liquid-cloud pixel, as a function of the supercooling temperature and we control for cloud parameters (effective radius, liquid water path, cloud top pressure), LTS , SH, and CO concentrations. As Rangno and Hobbs (2001) have shown, we observe an increase of freezing temperatures when the cloud droplet effective radius decreases. The freezing supercooling temperature is defined as the supercooling temperature for which the ice fraction is equal to 50%. We expect a decrease of freezing supercooling temperature with an increase of anthropogenic pollution concentration due to reduced liquid droplet size. However, the opposite is observed. Our results show that the decrease of effective radius from 19 μm to 5,μm effectively increases the supercooling freezing temperature by 1°C. The increase of CO concentration from χ_{CO} less than 44 ppb to χ_{CO} greater than 75 ppb decreases the supercooling freezing temperature from 22.1 to 17.2°C. We do not have a definite explanation, but a potential mechanism is that the numerous droplets, due to an increase in CCN, decrease the mean free path of a droplet and impact between cloud droplet is more likely to happen which can trigger the phase transition (Niehaus and Cantrell 2015).

7.2 Future works

This dissertation examined use of passive tracer from a numerical tracer transport model combined with satellite data to observe the effect of pollution plumes on clouds. By considering multiple years and the Arctic as a whole, the large number of data points allowed for robust statistical analyses of the aerosol indirect effect and of liquid-ice phase transition in clouds.

Past studies have been interested by the interaction of clouds with sea ice or snow cover

(Curry 1995; Kay et al. 2008; Screen and Simmonds 2010; Kay and L'Ecuyer 2013; Bennartz et al. 2013; Liu and Key 2014). Sea-ice cover has an impact on the meteorological conditions of the Arctic. When it is present, it dries the atmosphere and makes it more stable by lowering surface temperature (Schweiger et al. 2008). Any future decrease of sea-ice extent will modify the meteorological conditions and will impact the cloud microphysical properties and their interactions with aerosols. Along the same idea that what Zhao and Garrett (2015) have developed, we could retrieve cloud properties under polluted and clean events, retrieve their radiative properties and evaluate consequences of the sea-ice on the ACI. Several instruments can be used: passive or active sensors, ground based measurements, or data from Ice Atmosphere Arctic Ocean Observing System (IAAOOS) which is a network of Light Detection And Ranging (LIDAR) (Provost et al. 2015) and retrieves informations on ocean, sea ice, and atmosphere.

In this dissertation we have been looking at pollution plumes from combustion processes (fossil fuel and biomass burning). In the atmosphere there are other aerosols that can reach the Arctic such as desert dust and aerosols from volcanic plumes, that could potentially interact with clouds (Sassen et al. 2003; McCoy and Hartmann 2015). Tanaka and Chiba (2006) hypothesize that dust in the Arctic, mainly from East Asia, can have a potential impact on climate. Studies in the Arctic, considering dust, are focused on the surface albedo impact (Zdanowicz et al. 1998; Tanaka and Chiba 2006). Even if desert dust has been stated as efficient ice nuclei (IN) (Phillips et al. 2008; Niemand et al. 2012), studies focused on the Arctic are few (Paukert and Hoose 2014). A potential extension of our study would be to compare cloud microphysical parameters during desert-dust events with cloud parameters during clean regimes, while meteorological parameters are controlled. This could help understanding the impact of aerosols from these remote sources on arctic clouds. Reanalysis or models, such as the aerosol optical depth for different aerosol sources provided by MACC reanalysis from ECMWF, indicate the aerosol concentration and can be colocated with clouds, as we did with the CO. A complication compared to the methodology developed for this dissertation is that we should account for the fact that aerosols are removed from simulation when they interact with clouds: the ACI parameter could be diminished. Another solution would be to identify pollution events from ground based measurements, and observe cloud properties from space and comparing cloud prop-

erties under polluted and clean conditions controlled for same meteorological parameters settings. Other aerosols act as efficient CCN, dimethyl sulphide are more efficient than sulphate (Pandis et al. 1994), or on the opposite inhibit the action of aerosols, sea-salt aerosols decrease the fraction of activated sulphate aerosols (Ghan et al. 1998).

Before reaching the Arctic, CO concentration can be decorrelated from aerosol concentration in the atmosphere due to precipitation. The results presented in the dissertation still have the uncertainty that precipitation occurred, therefore, the study is limited to the interaction of pollution plumes with clouds. Questions remain in our analyses: In what proportion do CO and aerosols remain correlated after their transport up to the Arctic? Do we observe the aerosol-cloud interaction or the impact of midlatitude source on arctic cloud microphysical properties? To avoid the problem of decorrelation between the passive tracer CO and aerosols, back-trajectories from a model could be used to select only air parcels which have not been affected by precipitation en route to the Arctic. The conclusion of the aerosol impacts on cloud properties would be more robust and precise.

We could also improve cloud property description by adding measurements from other satellites from the A-train such as CALIOP and CloudSat. These can be used to retrieve the vertical profile of cloud and precipitation properties. The data could then be applied to assess aerosol impacts on cloud precipitation amount (L'Ecuyer et al. 2009; Lee et al. 2016). Also, use of passive instruments, such as POLDER and MODIS, cannot distinguish the presence of mixed phase clouds from multilayer clouds. However, CALIOP has been successful in observing mixed-phase clouds (Mioche et al. 2014). Mixed-phase cloud occurrence is estimated to 20% in the Arctic below 2 km (Mioche et al. 2014) and these clouds have important impacts on surface radiations (Shupe and Intrieri 2004). However, Jackson et al. (2012) have pointed out that study of mixed-phase clouds has to be done in a wider variety of meteorology conditions to identify the dominant aerosol forcing mechanism in mixed-phase clouds. Moreover, biomass burning aerosols have been defined as ice nuclei (Hobbs and Locatelli 1969; Pueschel and Langer 1973), their presence can trigger ice precipitation and potentially the formation of mixed-phase clouds. Coupled with a passive tracer from a numerical tracer transport model, CALIOP observations could help understand the impact of aerosols on mixed-phase-cloud fractions. Moreover, CALIOP lidar and CloudSat radar provide additional and independent information on droplet

concentration and geometric depth that may be used to obtain a deeper understanding of the mechanisms behind aerosol-cloud interactions.

Studies presented for this dissertation already provide important results and significant observational constraint to develop aerosol-cloud interaction parameterization in models. Our analyses also open several paths for further investigation that will benefit greatly from an integrated approach coupling satellite observation, model reanalysis, and air masses history reconstruction through statistical back trajectory reanalysis.

APPENDIX

SEA-ICE EXTENT

Figures A.1 and A.2 show the monthly average of arctic sea-ice concentration from 2005 to 2010 from data retrieved by Cavialieri et al. (1996) from the National Snow and Ice Data Center (NSIDC) that uses Special sensor microwave/images from 2005 to 2007, and The Special Sensor Microwave Imager/Sounder after 2007 processed with the NASA Team algorithm, provided at 25 km spatial resolution. A large part of the arctic ocean is covered by sea ice, the extent of which depends on the season. In September, the extent is minimal because it has melted during spring and summer. On the contrary, after September the sea ice recovers in a large part of the arctic ocean, month after month, and reaches its maximum in March.

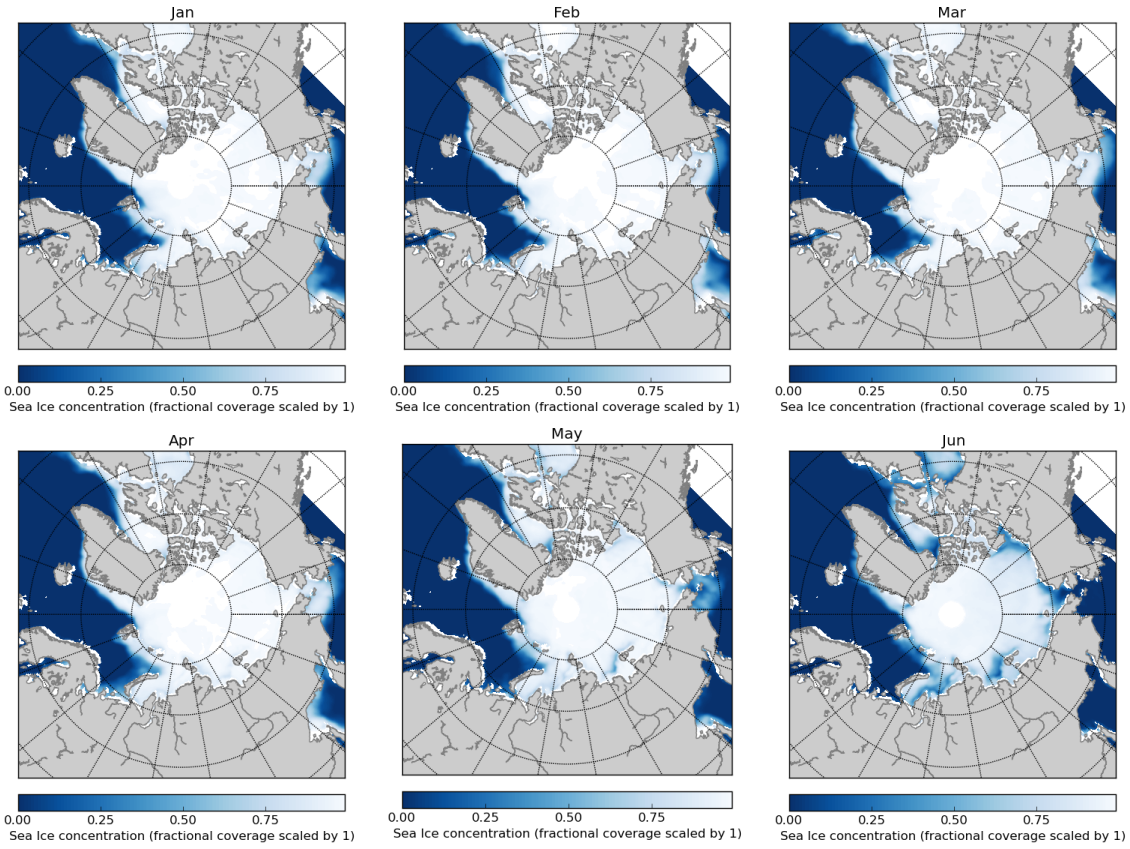

Figure A.1: Average monthly sea-ice concentration, for the year from 2005 to 2010, defined as the fractional coverage normalized from January to June. We used the months in the years from 2005 to 2010.

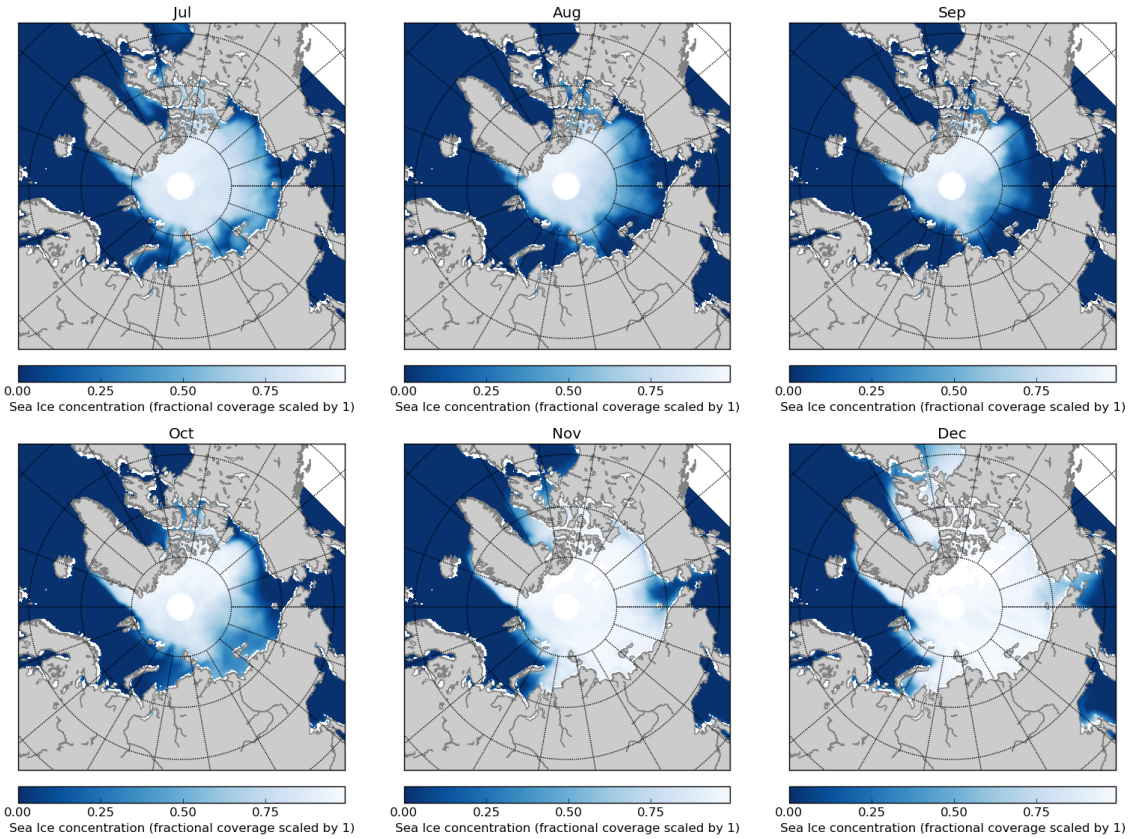

Figure A.2: Same as Figure A.1 but from August to December.

REFERENCES

Ackerman, A. S., M. P. Kirkpatrick, D. E. Stevens, and O. B. Toon, 2004: The impact of humidity above stratiform clouds on indirect aerosol climate forcing. *Nature*, **432**, 1014–1017, doi:10.1038/nature03137.1.

Ackerman, S. A., K. I. Strabala, W. P. Menzel, R. A. Frey, C. C. Moeller, and L. E. Gumley, 1998: Discriminating clear sky from clouds with MODIS. *J. Geophys. Res.: Atmos.*, **103 (D24)**, 32 141–32 157, doi:10.1029/1998JD200032.

Albrecht, B. A., 1989: Aerosols, cloud microphysics, and fractional cloudiness. *Science*, **245 (4)**, 1227–1230.

Amann, M., and Coauthors, 2011: Cost-effective control of air quality and greenhouse gases in Europe: Modeling and policy applications. *Environ. Model. & Software*, **26 (12)**, 1489–1501, doi:10.1016/j.envsoft.2011.07.012.

Ambartsumian, V. A., 1942: Diffusion of light by planetary atmospheres. *Astron. Zh.*, **19**, 30–41.

Ancellet, G., J. Pelon, Y. Blanchard, B. Quennehen, A. Bazureau, K. S. Law, and A. Schwarzenboeck, 2014: Transport of aerosol to the Arctic: Analysis of CALIOP and French aircraft data during the spring 2008 POLARCAT campaign. *Atmos. Chem. Phys.*, **14 (16)**, 8235–8254, doi:10.5194/acp-14-8235-2014.

Andersen, H., and J. Cermak, 2015: How thermodynamic environments control stratocumulus microphysics and interactions with aerosols. *Environ. Res. Lett.*, **10 (2)**, 24 004, doi:10.1088/1748-9326/10/2/024004.

Andrade, F., C. Orsini, and W. Maenhaut, 1994: Relation between aerosol sources and meteorological parameters for inhalable atmospheric particles in Sao Paulo City, Brazil. *Atmos. Environ.*, **28 (14)**, 2307–2315, doi:10.1016/1352-2310(94)90484-7.

Andreae, M., and D. Rosenfeld, 2008: Aerosol cloud precipitation interactions. Part 1. The nature and sources of cloud-active aerosols. *Earth-Sci. Rev.*, **89 (1-2)**, 13–41, doi:10.1016/j.earscirev.2008.03.001.

Antonakaki, T., and A. Arola, 2013: Validation report of the MACC reanalysis of global atmospheric composition. Tech. rep, 85 pp.

Arakawa, A., 1975: *The Physical Basis of Climate and Climate Modeling*. World Meteorological Organization, 265 pp.

Avey, L., T. J. Garrett, and A. Stohl, 2007: Evaluation of the aerosol indirect effect using satellite, tracer transport model, and aircraft data from the International Consortium for Atmospheric Research on Transport and Transformation. *J. Geophys. Res.*, **112 (D10)**, D10S33, doi:10.1029/2006JD007581.

Barrie, L. A., 1986: Arctic air pollution: An overview of current knowledge. *Atmos. Environ.*, **20 (4)**, 643–663.

Belchansky, G. I., D. C. Douglas, and N. G. Platonov, 2004: Duration of the Arctic sea ice melt season: Regional and interannual variability, 19792001. *J. Climate*, **17 (1)**, 67–80.

Bennartz, R., and Coauthors, 2013: July 2012 Greenland melt extent enhanced by low-level liquid clouds. *Nature*, **496 (7443)**, 83–86, doi:10.1038/nature12002.

Berg, L. K., C. M. Berkowitz, J. C. Barnard, G. Senum, and S. R. Springston, 2011: Observations of the first aerosol indirect effect in shallow cumuli. *Geophys. Res. Lett.*, **38 (3)**, doi:10.1029/2010GL046047.

Berrisford, P., D. Dee, K. Fielding, M. Fuentes, P. Kallberg, S. Kobayashi, and S. Uppala, 2011: The ERA-Interim Archive version 2.0. ECMWF, Reading, UK, 1–23 pp.

Bey, I., and Coauthors, 2001: Global modeling of tropospheric chemistry with assimilated meteorology: Model description and evaluation. *J. Geophys. Res.: Atmos.*, **106 (D19)**, 23 073–23 095, doi:10.1029/2001JD000807.

Bierwirth, E., and Coauthors, 2013: Optical thickness and effective radius of Arctic boundary-layer clouds retrieved from airborne nadir and imaging spectrometry. *Atmos. Meas. Tech.*, **6 (5)**, 1189–1200, doi:10.5194/amt-6-1189-2013.

Bilde, M., and B. Svenningsson, 2004: CCN activation of slightly soluble organics: The importance of small amounts of inorganic salt and particle phase. *Tellus, Ser. B*, **56 (2)**, 128–134, doi:10.1111/j.1600-0889.2004.00090.x.

Boisvert, L. N., and J. C. Stroeve, 2015: The Arctic is becoming warmer and wetter as revealed by the Atmospheric Infrared Sounder. *Geophys. Res. Lett.*, **42 (11)**, 4439–4446, doi:10.1002/2015GL063775.

Boyle, S., and J. Ardill, 1989: *The Greenhouse Effect*. Hodder and Stoughton, 298 pp.

Boucher, O., and Coauthors, 2013: IPCC. Climate Change 2013: The Physical Science Basis. Contribution of Working Group I to the Fifth Assessment Report of the Intergovernmental Panel on Climate Change, 571–657, doi:10.1017/CBO9781107415324.016.

Brenguier, J., and R. Wood, 2009: Observational strategies from the micro to meso scale. *Clouds in the Perturbed Climate System: Their Relationship to Energy Balance, Atmospheric Dynamics, and Precipitation*, J. Heintzenberg, and R. J. Charlson, Eds., MIT Press, MASS, Cambridge, 487–510.

Brenguier, J.-l., H. Pawlowska, and L. Schu, 2003: Cloud microphysical and radiative properties for parameterization and satellite monitoring of the indirect effect of aerosol on climate. *J. Geophys. Res.: Atmos.*, **108 (15)**, 4407, doi:10.1029/2002JD002682.

Brenguier, J. L., H. Pawlowska, L. Schüller, R. Preusker, J. Fischer, and Y. Fouquart, 2000: Radiative properties of boundary layer clouds: Droplet effective radius versus number concentration. *J. Atmos. Sci.*, **57 (6)**, 803–821.

Bréon, F.-M., and S. Colzy, 1999: Cloud detection from the spaceborne POLDER instrument and validation against surface synoptic observations. *J. Appl. Meteor.*, **38**, 777–785.

Breon, F.-M., D. Tanre, and S. Generoso, 2002: Aerosol effect on cloud droplet size monitored from satellite. *Science*, **295 (5556)**, 834–8, doi:10.1126/science.1066434.

Bretherton, F. P., Bryan, K., & Woods, J. D., 1990: Time-dependent greenhouse-gas- induced climate change. *Climate Change, The IPCC Scientific Assessment*, 173–194.

Brioude, J., and Coauthors, 2009: Effect of biomass burning on marine stratocumulus clouds off the California coast. *Atmos. Chem. Phys.*, **9**, 8841–8856, doi:www.atmos-chem-phys.net/9/8841/2009/.

Brock, C. A., and Coauthors, 2011: Characteristics, sources, and transport of aerosols measured in spring 2008 during the aerosol, radiation, and cloud processes affecting Arctic Climate (ARCPAC) Project. *Atmos. Chem. Phys.*, **11 (6)**, 2423–2453, doi:10.5194/acp-11-2423-2011.

Browse, J., K. S. Carslaw, A. Schmidt, and J. J. Corbett, 2013: Impact of future Arctic shipping on high-latitude black carbon deposition. *Geophys. Res. Lett.*, **40 (August)**, 4459–4463, doi:10.1002/grl.50876.

Bulgin, C. E., and Coauthors, 2008: Regional and seasonal variations of the Twomey indirect effect as observed by the ATSR-2 satellite instrument. *Geophys. Res. Lett.*, **35 (2)**, L02 811, doi:10.1029/2007GL031394.

Buriez, J. C., and Coauthors, 1997: Cloud detection and derivation of cloud properties from POLDER. *Int. J. of Remote Sens.*, **18 (13)**, 2785–2813, doi:10.1080/014311697217332.

Cantrell, W., and A. Heymsfield, 2005: Production of ice in tropospheric clouds: A review. *Bull. Amer. Meteor. Soc.*, **86(6)**, doi:10.1175/BAMS-86-6-795, 795–807.

Cavalieri, D., C. Parkinson, P. Gloersen, and J. Zwally, 1996 updated yearly: *Sea Ice Concentrations from Nimbus-7 SMMR and DMSP SSM/I-SSMIS Passive Microwave Data, Version 1.* Boulder, Colorado USA: NASA DAAC at the National Snow and Ice Data Center. doi:10.5067/8GQ8LZQVL0VL.

Chameides, W. L., C. Luo, R. Saylor, D. Streets, Y. Huang, M. Bergin, and F. Giorgi, 2002: Correlation between model-calculated anthropogenic aerosols and satellite-derived cloud optical depths: Indication of indirect effect? *J. Geophys. Res.: Atmos.*, **107 (D10)**, AAC 2–1–AAC 2–15, doi:10.1029/2000JD000208.

Chang, F. L., and J. A. Coakley, 2007: Relationships between marine stratus cloud optical depth and temperature: Inferences from AVHRR observations. *J. Climate*, **20**, 2022–2036, doi:10.1175/JCLI4115.1.

Chapman, W. L., and J. E. Walsh, 2007a: A synthesis of antarctic temperatures. *J. Climate*, **20 (16)**, 4096–4117, doi:10.1175/JCLI4236.1.

Chapman, W. L., and J. E. Walsh, 2007b: Simulations of Arctic temperature and pressure by global coupled models. *J. Climate*, **20 (4)**, 609–632, doi:10.1175/JCLI4026.1.

Chen, Y.-C., M. W. Christensen, G. L. Stephens, and J. H. Seinfeld, 2014: Satellite-based estimate of global aerosolcloud radiative forcing by marine warm clouds. *Nat. Geosci.*, **7 (September)**, 643–646, doi:10.1038/ngeo2214.

Choi, Y.-S., C.-H. Ho, C.-E. Park, T. Storelvmo, and I. Tan, 2014: Influence of cloud phase composition on climate feedbacks. *J. Geophys. Res.: Atmos.*, **119 (7)**, 3687–3700, doi:10.1002/2013JD020582.

Christensen, M. W., K. Suzuki, B. Zambri, and G. L. Stephens, 2014: Ship track observations of a reduced shortwave aerosol indirect effect in mixed-phase clouds. *Geophys. Res. Lett.*, **41 (19)**, 6970–6977, doi:10.1002/2014GL061320.

Church, J. A., and N. J. White, 2006: A 20th century acceleration in global sealevel rise. *Geophys. Res. Lett.*, **33 (1)**.

Coakley, J. A., R. L. Bernstein, and P. A. Durkee, 1987: Effect of ship-stack effluents on cloud reflectivity. *Science*, **237 (4818)**, 1020–1022.

Coakley, J. A., and C. D. Walsh, 2002: Limits to the aerosol indirect radiative effect derived from observations of ship tracks. *J. Atmos. Sci.*, **59 (3)**, 668–680.

Coopman, Q., T. J. Garrett, J. Riedi, S. Eckhardt, and A. Stohl, 2016: Effects of long-range aerosol transport on the microphysical properties of low-level liquid clouds in the Arctic. *Atmos. Chem. Phys.*, **16 (7)**, 4661–4674, doi:10.5194/acp-16-4661-2016.

Costantino, L., and F. M. Bréon, 2013: Aerosol indirect effect on warm clouds over South-East Atlantic, from co-located MODIS and CALIPSO observations. *Atmos. Chem. Phys.*, **13 (1)**, 69–88, doi:10.5194/acp-13-69-2013.

Cox, C. J., V. P. Walden, P. M. Rowe, and M. D. Shupe, 2015: Humidity trends imply increased sensitivity to clouds in a warming Arctic. *Nat. Commun.*, **6**, 10 117, doi:10.1038/ncomms10117.

Crutzen, P. J., and V. Ramanathan, 2003: The parasol effect on climate. *Science*, **302 (5651)**, 1679–1681, doi:10.1126/science.302.5651.1679.

Cubasch, U., and Coauthors, 2001: Projections of future climate change. *Climate Change 2001: The Scientific Basis: Contribution of Working Group I to the Third Assessment Report of the Intergovernmental Panel* 526–582.

Curry, J. A., 1986: Interactions among turbulence, radiation and microphysics in Arctic stratus clouds. *J. Atmos. Sci.*, **43 (1)**, 90–106.

Curry, J. A., 1995: Interactions among aerosols, clouds, and climate of the Arctic Ocean. *Sci. Total Environ.*, **160-161 (C)**, 777–791, doi:10.1016/0048-9697(95)04411-S.

Curry, J. A., J. O. Pinto, T. Benner, and M. Tschudi, 1997: Evolution of the cloudy boundary layer during the autumnal freezing of the Beaufort Sea. *J. Geophys. Res.: Atmos.*, **102 (D12)**, 13 851–13 860, doi:10.1029/96JD03089.

Curry, J. A., W. B. Rossow, D. Randall, and J. L. Schramm, 1996: Overview of arctic cloud and radiation characteristics. *J. Climate*, **9 (8)**, 1731–1764.

Curry, J. A., and Coauthors, 2000: FIRE Arctic Clouds Experiment. *Bull. Amer. Meteor. Soc.*, **81 (1)**, 5–29.

Dee, D. P., and Coauthors, 2011: The ERA-Interim reanalysis: Configuration and performance of the data assimilation system. *Quart. J. Roy. Meteor. Soc.*, **137 (April)**, 553–597, doi:10.1002/qj.828.

Del Genio, A. D., M.-S. Yao, W. Kovari, and K. K.-W. Lo, 1996: A prognostic cloud water parameterization for global climate models. *J. Climate*, **9 (2)**, 270–304.

Delanoë, J., A. Protat, O. Jourdan, J. Pelon, M. Papazzoni, R. Dupuy, J.-F. Gayet, and C. Jouan, 2013: Comparison of airborne in situ, airborne radarlidar, and spaceborne radarlidar retrievals of polar ice cloud properties sampled during the POLARCAT campaign. *J. of Atmos. and Oceanic Tech.*, **30 (1)**, 57–73, doi:10.1175/JTECH-D-11-00200.1.

DeMott, P. J., 2003: African dust aerosols as atmospheric ice nuclei. *Geophys. Res. Lett.*, **30 (14)**, 1732, doi:10.1029/2003GL017410.

DeMott, P. J., D. C. Rogers, S. M. Kreidenweis, Y. Chen, C. H. Twohy, D. Baumgardner, A. J. Heymsfield, and K. R. Chan, 1998: The role of heterogeneous freezing nucleation in upper tropospheric clouds: Inferences from SUCCESS. *Geophys. Res. Lett.*, **25 (9)**, 1387–1390, doi:10.1029/97GL03779.

DeMott, P. J., K. Sassen, M. R. Poellot, D. Baumgardner, D. C. Rogers, S. D. Brooks, A. J. Prenni, and S. M. Kreidenweis, 2003: African dust aerosols as atmospheric ice nuclei. *Geophys. Res. Lett.*, **30 (14)**, 26–29, doi:10.1029/2003GL017410.

Deschamps, P.-Y., F.-M. Breon, M. Leroy, A. Podaire, A. Bricaud, J.-C. Buriez, and G. Seze, 1994: The POLDER mission: Instrument characteristics and scientific objectives. *IEEE Trans. Geosci. and Remote Sens.*, **32 (3)**, 598–615, doi:10.1109/36.297978.

Desmons, M., N. Ferlay, F. Parol, L. Mcharek, and C. Vanbauce, 2013: Improved information about the vertical location and extent of monolayer clouds from POLDER3 measurements in the oxygen A-band. *Atmos. Meas. Tech.*, **6 (8)**, 2221–2238, doi:10.5194/amt-6-2221-2013.

Di Pierro, M., L. Jaeglé, E. W. Eloranta, and S. Sharma, 2013: Spatial and seasonal distribution of Arctic aerosols observed by the CALIOP satellite instrument (20062012). *Atmos. Chem. Phys.*, **13 (14)**, 7075–7095, doi:10.5194/acp-13-7075-2013.

Dimitriades, B., and M. Whisman, 1971: Carbon monoxide in lower atmosphere Reactions. *Environ. Sci. Technol.*, **5 (11)**, 1140–1141.

Djikaev, Y. S., and E. Ruckenstein, 2008: Thermodynamics of heterogeneous crystal nucleation in contact and immersion modes. *J. Phys. Chem.*, **112 (46)**, 11 677–11 687, doi:10.1021/jp803155f.

Dong, X., B. Xi, K. Crosby, C. N. Long, R. S. Stone, and M. D. Shupe, 2010: A 10 year climatology of Arctic cloud fraction and radiative forcing at Barrow, Alaska. *J. Geophys. Res.*, **115**, 1–14, doi:10.1029/2009JD013489.

Doutriaux-Boucher, M., and J. Quaas, 2004: Evaluation of cloud thermodynamic phase parametrizations in the LMDZ GCM by using POLDER satellite Data. *Geophys. Res. Lett.*, **31 (L06126)**, doi:10.1029/2003GL019095.

Durkee, P. A., and Coauthors, 2000: The impact of ship-produced aerosols on the microstructure and albedo of warm marine stratocumulus clouds: A test of MAST hypotheses 1i and 1ii. *J. Atmos. Sci.*, **57 (16)**, 2554–2569.

Dusek, U., and Coauthors, 2006: Size matters more than chemistry for cloud-nucleating ability of aerosol particles. *Science*, **312 (5778)**, 1375–1378, doi:10.1126/science.1125261.

Earle, M. E., P. S. K. Liu, J. W. Strapp, A. Zelenyuk, D. Imre, G. M. McFarquhar, N. C. Shantz, and W. R. Leaitch, 2011: Factors influencing the microphysics and radiative properties of liquid-dominated Arctic clouds: Insight from observations of aerosol and clouds during ISDAC. *J. Geophys. Res.*, **116**, D00T09, doi:10.1029/2011JD015887.

Eckhardt, S., and Coauthors, 2015: Current model capabilities for simulating black carbon and sulfate concentrations in the Arctic atmosphere: A multi-model evaluation using a comprehensive measurement data set. *Atmos. Chem. Phys.*, **15 (16)**, 9413–9433, doi:10.5194/acp-15-9413-2015.

Edwards, D. P., and Coauthors, 2004: Observations of carbon monoxide and aerosols from the Terra satellite: Northern Hemisphere variability. *J. Geophys. Res.*, **109**, 1–17, doi:10.1029/2004JD004727.

Ervens, B., M. Cubison, E. Andrews, G. Feingold, J. a. Ogren, J. L. Jimenez, P. DeCarlo, and A. Nenes, 2007: Prediction of cloud condensation nucleus number concentration using measurements of aerosol size distributions and composition and light scattering enhancement due to humidity. *J. Geophys. Res.: Atmos.*, **112 (10)**, 1–15, doi:10.1029/2006JD007426.

Feingold, G., 2003a: First measurements of the Twomey indirect effect using ground-based remote sensors. *Geophys. Res. Lett.*, **30 (6)**, 19–22, doi:10.1029/2002GL016633.

Feingold, G., 2003b: Modeling of the first indirect effect: Analysis of measurement requirements. *Geophys. Res. Lett.*, **30 (19)**, doi:10.1029/2003GL017967.

Feingold, G., L. A. Remer, J. Ramaprasad, and Y. J. Kaufman, 2001: Analysis of smoke impact on clouds in Brazilian biomass burning regions: An extension of Twomey ' s approach. *J. Geophys. Res.*, **106**, 22 907–22 922.

Finch, D. P., P. I. Palmer, and M. Parrington, 2014: Origin, variability and age of biomass burning plumes intercepted during BORTAS-B. *Atmos. Chem. Phys.*, **14 (24)**, 13 789–13 800, doi:10.5194/acp-14-13789-2014 .

Fisher, J. A., and Coauthors, 2010: Source attribution and interannual variability of Arctic pollution in spring constrained by aircraft (ARCTAS, ARCPAC) and satellite (AIRS) observations of carbon monoxide. *Atmos. Chem. Phys.*, **9 (5)**, 19 035–19 080, doi:10.5194/acpd-9-19035-2009.

Fletcher, N. H., E. G. Bowen, and P. Squires, 1962: *The Physics of Rainclouds*. Cambridge University Press, 386 pp.

Fougnie, B., G. Bracco, B. Lafrance, C. Ruffel, O. Hagolle, and C. Tinel, 2007: PARASOL in-flight calibration and performance. *Appl. Opt.*, **46**, 5435–5451, doi:10.1364/AO.46.005435.

Fromm, M., 2005: Pyro-cumulonimbus injection of smoke to the stratosphere: Observations and impact of a super blowup in northwestern Canada on 34 August 1998. *J. Geophys. Res.*, **110 (D8)**, D08 205, doi:10.1029/2004JD005350.

Fukuta, N., and B. Mason, 1963: Epitaxial growth of ice on organic crystals. *J. Phys. Chem. Solids*, **24 (6)**, 715–718, doi:10.1016/0022-3697(63)90217-8.

Garrett, T. J., L. Avey, P. I. Palmer, A. Stohl, J. A. Neuman, C. a. Brock, T. B. Ryerson, and J. S. Holloway, 2006: Quantifying wet scavenging processes in aircraft observations of nitric acid and cloud condensation nuclei. *J. Geophys. Res.: Atmos.*, **111 (23)**, 1–12, doi:10.1029/2006JD007416.

Garrett, T. J., S. Brattström, S. Sharma, D. E. J. Worthy, and P. Novelli, 2011: The role of scavenging in the seasonal transport of black carbon and sulfate to the Arctic. *Geophys. Res. Lett.*, **38 (L16805)**, doi:10.1029/2011GL048221.

Garrett, T. J., M. M. Maestas, S. K. Krueger, and C. T. Schmidt, 2009: Acceleration by aerosol of a radiative-thermodynamic cloud feedback influencing Arctic surface warming. *Geophys. Res. Lett.*, **36 (19)**, 10–13, doi:10.1029/2009GL040195.

Garrett, T. J., L. F. Radke, and P. V. Hobbs, 2002: Aerosol effects on cloud emissivity and surface longwave heating in the arctic. *J. Atmos. Sci.*, **59**, 769–778.

Garrett, T. J., and C. Zhao, 2006: Increased Arctic cloud longwave emissivity associated with pollution from mid-latitudes. *Nature*, **440 (7085)**, 787–789, doi:10.1038/nature04636.

Garrett, T. J., C. Zhao, X. Dong, G. G. Mace, and P. V. Hobbs, 2004: Effects of varying aerosol regimes on low-level Arctic stratus. *Geophys. Res. Lett.*, **31 (17)**, L17 105, doi:10.1029/2004GL019928.

Garrett, T. J., C. Zhao, and P. C. Novelli, 2010: Assessing the relative contributions of transport efficiency and scavenging to seasonal variability in Arctic aerosol. *Tellus, Ser. B*, **62 (3)**, 190–196, doi:10.1111/j.1600-0889.2010.00453.x.

Gayet, J.-F., G. Mioche, A. Dörnbrack, A. Ehrlich, A. Lampert, and M. Wendisch, 2009: Microphysical and optical properties of Arctic mixed-phase clouds the 9 April 2007 case study. *Atmos. Chem. Phys.*, **9 (3)**, 11 333–11 366, doi:10.5194/acpd-9-11333-2009.

Ghan, S. J., G. Guzman, and H. Abdul-Razzak, 1998: Competition between sea salt and sulfate particles as cloud condensation nuclei. *J. Atmos. Sci.*, **55 (22)**, 3340–3347.

Goody, R. M., and Y. L. Yung, 1995: *Atmospheric Radiation: Theoretical Basis*. Oxford Univ. Press, 519 pp.

Gryspeerdt, E., J. Quaas, and N. Bellouin, 2016: Constraining the aerosol influence on cloud fraction. *J. Geophys. Res.: Atmos.*, **121 (7)**, 3566–3583, doi:10.1002/2015JD023744.

Gultepe, I., G. A. Isaac, W. R. Leaitch, and C. M. Banic, 1996: Parameterizations of marine stratus microphysics based on in situ observations: Implications for GCMS. *J. Climate*, **9 (2)**, 345–357.

Gurganus, C. W., J. C. Charnawskas, A. B. Kostinski, and R. A. Shaw, 2014: Nucleation at the contact line observed on nanotextured surfaces. *Phys. Rev. Lett.*, **113 (23)**, 235 701, doi:10.1103/PhysRevLett.113.235701.

Hammersley, J. M., and D. C. Handscomb, 1964: *The General Nature of Monte Carlo Methods - Monte Carlo Methods*. Springer n ed., 1–9 pp.

Han, Q., J. Chou, and R. M. Welch, 1998: Global variation of column droplet concentration in low-level clouds. *Geophys. Res. Lett.*, **25 (9)**, 1419–1422.

Hansen, J. E., and L. D. Travis, 1974: Light scattering in planetary atmospheres. *Space-Sci. Rev.*, **16 (1957)**, 527–610.

Hartmann, D. L., M. E. Ockert-Bell, and M. L. Michelsen, 1992: The effect of cloud type on Earth's energy balance: Global analysis. *J. Climate*, **5 (11)**, 1281–1304.

Hassol, S., 2004: *Impacts of a Warming Arctic-Arctic Climate Impact Assessment*. Cambridge University Press, 135 pp.

Haywood, J., and O. Boucher, 2000: Estimates of the direct and indirect radiative forcing due to tropospheric aerosols: A review. *Reviews of Geophysics*, **38 (4)**, 513–543, doi: 10.1029/1999RG000078.

Hegg, D. A., D. S. Covert, M. J. Rood, and P. V. Hobbs, 1996: Measurements of aerosol optical properties in marine air. *J. Geophys. Res.*, **101 (D8)**, 12 893–12 903.

Heist, R. H., and H. Reiss, 1973: Investigation of the homogeneous nucleation of water vapor using a diffusion cloud chamber. *The journal of Chemical Physics*, **59 (2)**, 665–671.

Held, I. M., and B. J. Soden, 2000: Water vapor feedback and global warming 1. *Annu. Rev. Energy*, **25 (1)**, 441–475.

Herman, B. M., and S. R. Browning, 1965: A numerical solution to the equation of radiative transfer. *J. Atmos. Sci.*, **22 (5)**, 559–566.

Hewson, E. W., and R. W. Longley, 1944: *Meteorology, Theoretical and Applied*. J. Wiley & sons, inc.; Chapman & Hall, 484 pp.

Heymsfield, A. J., L. M. Miloshevich, C. Schmitt, A. Bansemer, C. Twohy, M. R. Poellot, A. Fridlind, and H. Gerber, 2005: Homogeneous ice nucleation in subtropical and tropical convection and its influence on cirrus anvil microphysics. *J. Atmos. Sci.*, **62 (1)**, 41–64, doi: 10.1175/JAS-3360.1.

Hirdman, D., and Coauthors, 2010: Source identification of short-lived air pollutants in the Arctic using statistical analysis of measurement data and particle dispersion model output. *Atmos. Chem. Phys.*, **9**, 19 879–19 937, doi:10.5194/acpd-9-19879-2009.

Hobbs, P. V., T. J. Garrett, R. J. Ferek, S. R. Strader, D. A. Hegg, G. M. Frick, and C. O'Dowd, 2000: Emissions from ships with respect to their effects on clouds. *J. Atmos. Sci.*, **57 (16)**, 2570–2590, doi:9.

Hobbs, P. V., and J. Locatelli, 1969: Ice nuclei from a natural forest fire. *J. Appl. Meteor.*, **8 (5)**, 833–834.

Holzer, M., T. M. Hall, and R. B. Stull, 2005: Seasonality and weather & driven variability of transpacific transport. *J. Geophys. Res.*, **110 (23103)**, 1–22, doi:10.1029/2005JD006261.

Hu, Y., S. Rodier, K.-m. Xu, W. Sun, J. Huang, B. Lin, P. Zhai, and D. Josset, 2010: Occurrence, liquid water content, and fraction of supercooled water clouds from combined CALIOP/IIR/MODIS measurements. *J. Geophys. Res.*, **115 (19)**, D00H34, doi:10.1029/2009JD012384.

Hu, Y., D. Winker, M. Vaughan, B. Lin, A. Omar, C. Trepte, and R. Holz, 2009: CALIPSO/CALIOP cloud phase discrimination algorithm. *Journal of Atmospheric and Oceanic Technology*, **26 (11)**, 2293–2309, doi:10.1175/2009JTECHA1280.1.

Huber, P. J., 1973: The 1972 Wald Memorial Lectures: Robust regression: Asymptotics, conjectures, and Monte Carlo. *The Annals of Statistics*, **1 (5)**, 799–821.

Huber, P. J., 2011: *Robust Statistics*. Wiley Series in Probability and Statistics, Springer, Chichester, UK, 511 pp.

Intrieri, J. M., 2002: An annual cycle of Arctic cloud characteristics observed by radar and lidar at SHEBA. *J. Geophys. Res.*, **107 (C10)**, 8030, doi:10.1029/2000JC000423.

IPCC, 1990: *Intergovernmental Panel On Climate. Climate Change 1990: The Physical Science Basis*. Cambridge University Press, 364 pp.

IPCC, 1996: *Intergovernmental Panel On Climate. Climate Change 1996: The Physical Science Basis*. Cambridge University Press, 572 pp.

IPCC, 2007: *Intergovernmental Panel On Climate. Climate Change 2007: The Physical Science Basis*. Cambridge University Press, 996 pp.

IPCC, 2013: *Climate Change 2014 Synthesis report Longer report*. Cambridge University Press, 1535 pp.

Jackson, R. C., and Coauthors, 2012: The dependence of ice microphysics on aerosol concentration in arctic mixed-phase stratus clouds during ISDAC and M-PACE. *J. Geophys. Res.*, **117 (D15)**, D15 207, doi:10.1029/2012JD017668.

Jeffery, C. A., and P. H. Austin, 1997: Homogeneous nucleation of supercooled water: Results from a new equation of state. *J. Geophys. Res.: Atmos.*, **102 (D21)**, 25 269–25 279, doi:10.1029/97JD02243.

Jiao, C., and M. G. Flanner, 2016: Changing black carbon transport to the Arctic from present day to the end of 21st century. *J. Geophys. Res.: Atmos.*, **121 (9)**, 4734–4750, doi:10.1002/2015JD023964.

Jourdan, O., and Coauthors, 2010: Coupling of the microphysical and optical properties of an Arctic nimbostratus cloud during the ASTAR 2004 experiment: Implications for light-scattering modeling. *J. Geophys. Res.* , **115 (D23)**, D23 206, doi:10.1029/2010JD014016.

Kahl, J. D., 1990: Characteristics of the low-level temperature inversion along the Alaskan Arctic coast. *International Journal of Climatology*, **10 (5)**, 537–548.

Kärcher, B., 2003: A parameterization of cirrus cloud formation: Heterogeneous freezing. *J. Geophys. Res.*, **108 (D14)**, 4402, doi:10.1029/2002JD003220.

Kato, S., and Coauthors, 2006: Seasonal and interannual variations of top-of-atmosphere irradiance and cloud cover over polar regions derived from the CERES data set. *Geophys. Res. Lett.*, **33 (19)**, 1–5, doi:10.1029/2006GL026685.

Kaufman, Y. J., I. Koren, L. A. Remer, D. Rosenfeld, and Y. Rudich, 2005: The effect of smoke, dust, and pollution aerosol on shallow cloud development over the Atlantic Ocean. *Proc. Natl. Acad. Sci. U. S. A.*, **102**, 11 207–11 212, doi:10.1073/pnas.0505191102.

Kawamoto, K., T. Hayasaka, I. Uno, and T. Ohara, 2006: A correlative study on the relationship between modeled anthropogenic aerosol concentration and satellite-observed cloud properties over east Asia. *J. Geophys. Res.: Atmos.*, **111**, 1–7, doi:10.1029/2005JD006919.

Kay, J. E., and T. L'Ecuyer, 2013: Observational constraints on Arctic Ocean clouds and radiative fluxes during the early 21st century. *J. Geophys. Res.: Atmos.*, **118 (13)**, 7219–7236, doi:10.1002/jgrd.50489.

Kay, J. E., T. L'Ecuyer, A. Gettelman, G. Stephens, and C. O'Dell, 2008: The contribution of cloud and radiation anomalies to the 2007 Arctic sea ice extent minimum. *Geophys. Res. Lett.*, **35 (8)**, L08 503, doi:10.1029/2008GL033451.

Kellogg, W. W., 1975: Climatic feedback mechanisms involving the polar regions. *Climate of the Arctic*, 111–116.

Kim, B.-G., M. A. Miller, S. E. Schwartz, Y. Liu, and Q. Min, 2008: The role of adiabaticity in the aerosol first indirect effect. *J. Geophys. Res.: Atmos.*, **113 (D5)**, doi:10.1029/2007JD008961.

Kim, Y. J., B. G. Kim, M. Miller, Q. Min, and C. K. Song, 2012: Enhanced aerosol-cloud relationships in more stable and adiabatic clouds. *Asia-Pacific J. Atmos. Sci.*, **48 (3)**, 283–293, doi:10.1007/s13143-012-0028-0.

King, M. D., Y. J. Kaufman, W. P. Menzel, and D. Tanre, 1992: Remote sensing of cloud, aerosol, and water vapor properties from the moderate resolution imaging spectrometer (MODIS). *IEEE Trans. Geosci. and Remote Sens.*, **30 (1)**, 2–27, doi:10.1109/36.124212.

King, M. D., and S. Platnick, 2006: Collection 005 change summary for the MODIS cloud optical property (06 _ OD) Algorithm high impact change overview : Change details. *Terra*, **1 (May)**, 1–23.

Klein, S. A., and D. L. Hartmann, 1993: The seasonal cycle of low stratiform clouds. *J. Climate*, **6** doi:10.1175/1520-0442, 1587–1606.

Klein, S. A., and Coauthors, 2009: Intercomparison of model simulations of mixed-phase clouds observed during the ARM Mixed-Phase Arctic Cloud Experiment. I: single-layer cloud. *Quart. J. Roy. Meteor. Soc.*, **135 (641)**, 979–1002, doi:10.1002/qj.416.

Klimont, Z., S. J. Smith, and J. Cofala, 2013: The last decade of global anthropogenic sulfur dioxide: 20002011 emissions. *Environ. Res. Lett.*, **8 (1)**, 014 003, doi:10.1088/1748-9326/8/1/014003.

Klingebiel, M., A. de Lozar, R. Weigel, A. Roth, L. Schmidt, and S. Borrmann, 2015: Arctic low-level boundary layer clouds: In situ measurements and simulations of mono-and bimodal supercooled droplet size distributions at the top layer of liquid phase clouds. *Atmos. Chem. Phys*, **15**, 617–631.

Klonecki, A., P. Hess, L. Emmons, L. Smith, J. Orlando, and D. Blake, 2003: Seasonal changes in the transport of pollutants into the Arctic troposphere-model study. *J. Geophys. Res.*, **108 (D4)**, doi:10.1029/2002JD002199.

Koch, D., and J. Hansen, 2005: Distant origins of Arctic black carbon: A Goddard Institute for Space Studies ModelE experiment. *J. Geoph. Res.*, **110 (D04204)**, 1–14, doi:10.1029/2004JD005296.

Komurcu, M., and Coauthors, 2014: Intercomparison of the cloud water phase among global climate models. *J. Geophys. Res.: Atmos.*, **119 (6)**, 3372–3400, doi:10.1002/2013JD021119.

Kristjánsson, J. E., 2002: Studies of the aerosol indirect effect from sulfate and black carbon aerosols. *J. Geophys. Res.: Atmos.*, **107**, 1–19, doi:10.1029/2001JD000887.

Lamarque, J.-F., and Coauthors, 2010: Historical (1850–2000) gridded anthropogenic and biomass burning emissions of reactive gases and aerosols: Methodology and application. *Atmos. Chem. Phys.*, **10 (15)**, 7017–7039, doi:10.5194/acp-10-7017-2010.

Lamb, D., and J. Verlinde, 2011: *Physics and Chemistry of Clouds*. Cambridge University Press, 584 pp.

Lance, S., and Coauthors, 2011: Cloud condensation nuclei as a modulator of ice processes in Arctic mixed-phase clouds. *Atmos. Chem. Phys*, **11** doi:10.5194/acp-11-8003-2011, 8003–8015.

Lathem, T. L., and Coauthors, 2013: Analysis of CCN activity of Arctic aerosol and Canadian biomass burning during summer 2008. *Atmos. Chem. Phys.*, **13 (5)**, 2735–2756, doi:10.5194/acp-13-2735-2013.

Law, K. S., and A. Stohl, 2007: Arctic air pollution: Origins and impacts. *Science*, **315 (5818)**, 1537–1540, doi:10.1126/science.1137695.

Law, K. S., and Coauthors, 2014: Arctic air pollution: New insights from POLARCAT-IPY. *Bull. Amer. Meteor. Soc.*, **95 (12)**, 1873–1895, doi:10.1175/BAMS-D-13-00017.1.

Le Houerou, H. N., 1996: Climate change, drought and desertification. *J. Arid Environ.*, **34 (2)**, 133–185.

Le Trent, H., and Z.-X. Li, 1991: Sensitivity of an atmospheric general circulation model to prescribed SST changes: Feedback effects associated with the simulation of cloud optical properties. *Climate Dyn.*, **5 (3)**, 175–187, doi:10.1007/BF00251808.

Lebsock, M. D., G. L. Stephens, and C. Kummerow, 2008: Multisensor satellite observations of aerosol effects on warm clouds. *J. Geophys. Res.*, **113 (D15)**, D15 205, doi:10.1029/2008JD009876.

L'Ecuyer, T. S., W. Berg, J. Haynes, M. Lebsock, and T. Takemura, 2009: Global observations of aerosol impacts on precipitation occurrence in warm maritime clouds. *J. Geophys. Res.*, **114 (D9)**, D09 211, doi:10.1029/2008JD011273.

Lee, S. S., and Coauthors, 2016: Effects of aerosol on evaporation, freezing and precipitation in a multiple cloud system. *Climate Dyn.*, 1–19, doi:10.1007/s00382-016-3128-1.

Leibowicz, B. D., D. S. Abbot, K. Emanuel, and E. Tziperman, 2012: Correlation between present-day model simulation of Arctic cloud radiative forcing and sea ice consistent with positive winter convective cloud feedback. *J. of Adv. in Model. Earth Syst.*, **4 (3)**, doi:10.1029/2012MS000153.

Lenoble, J., 1961: Application de la methode des harmoniques spheriques au cas de la diffusion anisotrope. *Comptes rendus hebdomadaires des seances de l'academie des Sciences*, **252 (14)**, 2087.

LeTreut, 2007: Historical overview of climate change. *Climate Change 2007: The Physical Science Basis*. Contribution of Working Group I to the Fourth Assessment Report of the Intergovernmental Panel on Climate Change, Cambridge University Press, 94–127.

Lihavainen, H., V. M. Kerminen, and L. A. Remer, 2009: Aerosol-cloud interaction determined by both in situ and satellite data over a northern high-latitude site. *Atmos. Chem. Phys.*, **10 (2003)**, 10 987–10 995, doi:10.5194/acp-10-10987-2010.

Lihavainen, H., and Coauthors, 2008: Measurements of the relation between aerosol properties and microphysics and chemistry of low level liquid water clouds in Northern Finland. *Atmos. Chem. Phys.*, **8 (23)**, 6925–6938, doi:10.5194/acp-8-6925-2008.

Lin, R.-F., D. O. Starr, P. J. DeMott, R. Cotton, K. Sassen, E. Jensen, B. Kärcher, and X. Liu, 2002: Cirrus Parcel Model Comparison Project. Phase 1: The critical components to simulate cirrus initiation explicitly. *J. Atmos. Sci.*, **59 (15)**, 2305–2329.

Lindholt, L., and S. Glomsrød, 2012: The Arctic: No big bonanza for the global petroleum industry. *Energy Economics*, **34 (5)**, 1465–1474, doi:10.1016/j.eneco.2012.06.020.

Liu, Y., and J. R. Key, 2014: Less winter cloud aids summer 2013 Arctic sea ice return from 2012 minimum. *Environ. Res. Lett.*, **9**, 44 002, doi:10.1088/1748-9326/9/4/044002.

Loeb, N. G., B. A. Wielicki, D. R. Doelling, G. L. Smith, D. F. Keyes, S. Kato, M.-S. Natividad, and T. Wong, 2009: Toward optimal closure of the Earth's top-of-atmosphere radiation budget. *J. Climate*, **22 (33)**, 748–766, doi:10.1175/2008JCLI2637.1.

Lohmann, U., and J. Feichter, 2004: Global indirect aerosol effects: A review. *Atmos. Chem. Phys.*, **4 (6)**, 7561–7614, doi:10.5194/acpd-4-7561-2004.

Longley, I. D., D. W. F. Inglis, M. W. Gallagher, P. I. Williams, J. D. Allan, and H. Coe, 2005: Using NOx and CO monitoring data to indicate fine aerosol number concentrations and emission factors in three UK conurbations. *Atmos. Environ.*, **39 (x)**, 5157–5169, doi:10.1016/j.atmosenv.2005.05.017.

Lu, M.-L., W. C. Conant, H. H. Jonsson, V. Varutbangkul, R. C. Flagan, and J. H. Seinfeld, 2007: The Marine Stratus/Stratocumulus Experiment (MASE): Aerosol-cloud relationships in marine stratocumulus. *J. Geophys. Res.*, **112 (D10)**, D10 209, doi:10.1029/2006JD007985.

Lu, M.-L., G. Feingold, H. H. Jonsson, P. Y. Chuang, H. Gates, R. C. Flagan, and J. H. Seinfeld, 2008: Aerosol-cloud relationships in continental shallow cumulus. *J. Geophys. Res.*, **113 (D15)**, D15 201, doi:10.1029/2007JD009354.

Lubin, D., and A. M. Vogelmann, 2006: A climatologically significant aerosol longwave indirect effect in the Arctic. *Nature*, **439 (January)**, 453–456, doi:10.1038/nature04449.

Lubin, D., and A. M. Vogelmann, 2007: Expected magnitude of the aerosol shortwave indirect effect in springtime Arctic liquid water clouds. *Geophys. Res. Lett.*, **34 (11)**, L11 801, doi:10.1029/2006GL028750.

Luo, C., 2003: Sensitivity study of meteorological parameters on mineral aerosol mobilization, transport, and distribution. *J. Geophys. Res.*, **108 (D15)**, 4447, doi: 10.1029/2003JD003483.

Madonna, L. A., C. M. Sciulli, L. N. Canjar, and G. M. Pound, 1961: Low temperature cloud chamber studies on water vapour. *Proc. Phys. Soc.*, **78 (6)**, 1218.

Mao, J., and Coauthors, 2010: Chemistry of hydrogen oxide radicals (HO x) in the Arctic troposphere in spring. *Atmos. Chem. Phys.*, **10 (13)**, 5823–5838, doi:10.5194/acp-10-5823-2010.

Marelle, L., and Coauthors, 2015: Transport of anthropogenic and biomass burning aerosols from Europe to the Arctic during spring 2008. *Atmos. Chem. Phys.*, **15 (7)**, 3831–3850, doi:10.5194/acp-15-3831-2015.

Markus, T., J. C. Stroeve, and J. Miller, 2009: Recent changes in Arctic sea ice melt onset, freezeup, and melt season length. *J. Geophys. Res.: Oceans*, **114 (12)**, 1–14, doi: 10.1029/2009JC005436.

Martin, G. M., D. W. Johnson, and A. Spice, 1994: The measurement and parameterization of effective radius of droplets in warm stratocumulus clouds. *J. Atmos. Sci.*, **51 (13)**, 1823–1842.

Mason, B. J., 1961: The growth of snow crystals. *Sci. Amer.*, **204**, 120–133.

Matsui, T., H. Masunaga, S. M. Kreidenweis, R. a. Pielke, W. K. Tao, M. Chin, and Y. J. Kaufman, 2006: Satellite-based assessment of marine low cloud variability associated with aerosol, atmospheric stability, and the diurnal cycle. *J. Geophys. Res.: Atmos.*, **111 (October)**, 1–16, doi:10.1029/2005JD006097.

Mauger, G. S., and J. R. Norris, 2007: Meteorological bias in satellite estimates of aerosol-cloud relationships. *Geophys. Res. Lett.*, **34 (August 2007)**, 1–5, doi:10.1029/2007GL029952.

Mauritsen, T., and Coauthors, 2011: An Arctic CCN-limited cloud-aerosol regime. *Atmos. Chem. Phys*, **11** doi:10.5194/acp-11-165-2011, 165–173.

McComiskey, A., and G. Feingold, 2012: The scale problem in quantifying aerosol indirect effects. *Atmos. Chem. Phys.*, **12 (2)**, 1031–1049, doi:10.5194/acp-12-1031-2012.

McComiskey, A., G. Feingold, A. S. Frisch, D. D. Turner, M. A. Miller, J. C. Chiu, Q. Min, and J. A. Ogren, 2009: An assessment of aerosol cloud interactions in marine stratus clouds based on surface remote sensing. *J. Geophys. Res.*, **114 (D9)**, D09 203, doi: 10.1029/2008JD011006.

McCoy, D. T., and D. L. Hartmann, 2015: Observations of a substantial cloud-aerosol indirect effect during the 2014-2015 Bárarbunga-Veiivötn fissure eruption in Iceland. *Geophys. Res. Lett.*, **42 (23)**, 10,409–10,414, doi:10.1002/2015GL067070.

McFarquhar, G. M., and A. J. Heymsfield, 2001: Parameterizations of INDOEX microphysical measurements and calculations of cloud susceptibility: Applications for climate studies. *J. Geophys. Res.*, **106 (D22)**, 28 675, doi:10.1029/2000JD900777.

McFarquhar, G. M., and Coauthors, 2011: Indirect and semi-direct aerosol campaign. *Bull. Amer. Meteor. Soc.*, **92 (2)**, 183–201, doi:10.1175/2010BAMS2935.1.

Miller, A. W., and G. M. Ruiz, 2014: Arctic shipping and marine invaders. *Nat. Climate Change*, **4 (6)**, 413–416, doi:http://dx.doi.org/10.1038/nclimate2244.

Mioche, G., O. Jourdan, M. Ceccaldi, and J. Delanoë, 2014: Variability of the mixed phase in the Arctic with a focus on the Svalbard region: A study based on spaceborne active remote sensing. *Atmos. Chem. Phys.*, **14 (16)**, 23 453–23 497, doi:10.5194/acpd-14-23453-2014.

Monks, S. A., S. R. Arnold, and M. P. Chipperfield, 2012: Evidence for El Nino-Southern Oscillation (ENSO) influence on Arctic CO interannual variability through biomass burning emissions. *Geophys. Res. Lett.*, **39 (14)**, doi:10.1029/2012GL052512.

Monks, S. A., and Coauthors, 2015: Multi-model study of chemical and physical controls on transport of anthropogenic and biomass burning pollution to the Arctic. *Atmos. Chem. Phys.*, **15**, 3575–3603, doi:10.5194/acp-15-3575-2015.

Myhre, G., and Coauthors, 2006: Aerosol-cloud interaction inferred from MODIS satellite data and global aerosol models. *Atmos. Chem. Phys.*, **6 (5)**, 9351–9388, doi:10.5194/acpd-6-9351-2006.

Nakajima, T., A. Higurashi, K. Kawamoto, and J. E. Penner, 2001: A possible correlation between satellite-derived cloud and aerosol microphysical parameters. *Geophys. Res. Lett.*, **28 (7)**, 1171–1174, doi:10.1029/2000GL012186.

Nakicenovic, N., J. Alcamo, G. Davis, B. De Vries, J. Fenhann, S. Gaffin, and E. Lebre, 2000: *Emissions scenarios*. Cambridge University Press, 608 pp.

Niehaus, J., and W. Cantrell, 2015: Contact freezing of water by salts. *J. Phys. Chem. Lett.*, **6 (17)**, 3490–3495, doi:10.1021/acs.jpclett.5b01531.

Niemand, M., and Coauthors, 2012: A particle-surface-area-based parameterization of immersion freezing on desert dust particles. *J. Atmos. Sci.*, **69 (10)**, 3077–3092, doi:10.1175/JAS-D-11-0249.1.

Novelli, P. C., and K. A. Masarie, 2014: Atmospheric carbon monoxide dry air mole fractions from the NOAA ESRL Carbon Cycle Cooperative Global Air Sampling Network, 1988 2013.

Nygärd, T., T. Valkonen, and T. Vihma, 2014: Characteristics of arctic low-tropospheric humidity inversions based on radio soundings. *Atmos. Chem. Phys.*, **14 (4)**, 1959–1971, doi:10.5194/acp-14-1959-2014.

Ødemark, K., S. B. Dalsøren, B. H. Samset, T. K. Berntsen, J. S. Fuglestvedt, and G. Myhre, 2012: Short-lived climate forcers from current shipping and petroleum activities in the Arctic. *Atmos. Chem. Phys.*, **12 (4)**, 1979–1993, doi:10.5194/acp-12-1979-2012.

O'Dowd, C. D., J. A. Lowe, M. H. Smith, and A. D. Kaye, 1999: The relative importance of non-sea-salt sulphate and sea-salt aerosol to the marine cloud condensation nuclei population: An improved multi-component aerosol-cloud droplet parametrization. *Quart. J. Roy. Meteor. Soc.*, **125 (556)**, 1295–1313, doi:10.1002/qj.1999.49712555610.

Overland, J. E., and M. Wang, 2013: When will the summer Arctic be nearly sea ice free? *Geophys. Res. Lett.*, **40 (February)**, 2097–2101, doi:10.1002/grl.50316.

Painemal, D., S. Kato, and P. Minnis, 2014: Boundary layer regulation in the southeast Atlantic cloud microphysics during the biomass burning season as seen by the A-train satellite constellation. *J. Geophys. Res.: Atmos.*, doi:10.1002/2014JD022182.

Painemal, D., and P. Zuidema, 2013: The first aerosol indirect effect quantified through airborne remote sensing during VOCALS-REx. *Atmos. Chem. Phys.*, **13 (2)**, 917–931, doi:10.5194/acp-13-917-2013.

Pandis, S. N., L. M. Russell, and J. H. Seinfeld, 1994: The relationship between DMS flux and CCN concentration in remote marine regions. *J. Geophys. Res.: Atmos.*, **99 (D8)**, 16 945–16 957.

Paris, J.-D., and Coauthors, 2009: Wildfire smoke in the Siberian Arctic in summer: Source characterization and plume evolution from airborne measurements. *Atmos. Chem. Phys.*, **9 (5)**, 18 201–18 233, doi:10.5194/acpd-9-18201-2009.

Parkinson, C. L., D. J. Cavalieri, P. Gloersen, H. J. Zwally, and J. C. Comiso, 1999: Arctic sea ice extents, areas, and trends, 1978-1996. *J. Geophys. Res.*, **104 (20)**, 837–856.

Parrington, M., and Coauthors, 2012: The influence of boreal biomass burning emissions on the distribution of tropospheric ozone over North America and the North Atlantic during 2010. *Atmos. Chem. Phys.*, **12 (4)**, 2077–2098, doi:10.5194/acp-12-2077-2012.

Paukert, M., and C. Hoose, 2014: Modeling immersion freezing with aerosol-dependent prognostic ice nuclei in Arctic mixed-phase clouds. *J. Geophys. Res.: Atmos.*, **119 (14)**, 9073–9092, doi:10.1002/2014JD021917.

Pearl, J., 1994: A probabilistic calculus of actions. *Proceedings of the Tenth International Conference on Uncertainty in Artificial Intelligence*, Morgan Kaufmann Publishers Inc., 454–462.

Perovich, D., T. Grenfell, B. Light, and P. Hobbs, 2002: Seasonal evolution of the albedo of multiyear Arctic sea ice. *J. Geophys. Res.: Oceans*, **107 (C10)**.

Peters, G. P., T. B. Nilssen, L. Lindholt, M. S. Eide, S. Glomsrød, L. I. Eide, and J. S. Fuglestvedt, 2011: Future emissions from shipping and petroleum activities in the Arctic. *Atmos. Chem. Phys.*, **11 (11)**, 5305–5320, doi:10.5194/acp-11-5305-2011.

Petty, G. W., 2006: *A First Course in Atmospheric Radiation*. Sundog Pub., 459 pp.

Phillips, V. T., P. J. DeMott, and C. Andronache, 2008: An empirical parameterization of heterogeneous ice nucleation for multiple chemical species of aerosol. *J. Atmos. Sci.*, **65 (9)**, 2757–2783, doi:10.1175/2007JAS2546.1.

Pincus, R., and M. B. Baker, 1994: Effect of precipitation on the albedo susceptibility of clouds in the marine boundary layer. *Nature*, **372 (6503)**, 250–252, doi:10.1038/372250a0.

Pithan, F., and T. Mauritsen, 2014: No Title. *Nat. Geosci.*, **7 (3)**, 181–184, doi:10.1038/ngeo2071.

Pizzolato, L., S. E. L. Howell, C. Derksen, J. Dawson, and L. Copland, 2014: Changing sea ice conditions and marine transportation activity in Canadian Arctic waters between 1990 and 2012. *Climatic Change*, **123 (2)**, 161–173, doi:10.1007/s10584-013-1038-3.

Platnick, S., M. D. King, S. A. Ackerman, W. P. Menzel, B. A. Baum, J. C. Riédi, and R. A. Frey, 2003: The MODIS cloud products: Algorithms and examples from terra. *IEEE Trans. Geosci. and Remote Sens.*, **41 (2)**, 459–472, doi:10.1109/TGRS.2002.808301.

Platnick, S., J. Y. Li, M. D. King, H. Gerber, and P. V. Hobbs, 2001: A solar reflectance method for retrieving the optical thickness and droplet size of liquid water clouds over snow and ice surfaces. *J. Geophys. Res.*, **106 (D14)**, 15 185, doi:10.1029/2000JD900441.

Platnick, S., and Coauthors, 2014: MODIS cloud optical properties: User guide for the collection 6 Level-2 MOD06/MYD06 product and associated Level-3 datasets. *Version 0.9 (beta)*, **17**.

Popovitz-Biro, R., J. L. Wang, J. Majewski, E. Shavit, L. Leiserowitz, and M. Lahav, 1994: Induced freezing of supercooled water into ice by self-assembled crystalline monolayers of amphiphilic alcohols at the air-water interface. *J. Amer. Chem. Soc.*, **116 (4)**, 1179–1191, doi:10.1021/ja00083a003.

Provost, C., and Coauthors, 2015: IAOOS (Ice-Atmosphere-Arctic Ocean Observing System, 2011-2019). *Mercator Ocean Quart. Newsl.*, **(51)**, 13–15.

Pruppacher, H. R., 1995: A New Look at Homogeneous Ice Nucleation in Supercooled Water Drops. *J. Atmos. Sci.*, **52 (11)**, 1924–1933.

Pruppacher, H. R., and J. D. Klett, 1997: *Microphysics of Clouds and Precipitation*. Kluwer Academic Publishers, 714 pp.

Pueschel, R. F., and G. Langer, 1973: Sugar cane fires as a source of ice nuclei in Hawaii. *J. Appl. Meteor.*, **12 (3)**, 549–551.

Qiu, S., X. Dong, B. Xi, and J. F. Li, 2015: Characterizing Arctic mixed-phase cloud structure and its relationship with humidity and temperature inversion using ARM NSA observations. *J. Geophys. Res.*, 1–10, doi:10.1002/2014JD023022.Received.

Qu, X., and A. Hall, 2005: Surface contribution to planetary albedo variability in cryosphere regions. *J. Climate*, **18 (24)**, 5239–5252.

Quaas, J., 2004: Aerosol indirect effects in POLDER satellite data and the Laboratoire de Meteorologie DynamiqueZoom (LMDZ) general circulation model. *J. Geophys. Res.*, **109 (D8)**, D08 205, doi:10.1029/2003JD004317.

Quaas, J., O. Boucher, and U. Lohmann, 2005: Constraining the total aerosol indirect effect in the LMDZ and ECHAM4 GCMs using MODIS satellite data. *Atmos. Chem. Phys.*, **5 (5)**, 9669–9690, doi:10.5194/acpd-5-9669-2005.

Quinn, P. K., T. S. Bates, D. J. Coffman, and D. S. Covert, 2007a: Influence of particle size and chemistry on the cloud nucleating properties of aerosols. *Atmos. Chem. Phys.*, **7 (5)**, 14 171–14 208, doi:10.5194/acpd-7-14171-2007.

Quinn, P. K., T. L. Miller, T. S. Bates, J. A. Ogren, E. Andrews, and G. E. Shaw, 2002: A 3-year record of simultaneously measured aerosol chemical and optical properties at Barrow, Alaska. *J. Geophys. Res.*, **107 (D11)**.

Quinn, P. K., G. Shaw, E. Andrews, E. G. Dutton, T. Ruoho-Airola, and S. L. Gong, 2007b: Arctic haze: Current trends and knowledge gaps. *Tellus, Ser. B*, **59**, 99–114, doi: 10.1111/j.1600-0889.2006.00238.x.

Radke, L. F., J. A. J. Coakley, and M. D. King, 1989: Direct and remote sensing observations of the effects of ships on clouds. *J. Appl. Meteor.*, **246**, 1146–1149.

Raga, G. B., and P. R. Jonas, 1993: On the link between cloudtop radiative properties and subcloud aerosol concentrations. *Quart. J. Roy. Meteor. Soc.*, **119 (514)**, 1419–1425.

Ramanathan, V., 2001: Aerosols, climate, and the hydrological cycle. *Science*, **294 (5549)**, 2119–2124, doi:10.1126/science.1064034.

Ramanathan, V., R. D. Cess, E. F. Harrison, P. Minnis, B. R. Barkstrom, E. Ahmad, and D. Hartmann, 1989: Cloud-radiative forcing and climate: Results from the Earth radiation budget experiment. *Science*, **243 (4887)**, 57–63, doi:10.1126/science.243.4887.57.

Ramanathan, V., and A. M. Vogelmann, 1997: Greenhouse effect, atmospheric solar absorption and the Earth's radiation budget: From the Arrhenius-Langley era to the 1990s. *Ambio*, 38–46.

Randall, D., and Coauthors, 1996: Status of and outlook for large-scale modeling of atmosphere-ice-ocean interactions in the Arctic. *Bull. Amer. Meteor. Soc.*, **79 (2)**, 197–219.

Rangno, A. L., and P. V. Hobbs, 2001: Ice particles in stratiform clouds in the Arctic and possible mechanisms for the production of high ice concentrations. *J. Geophys. Res.*, **106** doi: 10.1029/2000JD900286, 15,15–65,75.

Rasmussen, D. H., 1982: Ice formation in aqueous systems. *J. Microsc.*, **128 (2)**, 167–174.

Reuveny, R., 2007: Climate change-induced migration and violent conflict. *Political geography*, **26 (6)**, 656–673.

Richter-Menge, J., and M. Jeffries, 2011: State of the climate in 2010: The Arctic. *Bull. Amer. Meteor. Soc.*, **92 (6)**, S143–S160.

Riedi, J., and Coauthors, 2010: Cloud thermodynamic phase inferred from merged POLDER and MODIS data. *Atmos. Chem. Phys*, **10** doi:10.5194/acp-10-11851-2010, 11 851–11 865.

Robock, A., 1980: The seasonal cycle of snow cover, sea ice and surface albedo. *Mon. Wea. Rev.*, **108 (3)**, 267–285.

Rogers, D., P. DeMott, S. Kreidenweis, and Y. Chen, 1998: Measurements of ice nucleating aerosols during SUCCESS. *Geophys. Res. Lett.*, **25**, 1383–1386.

Rosenfeld, D., and W. L. Woodley, 2000: Deep convective clouds with sustained supercooled liquid water down to -37.5C. *Nature*, **405 (6785)**, 440–442.

Rossow, W. B., L. C. Garder, P. J. Lu, and A. Walker, 1991: International satellite cloud climatology project (ISCCP) documentation of cloud data. *WMO Tech. Doc.*, 76.

Sanderson, M. G., D. L. Hemming, and R. A. Betts, 2011: Regional temperature and precipitation changes under high-end ({>}=4 C) global warming. *Philos. Trans. Roy. Soc., A*, **369 (1934)**, 85–98, doi:10.1098/rsta.2010.0283.

Sarna, K., and H. W. J. Russchenberg, 2016: Ground based remote sensing scheme for monitoring aerosolcloud interactions. *Atmos. Meas. Tech.*, **9 (3)**, 1039–1050, doi:10.5194/amt-9-1039-2016.

Sassen, K., 2003: Saharan dust storms and indirect aerosol effects on clouds: CRYSTAL-FACE results. *Geophys. Res. Lett.*, **30 (12)**, 1–4, doi:10.1029/2003GL017371.

Sassen, K., P. J. DeMott, J. M. Prospero, and M. R. Poellot, 2003: Saharan dust storms and indirect aerosol effects on clouds: CRYSTAL-FACE results. *Geophys. Res. Lett.*, **30 (12)**, 1–4, doi:10.1029/2003GL017371.

Sassen, K., and G. C. Dodd, 1988: Homogeneous Nucleation Rate for Highly Supercooled Cirrus Cloud Droplets. *J. Atmos. Sci.*, **45 (8)**, 1357–1369.

Satheesh, S., and K. Krishnamoorthy, 2005: Radiative effects of natural aerosols: A review. *Atmos. Environ.*, **39 (11)**, 2089–2110, doi:10.1016/j.atmosenv.2004.12.029.

Schmidt, A., and Coauthors, 2015: Satellite detection, long-range transport, and air quality impacts of volcanic sulfur dioxide from the 20142015 flood lava eruption at Bárarbunga (Iceland). *J. Geophys. Res.: Atmos.*, **120**, 9739–9757, doi:10.1002/2015JD023638.

Schmidt, J., A. Ansmann, J. Bühl, H. Baars, U. Wandinger, D. Müller, and A. V. Malinka, 2014: Dual-FOV Raman and Doppler lidar studies of aerosol-cloud interactions: Simultaneous profiling of aerosols, warm-cloud properties, and vertical wind. *J. Geophys. Res.: Atmos.*, **119 (9)**, 5512–5527, doi:10.1002/2013JD020424.

Schwartz, S. E., Harshvardhan, and C. M. Benkovitz, 2002: Influence of anthropogenic aerosol on cloud optical depth and albedo shown by satellite measurements and chemical transport modeling. *Proc. Natl. Acad. Sci. U. S. A.*, **99**, 1784–1789, doi:10.1073/pnas.261712099.

Schweiger, A. J., and J. R. Key, 1994: Arctic Ocean radiative fluxes and cloud forcing estimated from the ISCCP C2 cloud dataset, 1983–1990. *J. Appl. Meteor.*, **33 (8)**, 948–963.

Schweiger, A. J., R. W. Lindsay, S. Vavrus, and J. A. Francis, 2008: Relationships between arctic sea ice and clouds during Autumn. *J. Climate*, **21 (18)**, 4799–4810, doi:10.1175/2008JCLI2156.1.

Screen, J. A., and I. Simmonds, 2010: The central role of diminishing sea ice in recent Arctic temperature amplification. *Nature*, **464 (7293)**, 1334–1337, doi:10.1038/nature09051.

Sekiguchi, M., 2003: A study of the direct and indirect effects of aerosols using global satellite data sets of aerosol and cloud parameters. *J. Geophys. Res.*, **108**, 1–15, doi:10.1029/2002JD003359.

Sena, E. T., A. Mccomiskey, G. Feingold, and C. S. Division, 2016: A long-term study of aerosolcloud interactions and their radiative effect at the Southern Great Plains using ground-based measurements. *Atmos. Chem. Phys.*, **16**, 11 301–11 318, doi:10.5194/acp-16-11301-2016.

Serreze, M. C., A. P. Barrett, J. C. Stroeve, D. N. Kindig, and M. M. Holland, 2009: The emergence of surface-based Arctic amplification. *The Cryosphere*, **3**, 11–19, doi:10.5194/tcd-2-601-2008.

Serreze, M. C., and R. G. Barry, 2011: Processes and impacts of Arctic amplification: A research synthesis. *Global and Planetary Change*, **77**, 85–96, doi:10.1016/j.gloplacha.2011.03.004.

Serreze, M. C., and J. A. Francis, 2006: The Arctic on the fast track of change. *Wea.*, **61**, 65–69, doi:10.1256/wea.197.05.

Serreze, M. C., M. M. Holland, and J. Stroeve, 2007: Perspectives on the Arctic's shrinking sea-ice cover. *Science*, **315 (5818)**, 1533–1536.

Shaw, G. E., 1982: Evidence for a central Eurasian source area of Arctic haze in Alaska. *Nature*, **299**, 815–818.

Shaw, G. E., 1995: The Arctic haze phenomenon. *Bull. Amer. Meteor. Soc.*, **76 (12)**, 2403–2413.

Shindell, D., 2007: Local and remote contributions to Arctic warming. *Geophys. Res. Lett.*, **34 (L14704)**, doi:10.1029/2007GL030221.

Shindell, D. T., G. Faluvegi, D. M. Koch, G. A. Schmidt, N. Unger, and S. E. Bauer, 2009: Improved attribution of climate forcing to emissions. *Science*, **326 (5953)**, 716–718.

Shindell, D. T., and Coauthors, 2008: A multi-model assessment of pollution transport to the Arctic. *Atmos. Chem. Phys*, **8**, 5353–5372.

Shindell, D. T., and Coauthors, 2013: Radiative forcing in the ACCMIP historical and future climate simulations. *Atmos. Chem. Phys.*, **13 (6)**, 2939–2974, doi:10.5194/acp-13-2939-2013.

Shupe, M. D., and J. M. Intrieri, 2004: Cloud radiative forcing of the Arctic surface: The influence of cloud properties, surface albedo, and solar zenith angle. *J. Climate*, **17 (3)**, 616–628.

Shupe, M. D., P. O. G. Persson, I. M. Brooks, M. Tjernström, J. Sedlar, T. Mauritsen, S. Sjogren, and C. Leck, 2013: Cloud and boundary layer interactions over the Arctic sea ice in late summer. *Atmos. Chem. Phys.*, **13 (18)**, 9379–9399, doi:10.5194/acp-13-9379-2013.

Singh, H. B., B. E. Anderson, W. H. Brune, C. Cai, R. C. Cohen, J. H. Crawford, and G. Huey, 2010: Pollution influences on atmospheric composition and chemistry at high northern latitudes: Boreal and California forest fire emissions. *Atmos. Environ.*, **44 (36)**, 455–4564.

Sirois, A., and L. A. Barrie, 1999: Arctic lower tropospheric aerosol trends and composition at Alert, Canada: 19801995. *J. Geophys. Res.*, **104**, 11 599, doi:10.1029/1999JD900077.

Slingo, A., 1990: Sensitivity of the Earth's radiation budget to changes in low clouds. *Nature*, **343**, 49–51.

Sodemann, H., and Coauthors, 2011: Episodes of cross-polar transport in the Arctic troposphere during July 2008 as seen from models, satellite, and aircraft observations. *Atmos. Chem. Phys*, **11** doi:10.5194/acp-11-3631-2011, 3631–3651.

Solomon, A., M. D. Shupe, P. O. G. Persson, and H. Morrison, 2011: Moisture and dynamical interactions maintaining decoupled Arctic mixed-phase stratocumulus in the presence of a humidity inversion. *Atmos. Chem. Phys.*, **11 (19)**, 10 127–10 148, doi:10.5194/acp-11-10127-2011.

Sporre, M. K., P. Glantz, P. Tunved, E. Swietlicki, M. Kulmala, and H. Lihavainen, 2012: A study of the indirect aerosol effect on subarctic marine liquid low-level clouds using MODIS cloud data and ground-based aerosol measurements. *Atmos. Res.*, **116**, 56–66, doi:10.1016/j.atmosres.2011.09.014.

Stein, O., M. Schultz, J. Flemming, A. Inness, J. Kaiser, L. Jones, and A. Benedetti, 2010: MACC Global air quality services technical documentation. *Simulation*, **(January 2006)**, 1–12.

Stephens, G. L., 2005: Cloud feedbacks in the climate system: A critical review. *J. Climate*, **18 (2)**, 237–273, doi:10.1175/JCLI-3243.1.

Stephens, G. L., and Coauthors, 2002: The cloudsat mission and the A-Train: A new dimension of space-based observations of clouds and precipitation. *Bull. Amer. Meteor. Soc.*, **83 (12)**, 1771–1790+1742, doi:10.1175/BAMS-83-12-1771.

Stevens, B., 2007: On the growth of layers of nonprecipitating cumulus convection. *J. Atmos. Sci.*, **72 (9)**, 2916–2931, doi:10.1175/JAS3983.1.

Stevens, B., and J.-L. Brenguier, 2009: *Clouds in the Perturbed Climate System, Their Relationship to Energy Balance, Atmospheric Dynamics, and Precipitation*. MIT Press, 576 pp.

Stevens, B., and G. Feingold, 2009: Untangling aerosol effects on clouds and precipitation in a buffered system. *Nature*, **461 (7264)**, 607–613, doi:10.1038/nature08281.

Stevens, B., and A. Seifert, 2008: Understanding macrophysical outcomes of microphysical choices in simulations of shallow cumulus convection. *J. Meteor. Soc. Japan*, **86**, 143–162.

Stevenson, D., and Coauthors, 2013: Tropospheric ozone changes, radiative forcing and attribution to emissions in the Atmospheric Chemistry and Climate Model. *Atmos. Chem. Phys.*, **13 (6)**, 3063–3085, doi:10.5194/acp-13-3063-2013.

Stohl, A., 2001: A 1-year Lagrangian climatology of airstreams in the northern hemisphere troposphere and lowermost stratosphere. *J. Geophys. Res.*, **106 (D7)**, 7263–7279.

Stohl, A., 2006: Characteristics of atmospheric transport into the Arctic troposphere. *J. Geophys. Res..*, **111 (D11306)**, doi:10.1029/2005JD006888.

Stohl, A., K. Baumann, G. Wotawa, M. Langer, B. Neininger, M. Piringer, and H. Formayer, 1997: Diagnostic downscaling of large-scale wind fields to compute local-scale trajectories. *J. Appl. Meteor.*, **36 (7)**, 931–942.

Stohl, A., C. Forster, H. Huntrieser, H. Mannstein, W. W. McMillan, A. Petzold, H. Schlager, and B. Weinzierl, 2007: Aircraft measurements over Europe of an air pollution plume from Southeast Asia; aerosol and chemical characterization. *Atmos. Chem. Phys.*, **6 (6)**, 12 611–12 670, doi:10.5194/acpd-6-12611-2006.

Stohl, A., A. Franck, P. Seibert, and G. Wotawa, 2005: Technical note: The lagrangian particle dispersion model FLEXPART version 6.2. *Atmos. Chem. Phys.*, doi:1680-7324/acp/2005-5-2461.

Stohl, A., M. Hittenberger, and G. Wotawa, 1998: Validation of the lagrangian particle dispersion model FLEXPART against large-scale tracer experiment data. *Atmos. Environ.*, **32 (24)**, 4245–4264, doi:10.1016/S1352-2310(98)00184-8.

Stohl, A., and P. James, 2005: A lagrangian analysis of the atmospheric branch of the global water cycle. Part II: Moisture transports between Earth's ocean basins and river catchments. *J. of Hydrometeor.*, **6 (6)**, 961–984, doi:10.1175/JHM470.1.

Stohl, A., Z. Klimont, S. Eckhardt, K. Kupiainen, V. P. Shevchenko, V. M. Kopeikin, and A. N. Novigatsky, 2013: Black carbon in the Arctic: the underestimated role of gas flaring and residential combustion emissions. *Atmos. Chem. Phys.*, **13 (17)**, 8833–8855, doi:10.5194/acp-13-8833-2013.

Stohl, A., and Coauthors, 2003: A backward modeling study of intercontinental pollution transport using aircraft measurements. *J. Geophys. Res.*, **108 (12)**, 4370.

Stohl, A., and Coauthors, 2006: Arctic smoke record high air pollution levels in the European Arctic due to agricultural fires in Eastern Europe. *Atmos. Chem. Phys.*, **6 (5)**, 9655–9722, doi:10.5194/acpd-6-9655-2006.

Stohl, A., and Coauthors, 2015: Evaluating the climate and air quality impacts of short-lived pollutants. *Atmos. Chem. Phys.*, **15 (11)**, 15 155–15 241, doi:10.5194/acpd-15-15155-2015.

Su, W., N. G. Loeb, K.-M. Xu, G. L. Schuster, and Z. A. Eitzen, 2010: An estimate of aerosol indirect effect from satellite measurements with concurrent meteorological analysis. *J. Geophys. Res.*, **115 (D18)**, D18 219, doi:10.1029/2010JD013948.

Symon, C., L. Arris, and B. Heal, 2004: *Arctic Climate Impact Assessment*. Cambridge University Press, 130 pp.

Szyrmer, W., and I. Zawadzki, 1997: Biogenic and anthropogenic sources of ice-forming nuclei: A review. *Bull. Amer. Meteor. Soc.*, **78 (2)**, 209–228.

Tanaka, T. Y., and M. Chiba, 2006: A numerical study of the contributions of dust source regions to the global dust budget. *Global and Planetary Change*, **52**, 88–104, doi:10.1016/j.gloplacha.2006.02.002.

Terai, C. R., R. Wood, D. C. Leon, and P. Zuidema, 2012: Does precipitation susceptibility vary with increasing cloud thickness in marine stratocumulus? *Atmos. Chem. Phys.*, **12 (10)**, 4567–4583, doi:10.5194/acp-12-4567-2012.

Thomas, C. D., A. Cameron, R. E. Green, M. Bakkenes, L. J. Beaumont, and Y. C. Collingham, 2004: Extinction risk from climate change. *Nature*, **427 (6970)**, 145–148.

Thomson, W., 1872: On the equilibrium of vapour at a curved surface of liquid. *Proc. Roy. Soc. Edinburgh*, **7**, 63–68.

Tietze, K., J. Riedi, A. Stohl, and T. J. Garrett, 2011: Space-based evaluation of interactions between aerosols and low-level Arctic clouds during the spring and summer of 2008. *Atmos. Chem. Phys*, **11** doi:10.5194/acp-11-3359-2011, 3359–3373.

Twohy, C. H., 2005: Evaluation of the aerosol indirect effect in marine stratocumulus clouds: Droplet number, size, liquid water path, and radiative impact. *J. Geophys. Res.*, **110 (D8)**, D08 203, doi:10.1029/2004JD005116.

Twomey, S., 1974: Pollution and the planetary albedo. *Atmos. Environ.*, **41 (SUPPL.)**, 120–125, doi:10.1016/j.atmosenv.2007.10.062.

Twomey, S., 1977: The influence of pollution on the shortwave albedo of clouds. *J. Atmos. Sci.*, **34 (7)**, 1149–1152.

Uchiyama, A., A. Yamazaki, M. Shiobara, and H. Kobayashi, 2013: Case study on microphysical properties of boundary layer mixed-phase cloud observed at Ny-Alesund, Svalbard: Observed cloud microphysics and calculated optical properties on 9 June 2011. *Polar Science*, **16 (June 2011)**, doi:10.1016/j.polar.2013.11.001.

Unger, N., S. Menon, D. T. Shindell, and D. M. Koch, 2009: Impacts of aerosol indirect effect on past and future changes in tropospheric composition. *Atmos. Chem. Phys.*, **9 (1)**, 4691–4725, doi:10.5194/acpd-9-4691-2009.

Van de Hulst, H. C., 1948: Scattering in a planetary atmosphere. *The Astrophysical Journal*, **107**, 220.

Van de Hulst, H. C., and W. M. Irvine, 1963: General report on radiation transfer in planets scattering in model planetary atmospheres. *Liege International Astrophysical*, **11**, 78–98.

Van Tricht, K., and Coauthors, 2016: Clouds enhance Greenland ice sheet meltwater runoff. *Nat. Commun.*, **7 (May)**, 10 266, doi:10.1038/ncomms10266.

Venables, W. N., and B. D. Ripley, 2013: *Modern applied statistics with S-PLUS*. Springer Science and Business Media.

Verlinde, J., and Coauthors, 2007: The Mixed-Phase Arctic Cloud Experiment. *Bull. Amer. Meteor. Soc.*, **88 (2)**, 205–221, doi:10.1175/BAMS-88-2-205.

Villiers, R. A. D., G. Ancellet, J. Pelon, B. Quennehen, A. Schwarzenboeck, J. F. Gayet, and K. S. Law, 2010: Airborne measurements of aerosol optical properties related to early spring transport of mid-latitude sources into the Arctic. *Atmos. Chem. Phys.*, **10**, 5011–5030, doi:10.5194/acp-10-5011-2010.

Walsh, J. E., and W. L. Chapman, 1998: Arctic cloud-Radiation-temperature associations in observational data and atmospheric reanalyses. *J. Climate*, **11 (11)**, 3030–3045.

Wang, F., J. Guo, Y. Wu, X. Zhang, M. Deng, X. Li, J. Zhang, and J. Zhao, 2014: Satellite observed aerosol-induced variability in warm cloud properties under different meteorological conditions over eastern China. *Atmos. Environ.*, **84**, 122–132, doi:10.1016/j.atmosenv.2013.11.018.

Wang, M., and J. E. Overland, 2009: A sea ice free summer Arctic within 30 years? *Geophys. Res. Lett.*, **36 (7)**, doi:10.1029/2009GL037820.

Wang, M., J. E. Overland, V. Kattsov, J. E. Walsh, &. Zhang, X., and T. Pavlova, 2007: Intrinsic versus forced variation in coupled climate model simulations over the arctic during the twentieth century. *J. Climate*, **20 (6)**, 1093–1107, doi:10.1175/JCLI4043.1.

Warneke, C., and Coauthors, 2009: Biomass burning in Siberia and Kazakhstan as an important source for haze over the Alaskan Arctic in April 2008. *Geophys. Res. Lett.*, **36 (April 2008)**, 2–7, doi:10.1029/2008GL036194.

Warneke, C., and Coauthors, 2010: An important contribution to springtime Arctic aerosol from biomass burning in Russia. *Geophys. Res. Lett.*, **37 (L01801)**, doi:10.029/2009GL041816.

Wehner, B., and A. Wiedensohler, 2002: Long term measurements of submicrometer urban aerosols: Statistical analysis for correlations with meteorological conditions and trace gases. *Atmos. Chem. Phys.*, **2 (5)**, 1699–1733, doi:10.5194/acpd-2-1699-2002.

Wesslén, C., M. Tjernström, D. H. Bromwich, G. De Boer, a. M. L. Ekman, L. S. Bai, and S. H. Wang, 2014: The Arctic summer atmosphere: An evaluation of reanalyses using ASCOS data. *Atmos. Chem. Phys.*, **14**, 2605–2624, doi:10.5194/acp-14-2605-2014.

Westerling, a. L., H. G. Hidalgo, D. R. Cayan, and T. W. Swetnam, 2006: Warming and earlier spring increase western U.S. forest wildfire activity. *Science*, **313 (5789)**, 940–943, doi:10.1126/science.1128834.

Winther, M., J. H. Christensen, M. S. Plejdrup, E. S. Ravn, Ó. F. Eriksson, and H. O. Kristensen, 2014: Emission inventories for ships in the arctic based on satellite sampled AIS data. *Atmos. Environ.*, **91**, 1–14, doi:10.1016/j.atmosenv.2014.03.006.

Wood, R., 2006: Relationships between optical depth, liquid water path, droplet concentration and effective radius in an adiabatic layer cloud. **3 (7)**, 7–9.

Xie, Y., 1999: Identification of source nature and seasonal variations of Arctic aerosol by the multilinear engine. *Atmos. Environ.*, **33 (16)**, 2549–2562, doi:10.1016/S1352-2310(98)00196-4.

Yang, Q., and Coauthors, 2015: Aerosol transport and wet scavenging in deep convective clouds: A case study and model evaluation using a multiple passive tracer analysis approach. *J. Geophys. Res.: Atmos.*, **120 (16)**, 8448–8468, doi:10.1002/2015JD023647.

Yoshimori, M., M. Watanabe, A. Abe-Ouchi, H. Shiogama, and T. Ogura, 2013: Relative contribution of feedback processes to Arctic amplification of temperature change in MIROC GCM. *Climate Dyn.*, **42 (5-6)**, 1613–1630, doi:10.1007/s00382-013-1875-9.

Yu, L., and R. A. Weller, 2007: Objectively analyzed air-sea heat fluxes for the global ice-free oceans (1981-2005). *Bull. Amer. Meteor. Soc.*, **88 (4)**, 527.

Zamora, L. M., and Coauthors, 2015: Aircraft-measured indirect cloud effects from biomass burning smoke in the Arctic and subarctic. *Atmos. Chem. Phys. Discuss.*, **15 (16)**, 22 823–22 887, doi:10.5194/acpd-15-22823-2015.

Zdanowicz, C. M., G. a. Zielinski, and C. P. Wake, 1998: Characteristics of modern atmospheric dust deposition in snow on the Penny Ice Cap, Baffin Island, Arctic Canada. *Tellus, Ser. B*, **50**, 506–520.

Zhang, S., and Coauthors, 2016: On the characteristics of aerosol indirect effect based on dynamic regimes in global climate models. *Atmos. Chem. Phys.*, **16 (5)**, 2765–2783, doi:10.5194/acp-16-2765-2016.

Zhao, C., and T. J. Garrett, 2015: Effects of arctic haze on surface cloud radiative forcing. *Geophys. Res. Lett.*, **42**, 557–564, doi:10.1002/2014GL062015.

Zhao, C., S. A. Klein, S. Xie, X. Liu, J. S. Boyle, and Y. Zhang, 2012: Aerosol first indirect effects on non-precipitating low-level liquid cloud properties as simulated by CAM5 at ARM sites. *Geophys. Res. Lett.*, **39**, 1–7, doi:10.1029/2012GL051213.

Zygmuntowska, M., T. Mauritsen, J. Quaas, and L. Kaleschke, 2012: Arctic clouds and surface radiation-a critical comparison of satellite retrievals and the ERA-interim reanalysis. *Atmos. Chem. Phys.*, **12 (14)**, 6667–6677, doi:10.5194/acp-12-6667-2012.